University of Alaska
Coastal Marine Institute

Physical–Biological Numerical Modeling
on Alaskan Arctic Shelves

Henry J. Niebauer, Principal Investigator
University of Alaska Fairbanks

Final Report

August 2000

Final Report

Physical–Biological Numerical Modeling on Alaskan Arctic Shelves

by

Henry J. Niebauer, Principal Investigator

Institute of Marine Science
University of Alaska Fairbanks
Fairbanks, AK 99775-7220

E-mail: niebauer@sunset.meteor.wisc.edu

August 2000

ERRATA to Physical-Biological Numerical Modeling on Alaskan
Arctic Shelves, OCS Study MMS 2000-041

After this report was published, an error was discovered in the model code in the calculation of the Richardson number. The Richardson number is used in calculating vertical eddy viscosity and diffusivity in equations 10-12. The error was that Sigma-t, rather than density, was used in calculating a vertical density gradient to calculate the Richardson number. This made the vertical density gradient 1000 times greater than it should have been. This made the Richardson number higher, making the eddy viscosity and diffusivity lower which made diffusion of scalars and momentum lower. Away from vertical density gradients this had no effect. A sensitivity analysis was performed that showed the effect of this error was not large (partially because it is non-linear; equations 10-11). The sensitivity test was to run a model version (specifically experiment #74) for a month with and without the error. The difference in primary productivity, or the rate of carbon fixing was 1.9% (less primary productivity with the error because there was less diffusion). Primary production or chlorophyll was 3% lower for the same reason.

The results suggest that the difference caused by the error is ~2-4%. This does not change any of the results or conclusions. However, all the experiments will be rerun, with the correction, for journal publication. The differences are expected to be minor. The author regrets any inconvenience to readers and further questions can be directed to him at the email address given on report title page.

Table of Contents

List of Tables

List of Figures

Abstract

In this study, numerical models have been used to model the generation, flux and fate of the natural primary production phytoplankton particles, and their interaction with each other and with physical processes. The physical air–ice–ocean interaction has been modeled numerically in a relatively fine scale cross-sectional model. Experiments include melting ice in a marginal ice edge zone, coastal upwelling along an ice covered coast, and wind-driven cyclonic motion as would be generated by a passing storm. This cyclonic motion causes opening of ice and preconditioning of water via upwelling. This is followed by a cooling event. The cooling generates ice in the open water, causing brine rejection, leading to vertical convection of sea water. These physical interactions have been simultaneously modeled with both biological primary production and the subsequent aggregation of phytoplankton. Results suggest that two main sources or pathways or processes for the formation and flux of particles are brine rejection from ice formation in fall and winter, and aggregation in primary production blooms in spring and summer. Available hydrographic and biological data have been used for initial and boundary conditions and for verification. Verification from limited data available is reasonably good.

Introduction

The circulation on the Chukchi Sea shelf north of the Bering Strait (Fig. 1) is not well understood although progress is being made [e.g., Weingartner et al. 1998]. This broad, shallow shelf bordering the deep Arctic Ocean basin is an area of confluence of ocean flow from the Bering Sea to the south and from the Siberian shelf to the west. This confluent flow tends to spread out toward the deep Arctic Ocean beyond the shelf break, where it meets westward flow from the Beaufort Sea moving past Point Barrow. Some of this confluent flow is turned westward along the Siberian shelf break, while some recirculates on the shallow Siberian shelf back toward the Chukchi shelf. There is also subsurface flow which moves off of the shelf and/or down the shelf break canyons, such as the Barrow Canyon, feeding the Arctic Ocean halocline, or deeper. Some of this subsurface flow moves around Point Barrow and continues east along the Beaufort shelf break.

The circulation and dynamics of the Alaska Beaufort and Chukchi Sea shelves are further complicated by the cover of mobile and restless sea ice in winter that reduces to a partial covering of ice in summer. In other ice infested seas such as the Bering Sea and East Greenland Sea, increased insolation in spring and summer, and the resulting melt water, causes surface low-salinity stratification leading to increased primary production. There is reason to suspect that this also happens in the Chukchi/Beaufort Seas. In spring, ice melt water causes surface ocean density stratification which leads to elevated biological primary production in the presence of sunlight and nutrients [e.g., Alexander and Niebauer 1981; Niebauer et al. 1990, 1995].

In fall and winter, ice formation in the leads, cracks, shear zones and polynyas, as well as episodic wind events which open gaping holes in the ice canopy, lead to brine formation [e.g., Cavalieri and Martin 1994]. This brine convectively sinks to the shelf bottom and feeds into the Arctic Ocean halocline through, for example, the Barrow Canyon [e.g., Weingartner et al. 1998].

While biological production in the permanently ice covered Arctic Ocean is low, in the seasonally ice free shelf regions surrounding the Arctic Ocean, it can be high, and interaction of the ocean and biology with

ice is important [e.g., Alexander and Niebauer 1981; Grebmeier and Cooper 1995; Niebauer et al. 1990, 1995; Walsh et al. 1989; Smith and Sakshaug 1990]. Arctic marine food webs are greatly influenced by the interdependency of sea ice, water density and nutrient availability. The currents and ice may carry materials derived from human activity, as well as natural materials, into the region and interact with biological processes. Materials derived from human activity can include petroleum, material from offshore mining, radionuclides etc. Natural materials include nutrients, detritus, and again, petroleum particles. For example, the flow from the Bering Sea into the Chukchi Sea is particularly rich in nutrients which fuel high primary production in the southern Chukchi Sea [Walsh et al. 1989]. The Bering Sea may be a primary source of nutrients to Fram Strait in the eastern Arctic [W.O. Smith, Jr., pers. comm.], and these nutrients must cross the Chukchi/Beaufort shelves to get there.

Primary production particles (i.e., phytoplankton) aggregate, incorporate and otherwise interact with each other forming larger, more dense particles which sink faster. Single cell sinking is ~ 0.5–1 m d^{-1} while aggregate sinking speeds range to ~ 10 m d^{-1}, although speeds of up to 100 m d^{-1} [e.g., Hill 1992], and even >200 m d^{-1} [e.g., Gardner 1997] have been reported in the ocean. Aggregation and sinking carry these particles out of the photic zone and surface layers and deeper into the ocean. Because cold water tends to slow zooplankton development, phytoplankton are not heavily grazed [e.g., Coyle and Cooney 1988] and so can sink to the bottom. This primary production directly feeds the substantial benthic communities, and both directly and indirectly feeds the sizable marine mammal populations of the Arctic shelves. It is the bio–physical–chemical interactions of the primary production and their fluxes and fates that are being modeled with the aim of predictive capability.

In addition to the aggregation and sinking of spring blooms, the dense water (brine) generated when ice forms can also carry particulate material to the benthos, into the Arctic Ocean halocline or to the abyss beyond. As mentioned above, the Arctic Ocean halocline, which begins at only 30–60 m and is ~ 100 m thick, is thought to result from the lateral input of cold, high salinity water from the polynyas and leads, etc. Brine generation undoubtedly entrains particulate material of "new" production from the seasonal ice edge and open water blooms on the Arctic shelves, including the Bering Sea [Walsh et al. 1989].

This project used numerical models of air–ice–ocean interaction with biological production and nutrient chemistry to understand, model and quantify energy and material (i.e., biological or primary production, chemical nutrients, salt brine) interaction, pathways, fluxes and fates on the Alaskan Arctic shelves.

Objectives and hypotheses

Emphasis was placed on understanding and predicting the interaction of primary production particles and their flux (especially vertical, but also horizontal) and their fate on Arctic shelves.

The specific objectives were:

1) To modify an existing numerical model of Arctic waters [Niebauer and Smith 1989; Smith and Niebauer 1993], which includes sea ice as well as biological and nutrient chemistry interactions, to realistically model the vertical flux of phytoplankton as aggregates;

2) To model Arctic shelf spring phytoplankton blooms, aggregation and vertical transport of chlorophyll/phytoplankton as a function of physical processes of melt water and/or solar heated

surface stratification, wind mixing and wind-driving (coastal upwelling) of nutrients into the photic zone.

3) To model the vertically downward transport of water, both in conjunction with and as a separate process from the flux of natural/primary production particles and particle aggregation. This physical emphasis includes modeling higher density surface water formation and deep convection through processes such as ocean surface cooling, ice formation and brine rejection, and possible interaction with eddies.

4) To interact with field/data groups and individuals, as recommended by the National Academy of Science reports, who are working on different aspects of the Alaska Arctic shelves such as Dr. Tom Weingartner (e.g., hydrography, current meters, meteorology). The objective was to use field data to model initial and boundary conditions and to verify model results, and to use the model results to help form hypotheses, test ideas and refine field studies and plans. We also proposed to explore whether our modeling might or should eventually be reworked as an imbedded model in the larger scale regional circulation and/or trajectory model of the Chukchi/Beaufort Seas such as proposed by Dr. Weingartner and Dr. Andrey Proshutinsky at the University of Alaska, or by Dr. Dale Hadvogel of Rutgers University.

Hypotheses:

1) Phytoplankton particle and particle–particle interactions (aggregation) and subsequent sinking provide a dominant pathway for the removal of natural particles, nutrients and carbon from the surface layer. This material goes to the shelf bottom, the Arctic halocline or the deep Arctic basin.

   a) During spring blooms, melt water stratification leads to primary production which aggregates and sinks, carrying material to the bottom.

   b) During winter ice formation, polynyas (events) and larger ice-spreading events when open water is exposed to freezing temperatures, ice forms causing brine rejection and downward convection of cold, salty, dense water carrying material to the benthos and into the Arctic Ocean halocline.

2) Variability in environmental conditions strongly affects the timing, flux and fate of dense water and primary production of particles. In some years, sea ice barely pulls away from the Alaska Arctic coast while in other years the open ocean extends 10s of kilometers. This must also strongly affect the formation, flux and fate of water and biological particles.

Methods

Below is a narrative text of the modeling, followed by technical details.

The model is a cross-sectional, multi-layered, time-dependent, finite difference numerical model that is composed of physical, biological and sea ice sub-models (Fig. 2). The original physical model had its genesis in Bennett [1974] but has been greatly modified. For this project, the space dimensions are ~120 km in the horizontal by ~300 m in the vertical with Δx of 3 km and Δz of 5 m. Recent simulation

durations have been 12 weeks with Δt of 10 min [Smith et al. 1999]. These dimensions and details are fairly arbitrary and really only depend upon computer power.

The physical and biochemical ocean and ice sub-models are a series of time- and space-dependent coupled non-linear equations of motion which include the effects of Coriolis, wind and heat forcing, ice motion, as well as melting and freezing, and vertical and horizontal density gradients and ocean currents. Ocean density is a function of salinity, temperature and pressure. The physical model is a cross-sectional circulation model, sometimes called a 2½ dimensional model in space in that currents etc. can vary in time and space in the vertical and in the horizontal dimension parallel to the section. However, perpendicular to the section, currents can exist but can vary only in time but not in space along this dimension. That is to say, the dimension perpendicular to the cross section is modeled as very long and so, for example, edge waves cannot propagate in this direction. The model is 3½ dimensional including time. The initial conditions for salinity, temperature and density are shown in Figure 3 as taken from Aagaard et. al. [1988].

The biological sub-model [Niebauer and Smith 1989] includes two separate nutrient pools (nitrate and ammonium), phytoplankton nutrient uptake, grazing by zooplankton, and nutrient recycling and regeneration. The initial conditions for nitrate are 8 µM for 0–40 m, 12 µM for 40–60 m, 16 µM for 60–75 m, and back to 12 µM for 75–300 m [Aagaard et. al. 1988]. Ammonia is set at 0.5 µM throughout. Primary production is driven by an insolation sub-model as a function of date and latitude as well as nutrients and physical parameters such as depth, temperature, stratification, etc.

Code on biological particle aggregation [modified after Riebesell and Wolf-Gladrow 1992] has also been added as aggregation appears to be an important process for transporting biological products deeper in the ocean (i.e., bigger aggregations are more dense and so sink faster).

The phytoplankton initial conditions are that all size classes are set = 0.01 µg L^{-1} except for the first (smallest) size class which = 0.1 µg L^{-1}. This results in a total chlorophyll concentration at each grid point = 0.19 µg L^{-1}. Zooplankton initial conditions are that large zooplankton are = 0.15 µg N L^{-1} (20.4 mg dry wt m^{-3}) above 30 m and are = 0.03 µg N L^{-1} (4.1 mg dry wt m^{-3}) below 30 m. Small zooplankton = 0.01 µg N L^{-1} (1.4 mg dry wt m^{-3}) throughout. These are taken from Niebauer and Smith [1989] and are somewhat arbitrary but are required to get the predation going.

The physical sea ice sub-model is a simple balance among Coriolis force, wind drag and ocean drag. The coupling between wind and water is enhanced by the moving intermediary ice. That is, the drag between wind and ice and between ice and water is greater than between wind and water. Thermodynamics connect ice and water so that there can be change a of state between water and ice. The ice sub-model allows for sea ice formation and thickening (and salt rejection), melting and thinning (and associated ocean freshening), and differential advection (and associated mechanical thinning and thickening of sea ice due to both wind stress from above and current stress from below). Therefore, both latent heat and sensible heat polynyas can form. In the present model, it is probably a stretch to say that leads (~meters) can form because the horizontal grid spacing is 3 km, a dimension closer to polynyas. However, the model does allow 0–100% ice cover in each grid space so that leads can be simulated to some extent.

This next section deals with the details of the model.

Physical processes

The equations of advection and diffusion of momentum, heat and salt, as well as continuity, the hydrostatic approximation and the equation of state are as follows:

$$\frac{\partial u}{\partial t}+u\frac{\partial u}{\partial x}+w\frac{\partial u}{\partial z} = \frac{-1}{\rho}\frac{\partial p}{\partial x}+\frac{1}{\rho}\frac{\partial \tau_{zx}}{\partial z}+N_x\frac{\partial^2 u}{\partial x^2}-fv \tag{1}$$

$$\frac{\partial v}{\partial t}+u\frac{\partial v}{\partial x}+w\frac{\partial v}{\partial z} = \frac{-1}{\rho}\frac{\partial p}{\partial y}+\frac{1}{\rho}\frac{\partial \tau_{zy}}{\partial z}+N_x\frac{\partial^2 v}{\partial x^2}-fu \tag{2}$$

$$\frac{\partial T}{\partial t}+u\frac{\partial T}{\partial x}+w\frac{\partial T}{\partial z} = K_{zT}\frac{\partial^2 T}{\partial z^2}+K_{xT}\frac{\partial^2 T}{\partial x^2} \tag{3}$$

$$\frac{\partial S}{\partial t}+u\frac{\partial S}{\partial x}+w\frac{\partial S}{\partial z} = K_{zS}\frac{\partial^2 S}{\partial z^2}+K_{xS}\frac{\partial^2 S}{\partial x^2} \tag{4}$$

$$\frac{\partial u}{\partial x}+\frac{\partial w}{\partial z} = 0 \tag{5}$$

$$\frac{\partial p}{\partial z} = \rho g \tag{6}$$

$$\rho = \rho(S,T,p) \tag{7}$$

Table 1. Variables in Equations 1–9.

Variable	Definition
x	coordinate normal to ice edge
y	coordinate parallel to ice edge
z	vertical coordinate
t	time
$u(x,z,t)$	x component of velocity (normal to ice edge)
$v(x,z,t)$	y component of velocity (parallel to ice edge)
$w(x,z,t)$	z component of velocity (vertical)
f	Coriolis parameter
g	gravitational acceleration
ρ	density of water
p	pressure
$\tau_x(x,z,t)$	x component of vertical shear stress
$\tau_y(x,z,t)$	y component of vertical shear stress
Δx	horizontal grid spacing (3 km)
Δz	vertical grid spacing (5 m)
Δt	time step (600 sec)
$T(x,z,t)$, °C	temperature
$S(x,z,t)$, psu	salinity
$N_z(x,z,t)$, cm^2 s^{-2}	vertical eddy viscosity as a function of the Richardson Number
$K_z(x,z,t)$, cm^2 s^{-2}	vertical eddy diffusivity of heat and salt as a function of the Richardson Number
N_x	horizontal eddy viscosity (1.5×10^6 cm^2 s^{-2})
K_x	horizontal eddy diffusivity of heat and salt (1.5×10^5 cm^2 s^{-2})

The variables in (1)–(9) are defined in Table 1. These equations, as well as the ice model and biochemical equations, are all solved by a finite difference scheme. A non-linear equation of state with density as a function of temperature, salinity and pressure [Millero et al. 1980; Millero and Poisson 1981] is included because at the low temperatures of polar waters, salinity differences dictate density gradients, while temperature is required for realistic simulation of the thermodynamics of the MIZ (marginal ice zone) as well as an input for biological dynamics. Density as a function of pressure is also required to test hypotheses concerning penetrative convection.

Solutions to the physical and biological equations are generated on a 120 km by 300 m gridded section through the marginal ice edge zone (Fig. 2). The Boussinesq approximation is invoked; in addition, it is assumed that all along-ice time dependent gradients may be neglected, which implies that the along-ice direction is modeled as infinitely long. As a result, both vectors and scalars (e.g., currents, temperature) can vary in time but not in space along this axis, which results in some features (e.g., edge waves) being filtered out. The ocean surface is modeled as a rigid lid which eliminates surface waves and tides while

markedly increasing the length of the time step consistent with computational stability [e.g., Bennett 1974]. The time scale of the model (10 min) easily resolves both the biological and physical processes associated with Coriolis dynamics (f^{-1} or ~2 hours). Tilting of the sea surface and associated barotropic transport are allowed in the along-ice direction as dictated by boundary conditions such as wind stress.

In the numerical solution all but the diffusion terms are calculated by a "leapfrog"-centered time difference method. The diffusion terms are forward differenced in time, while the spatial derivatives are evaluated by centered differences. This procedure conserves mass, momentum and energy when used with the flux form of the equations as is done here. The pressure gradient terms in (1) and (2) are computed diagnostically from the hydrostatic equations and mass balance constraints.

The boundary conditions include the no-slip condition at the bottom, while at the surface and bottom the vertical velocity is zero. Except for the coastal upwelling simulation, there are no vertical solid boundaries (i.e., coasts) so that heat and salt fluxes are either specified or are zero only at the surface and at the bottom. Radiation conditions are specified at the two open-ocean boundaries so that information (e.g., momentum, heat, salt) passes through with as little reflection or distortion as possible. This is done by relaxing the tangency and no-slip conditions on these boundaries and then taking the first three columns (i.e., 6 km) interior of the boundary, including the boundary column, and setting all of the vectors and scalars in those columns equal to the fourth column (i.e., 9 km from the boundary) on each time step. This allows momentum, mass and heat to pass through the boundary without reflection. We have made many runs with this model with these boundary conditions as well as with solid boundaries and have little trouble with computational instabilities. No reflections or distortions of the interior solutions have been observed with this formulation. Wind stress is specified at the surface of the ocean and/or the ice, while below the surface vertical shear stresses are computed using:

$$\tau_{zx} = \rho N_z \frac{\partial u}{\partial z} \tag{8}$$

$$\tau_{zy} = \rho N_z \frac{\partial v}{\partial z} \tag{9}$$

The vertical mixing of momentum, heat and salt are given by Munk and Anderson [1948]:

$$N_z = 5 + 50\left(1 + 10 R_i\right)^{-0.5} \tag{10}$$

$$K_z = 50\left(1 + 3.33 R_i\right)^{-1.5} \tag{11}$$

The Richardson number (R_i) is defined by:

$$R_i(x, z, t) = \frac{g}{\rho}\left(\frac{\partial \rho}{\partial z}\right) \Bigg/ \left[\left(\frac{\partial u}{\partial z}\right)^2 + \left(\frac{\partial v}{\partial z}\right)^2\right] \tag{12}$$

At one vertical grid space above the bottom shear stresses are computed from:

$$\tau_{zx} = \rho\, 0.002 \left(u^2 + v^2\right)^{0.5} u \tag{13}$$

$$\tau_{zy} = \rho\, 0.002 \left(u^2 + v^2\right)^{0.5} v \tag{14}$$

The dimensionless value of the drag coefficient, 0.002, is a commonly quoted value for typical bottom roughness [e.g., Bennett, 1974].

The values of the horizontal eddy viscosity and diffusivity were chosen as low as possible to illustrate the advective nature of the circulation and to smooth the solutions. The horizontal eddy viscosity is in the range of those used to model coastal upwelling [e.g., Hamilton and Rattray 1978] and allows the formation of a baroclinic geostrophic ice edge jet in the coastal upwelling experiments. Further details of the general characteristics of this model are given in Bennett [1974], Niebauer [1982] and Niebauer and Smith [1989].

The ice sub-model is conceptually simple. Ice thickness is specified at each surface grid point as an initial condition. The mass of ice is conserved while being acted upon by wind and ocean stresses (horizontal advective fluxes) as well as by ocean temperatures (vertical heat and salt fluxes). The ice cover is assumed to be in free drift on the ocean so that momentum is modeled as a simple balance between stresses exerted by the wind, water and Coriolis force [McPhee 1980; Pease and Overland 1984]. Internal ice stress and the nonlinear terms in the ice momentum equations are assumed to be negligible, which is reasonable only away from the deep winter ice pack and from coastal barriers, where internal ice stress and floe interaction are important to the total momentum balance. The ice momentum equations are:

$$\tau_{aix} - \tau_{iwx} + \rho_i d_i f V_i = 0 \tag{15}$$

$$\tau_{aiy} - \tau_{iwy} + \rho_i d_i f U_i = 0 \tag{16}$$

where τ_{aix} and τ_{aiy} are the stresses between the air and ice, τ_{iwx} and τ_{iwy} are the stresses between ice and water, ρ_i is the density of ice (0.91 gm cm^{-3}), d_i is the thickness of the ice, and U_i and V_i are the ice velocities in the x and y directions. Wind stresses between air and water, τ_{awx} and τ_{awy}, are calculated via:

$$\tau_{awx}(x,t) = \rho_a C_a U_w^2 \tag{17}$$

$$\tau_{awy}(y,t) = \rho_a C_a V_w^2 \tag{18}$$

where ρ_a is the density of air (0.0012 gm cm^{-3}), C_a is the drag coefficient between air and water ($\sim 10^{-3}$) and U_w and V_w are the wind velocities. (With this formulation an 8 m s^{-1} or $\sim$16 kt wind will produce an $\sim$1 dyne cm^{-2} stress.) Studies of the atmospheric boundary layer over ice suggest that the drag coefficient is approximately twice that over water [Feldman et al. 1979; Overland 1985], so that τ_{aix} and τ_{aiy} are modeled using (17) and (18) with C_{ai}, the drag coefficient between air and ice, equal to $2 C_a$. The interfacial drag between ice and water is modeled as:

$$\tau_{iwx}(x,t) = \rho C_{wi}\left(u - U_i\right) \tag{19}$$

$$\tau_{iwy}(x,t) = \rho C_{wi}\left(v - V_i\right) \tag{20}$$

where C_{wi} is the drag coefficient between ice and water (0.086) and $(u - U_i)$ and $(v - V_i)$ are the differences between ocean and ice velocities [Hibler 1979; McPhee 1980].

Equations (15) and (16) are solved analytically at each time step of the ocean model for U_i and V_i on the same time and space scales as the ocean model. Ice fluxes are then calculated, but only in the cross-ice direction, as ice motion is assumed independent of the along-ice direction just as vectors and scalars are in the ocean model. Once the ice flux is known, ice concentrations and thicknesses are recalculated. Ice flux is constrained to allow slightly >100% ice concentration at any point in the grid (i.e., some rafting of the ice can occur). Once the new ice concentrations are known, the stresses that actually enter the surface of the ocean are calculated via:

$$\tau_{zx}(x,t) = \tau_{awx}(x,t)(1 - A) + \tau_{iwx}(x,t)A \tag{21}$$

$$\tau_{zy}(x,t) = \tau_{awy}(x,t)(1 - A) + \tau_{iwy}(x,t)A \tag{22}$$

where A is ice concentration (calculated as the ratio of ice thickness to the initial ice thickness). The ice concentration calculations are important because the contributions of τ_{iwx} and τ_{iwy} are proportional to the ice concentration, whereas τ_{awx} and τ_{awy} are proportional to $(1 - A)$, but never less than zero. Finally, given the momentum transfer into the ocean directly from the wind as well as from the wind to the ice to the ocean, the surface ocean velocities are calculated in (1)–(5) and serve as input to (15) and (16) to begin the next iteration. In (15) and (16), no turning angle is assumed or parameterized; the Coriolis terms in (15) and (16) account for the turning of the ice while the ocean model accounts for the turning of the currents below the ice–water and wind–water stresses.

The thermohaline dynamics of the ice are modeled by (23)–(25), which describe heat and fresh water flux to and from the ice as well as the variations in ice thickness due to melting or freezing. These equations are:

$$Q_i(x,t) = AK_i\left(T_o - T_i\right)d^{-1} \tag{23}$$

where Q_i is the vertical conduction heat flux into or out of the ice, K_i is 4.86 x 10^{-3} cal m^{-1} (of ice) s^{-1} °C^{-1} [Semtner 1976], T_o is the surface ocean temperature, T_i is the ice temperature which is assumed to be at the freezing point (~ -1.75°C) of sea water with a salinity of ~32‰, and d is the assumed thickness over which actual melting is taking place (arbitrarily set to 10 cm). When the ice thickness becomes less than 10 cm, d is set equal to the actual thickness of the ice but not less than 1 cm.

Fresh water flux between ice and ocean (F_s) is given by:

$$F_s(x,t) = \rho_i\left(S_o - S_i\right)\frac{Q_i}{Q_f} \tag{24}$$

where S_o is the ocean salinity, S_i is the salinity of the ice (assumed to be 5%) and Q_f is the volumetric heat of fusion for ice, which is assumed to be 64 cal cm^{-3} for ice with a salinity of ~5‰ and temperature ~−1.75°C [Doronin and Kheisin 1977]. Fluxes of latent heat, sensible heat, insolation and incoming longwave radiation are all set to zero.

Variations in ice thickness, $D(x,t)$, are calculated via:

$$D(x,t) = \frac{Q_i}{Q_f} \qquad (25)$$

As in the ice momentum equations, the thermodynamic equations are all solved on the same time and space scales as the ocean model.

The biological parameters within the model include nutrients (nitrate and ammonium), phytoplankton (10 size classes), and both micro- and macrozooplankton. These classes of plants and animals are used as they have been shown [e.g., Hewes et al. 1985; Smith and Nelson 1985; Smith et al. 1987] to be important in marginal ice zones and polar oceans. The equations for each of these parameters are similar to (3) and (4) except that biochemical terms that modify the concentration and distribution of the variables have been added. Thus all of these biochemical parameters are modified by their initial and boundary conditions and interactions among each other, as well as being affected by the physical processes (continuity, advection, diffusion, ice melt, etc.) in the model.

Although the zooplankton are divided into two size classes, the smaller size class contributed only minor amounts to biomass and productivity as a result of the initial conditions used in this study. Additional experiments have verified the quantitative significance of the nanoplankton and microzooplankton under other (e.g., low nutrient) conditions.

Irradiance often is a major factor controlling phytoplankton growth in polar regions because the extreme seasonal variations give rise to low incident irradiances, and because deep vertical mixing can create low mean irradiances within the water column [Smith 1987]. In our model the amount of irradiance reaching the ocean's surface depends on the Julian date and latitude, which in turn control the solar declination and angle. The amount of radiation reaching the ocean's surface is a function of the solar constant, an atmospheric turbidity factor, an atmospheric attenuation coefficient, the relative atmospheric thickness and a diffuse radiation component. We include these factors to calculate insolation as a function of time in a manner similar to that of Jamart et al. [1977]. However, these equations do not include the effects of atmospheric moisture, dust and pollutants. As a result, they overestimate the actual radiation which reaches the earth's surface. To remedy this, we applied a 0.7 correction factor to the solar constant of 1.92 cal cm^{-2} min^{-1}.

At the ocean's surface, irradiance is both reflected and refracted. The amount reflected (assuming a calm surface) is calculated using Snell's Law and the refraction is calculated by Beer's Law [Jerlov 1968]. The roughness of the sea state also greatly influences the amount of irradiance which can penetrate, but this factor is not included in these analyses. Irradiance is attenuated exponentially within the water column by:

$$I_z = I_0 e^{-kz} \tag{26}$$

where I_z and I_0 are the amount of irradiance at depth z and the surface, respectively, and k is the attenuation coefficient (in reciprocal meters). Phytoplankton are the major agent of irradiance absorption in most oceanic regions. We approximated k from chlorophyll concentrations using the relationship of Riley [1956]:

$$k = 0.44 + 0.0088(chl) + 0.054(chl)^{2/3} \tag{27}$$

This allowed us to calculate depth-dependent variations (e.g., self-shading) in irradiance attenuation and hence simulate realistic variations in phytoplankton growth and photosynthesis.

Ice and overlying snow cover greatly attenuate irradiance [Maykut and Grenfell 1975]. In the model we used an attenuation coefficient of 4.61 m^{-1}, which is intermediate between pure ice and ice with a deep snow cover. Irradiance penetration is a function not only of thickness but of the percentage of open water in the ice. This is a dominant factor in controlling irradiance penetration into the water and is accounted for here.

Maximum phytoplankton growth is in general set by temperature. This temperature dependence can be expressed as [Eppley 1972]:

$$\mu_{\max} = 10^{(0.0275T - 0.23)} \tag{28}$$

However, light and nutrients are needed in sufficient quantity before growth can proceed at maximal rates. In this model the effects of both irradiance and nutrients are independently computed and the growth rate is scaled according to the degree of limitation. Biomass is expressed in units of nitrogen and converted to or from carbon and chlorophyll using C/N and nitrogen/chlorophyll (mole/weight) ratios of 6.6 and 0.8 respectively. The relationship between irradiance and photosynthesis is parameterized as follows [Platt et al. 1980]:

$$F = \left[1 - \exp\left(-\alpha I_z / P_s^B\right)\right] \exp\left(-\beta I_z / P_s^B\right) \tag{29}$$

where F is the factor which modifies the temperature dependence of growth (and is equal to the ratio between realized and maximum photosynthesis), α is the slope of the light-dependent portion of the light response of chlorophyll-specific photosynthesis, P_s^B is the maximum rate of photosynthesis (per unit of chlorophyll), and β is the parameter which describes the propensity of the population to photoinhibition (i.e., when $\beta = 0$, no photoinhibition occurs). Initial values for the model were taken from Harrison and Platt's [1985] results in the Canadian Arctic (i.e., $P_s^B = 1.32$ mg C (mg chl)$^{-1}$ h^{-1}, $\alpha = 0.057$ and $\beta = 0.001316$ mg C (mg chl)$^{-1}$ h^{-1} (W m^{-2})$^{-1}$ where W = watts. For the model runs in this project, $P_s^B = 7.92$. Phytoplankton respiration is included in the model by assuming that respiration accounts for a constant loss equal to 2.5% of the maximum photosynthetic rate.

The effects of nutrients on phytoplankton growth can be described by the Monod relationship [Dugdale and Goering 1967]:

$$V = V_{\max}\left[s/(K_s + s)\right] \tag{30}$$

where V is the rate of nutrient uptake, V_{max} is the maximal rate of nutrient uptake, s is the ambient nutrient concentration, and K_s is the half-saturation constant (i.e., the concentration of nutrient at which $V = V_{max}/2$). The effects of the nutrient limitation are included by modifying the growth rate by the ratio of V/V_{max}.

Two nutrients, nitrate and ammonium, are included in the model. Nitrate is the primary nitrogen source for autotrophic growth in marginal ice zones, particularly in the spring bloom [Müller-Karger and Alexander 1987; Smith and Kattner 1988]. In the model nitrate is produced from ammonium by bacteria in the process of nitrification (BNIT), which is temperature dependent [Kremer and Nixon 1978] and is modeled by:

$$BNIT = \left[NH_4^+\right]\left[1 - \exp\left(0.068\left(1.188^{T-20}\right)\right)\right] \tag{31}$$

Ammonium is also a source of nitrogen for phytoplankton growth. Both nitrate and ammonium are removed by phytoplankton according to (30); however, when ammonium concentrations exceed threshold, nitrate uptake is reduced. Such an interaction is empirically modeled by:

$$INH = -0.5\left[NH_4^+\right] + 1.5 \tag{32}$$

Where INH is the nitrate uptake inhibition factor. Although the interaction is modeled as a linear function, there is evidence in the literature that the interaction is nonlinear [Conway 1977]. INH is constrained within 0.0 and 1.0, which implies that there is no inhibition of nitrate uptake at ammonium concentrations below 1.0 μM and complete inhibition at ammonium levels above 3.0 μM. The nitrate uptake rate is multiplied by the factor INH to give the actual nitrate removal rate.

In a previous use of this model [Niebauer and Smith 1989], the phytoplankton populations were divided into "large" and "small" phytoplankton. In the present use of the model, the focus is vertical flux of phytoplankton particles and so it includes 10 size classes within which there is aggregation and thus variable sinking as outlined below.

In the photic layer, primary production results in phytoplankton cells or particles which are initially small and slow sinking (~cm d^{-1}). These cells undergo aggregation which results in larger particles made up of aggregates of cells which sink faster (m d^{-1} to 10s m d^{-1}) because they are more dense. To model this aggregation, we started with the equations of Jackson [1990] and Riebesell and Wolf-Gladrow [1992] for modeling algal flocs through physical coagulation processes:

$$\frac{dC_i}{dt} = \frac{1}{2}\mu_{\frac{i}{2}}\left[1 - b_{\frac{i}{2}}\right]C_{\frac{i}{2}} - \mu_i C_i + 2\mu_i b_i C_i + \alpha\sum_{j=1}^{\frac{i}{2}}\beta_{j,i-j}C_j C_{i-j} - \alpha C_i\sum_{j=1}^{i_{\max}}\left(1 + \delta_{i,j}\right)\beta_{i,j}C_j - \frac{w_i}{H}C_i \tag{33}$$

$$(1) \qquad (2) \qquad (3) \qquad (4) \qquad (5) \qquad (6)$$

where i and j are the number of cells per aggregate, C_i and C_j are concentrations of aggregates of size i and j, μ is phytoplankton growth rate, b is the probability of cell breakup immediately after doubling, α is the probability of aggregates sticking upon contact (stickiness), δ is the Kronecker delta, β is the collision kernel, w_i is the size specific sinking rate, and H is the depth of the upper mixed layer.

The first three terms to the right of the equal sign (labeled 1–3 in equation 33) are the growth terms dependent upon the phytoplankton growth rate μ. The next two terms, 4 and 5, are the gain in concentration by aggregation of two smaller particles, and the loss in concentration by aggregation to larger particles, respectively. The last term, 6, is the loss in concentration of aggregates to sinking. In our model, phytoplankton growth (i.e., the first three terms) and the sinking term (i.e., the sixth term) are handled somewhat differently as outlined below. However, we explicitly solve for the gain and loss of particles through aggregation (i.e., terms 4 and 5). These terms are really summations of the stickiness of particles multiplied by a collision kernel multiplied by the product of particle concentrations. These terms are solved at every grid point of the model at every time step for every particle or aggregate size class.

To load or to initiate the aggregation routine, or alternatively, as a front end to the aggregation process, we create a number (10 in our case here) of aggregate size class concentrations as initial conditions and run them through the phytoplankton growth routine as outlined above and in Niebauer and Smith [1989]. In our phytoplankton growth model, chlorophyll is grown in units of mg m^{-3} and not in number of cells or particles. However, we have assumed that 10^5 cells m^{-3} = 0.01 mg m^{-3} chlorophyll so that if there were, for example, 30 cells per aggregate or per "particle", then 0.01 mg m^{-3} chlorophyll would = 3.33 x 10^{-3} aggregates or particles m^{-3}. We have chosen 30 cells per aggregate or "particle" as the smallest particle size so that with 10 size classes the largest particle consists of 300 cells. (As an aside, we have only considered these relatively larger aggregate sizes and a small number of size classes to follow the basic interaction among the physics and biology in aggregation, to get at the vertical flux, and how the larger scale air–ice–ocean interactions interface with aggregation. The next step, which did not appear to be necessary for this project, is to go to the two orders of magnitude more size classes of Riebesell and Wolf-Gladrow [1992]).

Having now fed chlorophyll into the aggregation routine and converted it to concentrations of particles, we then chose a cell diameter of d_1 = 10 µm with which we can calculate the diameters of the particles or aggregates, d_i, via:

$$d_i = d_1 \times i^{0.44} \tag{34}$$

where d_i = aggregate (of size i) diameter and d_1 = cell diameter. Once d_i is calculated, the aggregate settling velocity or particle sinking rate, w_i, is calculated via:

$$w_i = 2.29 \times 10^{-7} \times d_i \times i^{1.17} m\ s^{-1} \tag{35}$$

In our case, for 30 to 300 cells per aggregate, the aggregate diameters are 44.7 to 123.0 µm given a cell diameter of 10 µm. This gives aggregate settling velocities of 1.7 to 5.5 m d^{-1}. The maximum sinking of 5.5 m d^{-1} is a reasonable number although we note that it is more than an order of magnitude less than the maximum rates of ~100 m d^{-1} reported [e.g., Hill 1992]. Instead of using the sinking term (sixth term in

13

(33) above) explicitly to calculate the chlorophyll flux, in our model, when calculating the vertical chlorophyll flux at each grid point, we add the sinking rate to the vertical advection before calculating the flux.

Next we calculate a collision kernel $\beta_{i,j}$, consisting of two parts, one part due to shear flow $\beta^s_{i,j}$ and the other part due to differential settling, $\beta^d_{i,j}$. That due to shear flow can be written:

$$\beta^s_{i,j} = 0.136 \times d^3_{i,j} \times EC_{i,j} \qquad (36)$$

where 0.136 is a constant that depends upon the energy dissipation rate and kinematic viscosity of water, $d_{i,j} = d_i + d_j$ is the sum of aggregate diameters and $EC_{i,j}$ is the contact efficiency or the probability that two aggregates close to each other will come into contact.

The part of the collision kernel due to differential settling can be written:

$$\beta^d_{i,j} = \frac{\pi d^2_{i,j}}{4} |w_i - w_j| \left(EC_{i,j} + ED_{i,j} \right) \qquad (37)$$

where w_i and w_j are the sinking speeds of particles with i and j cells, and $ED_{i,j}$ is the diffusion efficiency [McCave 1975] but which is neglected here because diffusion is negligible for particles $\gg 1$ µm. $EC_{i,j}$ is a theoretical contact efficiency:

$$EC_{i,j}(p) = EC_0 \left(-\frac{0.1}{p} \right) \qquad (38)$$

where $p = d_{min}/d_{max}$ and $EC_0 = 1/\exp(-0.1)$. Finally, we calculate the collision kernel as:

$$\beta_{i,j} = \left(\beta^s_{i,j} + \beta^d_{i,j} \right) \qquad (39)$$

To complete the calculation of these aggregation terms, we multiply by a cell stickiness α. The natural range of phytoplankton stickiness is not well known. In the laboratory, Kiorboe et al. [1990] measured values of 0.001–0.1 which showed some dependence on nutrients. In marine snow aggregates, values up to ~0.9 were obtained [Alldredge and McGillivary 1991] but these aggregates are much more dense than phytoplankton. A sensitivity analysis in choosing a stickiness is presented below after finishing the derivation.

The dC_i/dt as represented by just the aggregation terms in (33) above (i.e., the fourth and fifth terms) are calculated and integrated over the time step, yielding concentrations of aggregates. Then these concentrations, C_i, are proportionally adjusted so that the number of cells before and after the aggregation process do not drift or change (i.e., the number of cells going in = number of cells coming out). Finally, these new C_i are changed back into chlorophyll as mg m^{-3} and sent on to the rest of the model for the advection, diffusion, growth, etc. at the next time step before coming back to be aggregated again.

In order to understand the aggregation routine as well as search for a realistic stickiness, we did a sensitivity study by varying stickiness as a constant between 0.001 and 2.0 over a series of experiments

14

(Table 2). In each experiment, with stickiness held constant, we tracking both primary production (surface 40 m) as well as the vertical flux of carbon through the 250 m level. We did this in a series of eight model runs of ~3 months duration (May–July) with stratification, nutrient and biological conditions similar to the Fram Strait/Greenland Sea ice edge. Basically, for all the runs, maximum primary production occurs at 2 weeks into the experiments at a maximum ~1 g C m^{-2} d^{-1} and falls off rapidly afterward. For the deep vertical flux at 250 m, there is background flux of ~10–15 mg C m^{-2} d^{-1} for the first 5 weeks followed by rapid increases reaching peaks of ~125–180 mg C m^{-2} d^{-1} between weeks 7 and 10.

In general, lower values of stickiness slow the generation of larger, more dense particles and so the increase in the flux at 250 m occurred later in the experiments (Table 2). Maximum flux was less than for higher values of stickiness which speed up generation of larger, more dense particles which sink faster. However, note that maximum flux of ~180 mg C m^{-2} d^{-1} occurred at the intermediate value of stickiness = 0.1.

In looking at the mean daily primary production in the upper 40 m and flux through 250 m, both vs. stickiness (Table 2), we find that primary production over the first 35 days does not vary much but stays relatively close to ~500 mg C m^{-2} d^{-1} for stickiness less than or equal to 0.1 but decreases markedly for larger values. This is again because for larger values of stickiness, particles coagulate quickly and sink too fast to sustain a surface bloom. Likewise, mean daily vertical flux through 250 m for the 7 weeks following the bloom rises with increasing stickiness reaching ~116 mg C m^{-2} d^{-1} for stickiness = 0.1, or ~25% of the mean daily surface primary production. Maximum 250 m flux is ~130 mg C m^{-2} d^{-1} for stickiness = 0.5, which gives a ratio of 31%. (We realize that these ratios in Table 2 may not be very meaningful because they depend on so many variables such as light, nutrients, zooplankton, etc. For example, in some high latitude seas such as the Bering Sea, there often are no zooplankton present during spring blooms because of cold water temperatures, so nearly all of the chlorophyll sinks; whereas in other situations, zooplankton grazing controls the bloom and little falls through.)

Table 2. Stickiness, mean daily primary production in upper 40 m (mg C m^{-2} d^{-1}) for days 0–35, mean daily flux through 250 m (mg C m^{-2} d^{-1}) for days 35–84, and the ratio of flux to primary production as a percent.

Stickiness	Primary Production (0–40 m)	Flux (250 m)	Ratio (%)
0.001	479	9	2
0.01	488	37	8
0.025	493	73	15
0.04	494	91	18
0.1	490	116	24
0.5	424	130	31
1.0	361	126	35
2.0	291	120	41

Stickiness greater than 0.1 was rejected as aggregation is too fast and the surface bloom does not develop well. Stickiness less than 0.01 was rejected as aggregation is too slow and less than 10% of the primary production gets to 250 m. This leaves us with stickiness between 0.01 and 0.1, which is within the range of Kiorboe et al. [1990]. We then refine our selection by using a subjective criteria that there should occur a relative ammonium maximum associated with a relative maximum in zooplankton that occurs in conjunction but lagging the bloom. For stickiness = 0.1 there is a weak ammonium/zooplankton response, moderate for stickiness = 0.04, and stronger for stickiness = 0.025 and 0.01. By this criteria, we dropped 0.1 as too weak and 0.01 as too strong. Within this range, we finally chose stickiness = 0.02 to arbitrarily allow for the possibility of 10% of the primary production to get to 250 m (Table 2).

Both microzooplankton and macrozooplankton ingestion are modeled as a saturation response [Walsh 1975] which incorporated zooplankton biomass, temperature effects, and threshold concentrations of phytoplankton needed to induce feeding. Maximum ingestion rates (I_{max} in time^{-1}) for a known temperature are related to the maximum ingestion rate at 0°C (I'_{max}):

$$I_{max} = I'_{max} e^{QT} \qquad (40)$$

In our treatment we followed the procedure of Kremer and Nixon [1978] who fitted Petipa's [1966] data as a function of temperature to determine the coefficients of (40). In this equation, Q (the temperature rate constant) was equal to 0.12°C^{-1} and $I'_{max} = 0.024\,d^{-1}$.

We included a threshold concentration for zooplankton grazing initiation ($P - P'$) using a hyperbolic relationship for zooplankton feeding:

$$I_{zoo} = I_{max} Z (P - P') / \left[(P - P') + K_z \right] \qquad (41)$$

where I_{zoo} is the ingestion rate, P is the phytoplankton biomass, Z is the zooplankton biomass, P' is the threshold concentration of food required for zooplankton grazing, and K_z is the "half-saturation constant" for grazing. Thus the ingestion rate depends on temperature, food concentration, and the biological response of the zooplankton. In our model, K_z is set at 5 µg chl L^{-1}, and P' at 1 µg chl L^{-1}.

Zooplankton are also divided into two size classes, each of which has different functional characteristics. The smaller class (microzooplankton) feed on nanoplankton (size class 1 in the present model), whereas the larger zooplankton (macrozooplankton) graze on net plankton and microzooplankton (size classes 1–10 in the present model). Both size classes' ingestion is modeled as a saturation response, with different grazing constants and threshold levels. For microzooplankton we use a K_z value of 2.5 µg chl L^{-1} and a threshold concentration of 0.5 µg chl L^{-1}, and for macrozooplankton the K_z and threshold levels are 10 and 1.0 µg chl L^{-1} respectively.

Zooplankton ingestion and growth is not 100% efficient, in that some material is excreted and a large amount is respired. Direct losses by egg production are not treated in this model but are assumed to be part of egestion and vertical flux. Zooplankton excrete ammonium, and the excretion is a constant proportion (i.e., 10% of macrozooplankton and 20% of microzooplankton ingestion is excreted as NH$_4^+$). Zooplankton also egest fecal material which rapidly sinks; furthermore, they suffer some mortality due to predation by higher trophic levels. These losses are accounted for by using a constant proportional loss term equal to 5% of the zooplankton standing stock.

Results

Ice edge ("20") series experiments

This series of experiments address objective 1) To modify an existing numerical model of Arctic waters [Niebauer and Smith 1989; Smith and Niebauer 1993], which includes sea ice as well as biological and nutrient chemistry interactions, to realistically model the vertical flux of phytoplankton as aggregates. These experiments also address objective 2) To model Arctic shelf spring phytoplankton blooms, aggregation and vertical transport of chlorophyll/phytoplankton as a function of physical processes of melt water and/or solar heated surface stratification, wind mixing and wind-driven coastal upwelling of nutrients into the photic zone. These experiments address hypothesis 1) Phytoplankton particle and particle–particle interactions (aggregation) and subsequent sinking provide a dominant pathway for the removal of natural particles, nutrients and carbon from the surface layer. This material goes to the shelf bottom, the Arctic halocline or the deep Arctic basin. These experiments also address hypothesis 2) concerning the effects of variability in environmnetal conditions on primary production.

The basic set of experiments shown here are four simulations starting on 1 May and lasting 4 weeks. The situation is that the ocean is half covered with 1 m of ice. There is no wind applied in these experiments, and density is a function of salinity and temperature only (i.e., no effect from pressure, see Fig. 3). No radiation is explicitly applied so that heat to melt ice comes only from the ocean (i.e., temperatures warmer than $-1.75°C$). The four experiments (hereafter called 20 through 23) presented here are a matrix (Table 3) of model runs with and without melting, and with and without background or deep stratification. The initial conditions were set as outlined in the previous section and the experiments were run for 4 weeks with no other forcing applied.

Table 3. Ice edge ("20") series of numerical experiments.

Experiment	Stratification Initial Condition
20	Isothermal at $-1°C$ (*ice melting*) and isohaline at 32‰ **NO STRAT, MELT**
21	Stratified as in Figure 3 so that there is *no ice melt* **STRAT, NO MELT**
22	Isothermal at $-1.75°C$ (*no ice melting*) and isohaline at 32‰ **NO STRAT, NO MELT**
23	Stratified as in Figure 3 but with temperature at $-1°C$ (*ice melting*) **STRAT, MELT**

As a general overview before getting lost in detail, the two experiments without initial physical stratification in temperature and salinity (i.e., 20 and 22) are characterized by strong vertical diffusion of nitrate into the surface layers (Table 4). This is simply because there is no ocean density stratification

to constrain vertical diffusion in the presence of a strong vertical nitrate gradient ($8~\mu M$ in upper 40 m rising to $16~\mu M$ at 75 m). In general, the increased diffusion of nitrate fuels ~16% higher primary productivity, or carbon fixing, and consequently >40% higher vertical chlorophyll flux back down through the water column (Table 4) than if there had been stratification (e.g., experiments 21 and 23). This higher vertical chlorophyll flux, in turn, leads to an average ~25% lower concentration of primary production (chlorophyll) in surface layers (Table 4). However, the experiment with ice melt and associated ice edge stratification (20) showed the highest chlorophyll concentration when integrated over the upper 40 m (Table 4). Here, the surface density stratification, this time low salinity melt water, lead to higher productivity and production.

In contrast, those experiments with initial (temperature and salinity) stratification (21 and 23; Table 3) are characterized by reduced vertical diffusion of nitrate and therefore lower primary productivity and lower vertical flux of chlorophyll or carbon, but (or thus) because of the density stratification holding material in the upper layer, there are higher concentrations of surface chlorophyll. Again, the exception is the higher value of integrated chlorophyll in experiment 20 (Table 4). (Note that there is little real difference between experiments 21 and 23, meaning that the stratification dominates the other processes.)

18

Table 4. Comparison of nitrate, primary productivity and production concentrations and rates from the ice edge ("20") series of numerical experiments.

Experiment	20 (NO STRAT−MELT)	21 (STRAT−NO MELT)	22 (NO STRAT−NO MELT)	23 (NO STRAT−MELT)
Primary Productivity (gm C m^{-2} d^{-1}, $\int$40m)				
average	0.32	0.22	0.26	0.24
maximum				
(instantaneous)	0.93	0.48	0.69	0.51
(daily average)	0.65	0.31	0.50	0.29
Primary Production				
average	0.93	0.88	0.65	0.98
maximum (mg m^{-3})	3.43	2.28	1.48	2.40
integrated average	37	35	26	39
integrated max (mg m^{-2}, $\int$40m)	105	67	56	71
Vertical Flux (gm C m^{-2} d^{-1}) (% of ave PP)				
average				
50 m	0.14 (44%)	0.08 (36%)	0.15 (59%)	0.08 (36%)
100 m	0.08 (26%)	0.02 (11%)	0.09 (36%)	0.02 (10%)
150 m	0.01 (5%)	0.01 (5%)	0.01 (6%)	0.01 (5%)
maximum @ 50 m (% of max daily ave PP)	0.28 (43%)	0.16 (52%)	0.31 (60%)	0.18 (62%)
Nitrate				
Photic zone				
minimum (µM)	2.8	1.5	8.8	0.9
integrated minimum (µM m^{-2}, $\int$40m)	265	93	356	83
(Initial integrated nitrate started at 160 µM m^{-2}, $\int$40m)				

One can see the details of these generalizations in the comparison of the myriad cross sections and time series (Figs. 4 through 17) from the experiments, but in an effort to avoid getting lost in gruesome detail, consider first data in Figure 4, which are the integrated nitrate, chlorophyll, primary productivity and vertical chlorophyll flux for experiments 20–23. Figure 4 and Table 4 show nitrate levels rising in the upper 40 meters in experiments 20 and 22 (cf., experiments 21 and 23) as a result of vertical diffusion with no stratification. This rise in nitrate results in increased primary productivity, higher vertical chlorophyll flux and, for the first ~2½ weeks, higher integrated total chlorophyll in 20 and 22 (Fig. 4).

However, nitrate concentrations drop over the last ~9 days of 20 (Fig. 4) coincident with increasing (~doubling) primary productivity and increasing (~doubling) integrated chlorophyll. This difference in 20 is caused by ice melt stratification at the edge of the melting ice pack (Figs. 5 and 14). The melt water stratification is holding phytoplankton in the photic zone in the presence of nitrate, resulting in increased primary production (i.e., an ice edge spring bloom). Under the ice, there is sufficient nitrate, stratification and phytoplankton seed populations, but not enough light to bloom. Seaward of the ice edge melt water stratification/front there is sufficient nitrate, light and phytoplankton, but not enough stratification to concentrate the bloom.

This ice edge bloom in experiment 20 appears to substantially gain momentum in the third week of May with the increase in primary productivity, decrease in nitrate and increase in chlorophyll (Figs. 4 and 6). The chlorophyll does not sink/diffuse vertically very quickly because of the ice melt stratification. This lack of sinking is reflected in little change in the vertical flux relative to the other experiments over the last ~9 days of the experiment. The spring bloom gaining momentum in the third week of May is probably reasonable when compared to the Bering Sea, some 10 degrees of latitude (~1000 km) farther south, where ice edge blooms start approximately 3 weeks earlier, around 1 May [Niebauer et. al. 1990]. It is already obvious that the 4 week experiments are not long enough to catch the spring bloom. To address this, a 3-month simulation of 20 is presented in Figures 15, 16 and 17 and discussed below.

Considering cross sections for experiments 20–23 in Figures 5, 7, 9 and 11, notice the concentration of primary productivity and production in the ice edge frontal structure caused by melting ice in 20 (Fig. 5). While there is a hint of similar structure in 23 (Fig. 11, the other ice melt experiment) it is not as strong, due to the background stratification. Note also the circulation in 20 and 23 (Fig. 13) caused by the melting ice. In both cases the currents are weak (maximum ~0.25 to 1.4 km d^{-1} in the horizontal and 0.5 m d^{-1} in the vertical). While these currents are not strong, the cross-ice velocity of ~0.25 km d^{-1} (which is in the off-ice direction) is enough to move ~7 km, or across two grid spaces, in the 4 week duration of the experiment. However, during the experiment, the ice edge stays at the same grid point, but becomes thinner as the ice melts faster than the weak currents can carry it out over the open ocean. In 20 (top panel of Fig. 13) the currents are not restricted by the deeper background stratification (as they are in 23; bottom panel of Fig. 13) and so reach much deeper.

It is probably these vertical currents, combined or interacting with minor inertial oscillations and slight vertical convection (discussed below), all associated with the ice edge, that appear to cause slight disruptions or fluctuations of the chlorophyll flux as shown in Figures 4, 6, 15 and 16. These disruptions are best seen in Figure 16, reoccurring at approximately days 20, 30, 44, 60 and 80. This does not happen in 23 (Figs. 4 and 12) because there is stratification to absorb motion so the currents do not reach as deep. Some of the fluctuations in Figure 16 are inertial oscillations (discussed more fully in the next section on

wind-driven upwelling). But note also that there are no oscillations or fluctuations for experiments 21 and 22 (Figs. 8, 10 and 16) because there are no water currents to force or initiate the motion.

The two experiments with melting ice (20 and 23) produced ice edge frontal structure in all of the fields. However, the frontal structure is much stronger in the experiment with no stratification but with ice melt (experiment 20), at least in part due to the circulation caused by the melting ice in the absence of vertical stratification. Experiment 20 (no stratification but with ice melt) most closely matches observations from field experiments in ice edge blooms (cf., Fig. 2 from Niebauer and Alexander [1985], and Fig. 14). Ice edge blooms begin during the transition between winter conditions (ice formation, unstratified water column, mixing to the bottom and elevated nutrient concentrations) and spring conditions (melting and retreating ice which induce water column stratification and shallow mixed layer) [Alexander and Niebauer 1981; Niebauer and Alexander 1985]. In the Bering Sea (~1000 km to the south) this transition begins in April when the ice begins to retreat. The bloom usually occurs around 1 May when insolation is sufficient and behaves classically in that it is strongly keyed to stratification. It is confined to the shallow surface mixed layer, although the photic zone may be much deeper. The critical depth model proposed by Sverdrup [1953] probably fits. In the absence of stratification, phytoplankton are mixed up and down or in and out of the photic zone so that growth does not exceed the loss terms like respiration etc., and there is no net gain in production. When the surface stratifies, the mixing is stopped, the phytoplankton are held in the surface photic zone where growth exceeds loss, and there is a bloom.

The primary physical difference between the ice edge bloom and an open water spring bloom lies in the mechanism producing the water column stability. At low temperatures (~<4°C), salinity tends to control density (e.g., Fig. 3). Melting ice provides a source of cold, low-salinity water. In open water blooms, temperature usually drives the density stratification. The relationship between temperature, salinity and density can be seen in Figures 3 and 14.

Details of the vertical chlorophyll flux and chlorophyll distribution over time and depth for all four of the experiments are shown in Figures 6, 8, 10 and 12. Concentrating on experiment 20 in Figure 6, the chlorophyll flux is shown increasing with both time and depth as the particles aggregate and become more dense and thus sink faster. Fluxes increase to ~5 mg m^{-2} d^{-1} at approximately 40 m by ~2.5 weeks, at which point the circulation (e.g., Fig. 13), slight convection (Fig. 15) and inertial oscillations combine to cause fluctuations that vary between 8 mg m^{-2} d^{-1} upward to 11 mg m^{-2} d^{-1} downward as the column flips between upwelling and downwelling. For the fourth week, the circulation settles down and apparently the main spring bloom starts. The main spring bloom is driven by insolation, while the first blooming, the ice edge production (Fig. 5), would not have occurred had it not been for ice melt stratification.

By the end of the experiment fluxes reach ~8 mg m^{-2} d^{-1} at ~25 m (Fig. 6). The mean for the whole water column on day 17 is ~2 mg m^{-2} d^{-1} while at day 28 the average is ~2.5 mg m^{-2} d^{-1}. The average over the 4 weeks is ~1.5 mg m^{-2} d^{-1}. To put these values in perspective, the average and maximum chlorophyll values integrated over the upper 40 m for all four experiments are 26–39 mg m^{-2} and 56–105 mg m^{-2} respectively (Table 4). Thus an idea of the vertical fluxes as a percentage of the primary production range from ~4–6% in the mean to ~8–14% at the maximum.

An extended experiment run of 3 months (May, June and July) was conducted for experiment 20 (Figs. 15–17) because it was realized that the 1 month runs did not reach a point of maximum bloom and subsequent post bloom conditions. Note also, the Cota et al. [1996] data are probably post bloom

conditions. Time series from this extended experiment 20 show that maximum primary productivity occurs about day 29 at ~0.6 gm C m^{-2} d^{-1} (Fig. 16). Maximum production or chlorophyll occurs a week to 10 days later at magnitudes >4 mg m^{-3} (Fig. 15) and 130 mg m^{-2} (Fig. 16). Maximum chlorophyll flux (Fig. 15) lags the chlorophyll maximum by a few days, occurring at about days 38–41 at ~20 m at a magnitude of 11–12 mg m^{-2} d^{-1}. This chlorophyll flux is ~9% of the integrated chlorophyll maximum. Finally, the maximum vertical carbon flux through 50 m (Fig. 16) occurs somewhere around day 42 at >0.4 gm C m^{-2} d^{-1}. This is almost 70% of the maximum primary production, and lags by ~2 weeks, which gives an average sinking rate of ~3.5 m d^{-1}.

Again, there are the interesting minor fluctuations mentioned earlier that show up in the chlorophyll flux (Fig. 15) along a line from 50 m at day 21 to 100 m at day 70, and also in vertical carbon flux (Fig. 16) at about days 29, 43, 59 and 78. In the chlorophyll flux, these fluctuations range from –18 to +25 mg m^{-2} d^{-1} around an average of ~–5 mg m^{-2} d^{-1}. It turns out that these fluctuations coincide with some minor convection (<0.5 m d^{-1}) that can be seen in the sigma-t time series (Fig. 15), and that this zone of chlorophyll flux variability coincides with the instabilities in the sigma-t (Fig. 15). The grid point or column where this is being sampled is not overlain by ice, but it is only 3 km off the ice. The ice is melting and the melt water is advected out over the open water (e.g., Figs. 5 and 14). Inspection of the temperature, salinity and sigma-t time series data (Fig. 15) shows that initially the cooling of the water has a greater effect on density than does the freshening so that the water becomes slightly unstable and convects. The dominance of cooling over freshening seems to last until about day 21, at which point the fluctuations in the chlorophyll flux begin. However, the subsurface instability lasts from ~day 21 to ~day 49. This instability, plus the ice edge advection, appears responsible for the fluctuations. It is suspected that this may not happen in nature, or is hard to observe, as it is probably overpowered by stronger events such as wind, waves, large scale advection, etc. For example, in the Arctic it is unlikely that there would be no wind for a period of 3 months.

Finally, Figure 17 shows the distribution of size classes of chlorophyll particles (i.e., aggregates) over time at three depths of 50, 100 and 250 m. In general, the smallest size class is most abundant toward the surface while, with time and depth, aggregation of particles results in higher concentration of larger size particles. If we consider for the moment just the largest size particle (particle size class 10) in Figure 17, and the plot labeled "CHLOROPHYLL (c10, mg/m3)" in Figure 15, we can see how the data sets relate. The data in the "PARTICLE SIZE CLASS 10" in the top panel of Figure 17 are the same data which would be selected by a line drawn across Figure 15 at 50 m. Likewise, the data in the "PARTICLE SIZE CLASS 10" in the middle panel of Figure 17 are the same data in a line drawn across Figure 15 at 100 m, and so on, with the bottom panel in Figure 17 reflecting a line of data at 250 m in Figure 15. The maximum concentration in the largest particle size reaches 50 m at about day 49, 100 m at ~day 70, and it appears as though the concentration is still increasing at 250 m by the end of the experiment at day 84. For the smallest size class, the maximum is found in the surface but is practically nonexistent at the bottom. This is in most part due to the largest size particles sinking more than five times faster than the smallest particles.

In an effort to verify model results to see if they make sense, observational data from various sources, primarily Cota et al. [1996], are compared with model results. The Cota et al. [1996] data come from an oceanographic cruise in August 1993 in the eastern Chukchi Sea in ice infested waters off Point Barrow. Their observations probably provide some of the best data for comparison. Their data are not necessarily from a distinct ice edge but they note that the average ice cover during the cruise in August was >50%.

Table 5 shows some of their data while Table 6 has been included for comparison with concentrations and rates for other ice infested regions of the ocean.

It should be noted that while there is reasonable comparison between model and observed data in many cases, it does not mean that the model is necessarily correct. Models can always be "tuned" to get things right. Not much tuning has been done here but rather the effort has been to use modeling to try to understand the dynamics and kinematics. Still, one must be in the ball park. More will be addressed in the Discussion.

Table 5. Primary productivity and production (chlorophyll) from the Chukchi Sea in August. [after Cota et al. 1996].

Depth (m)	Chlorophyll ($mg\ m^{-3}$)	Primary Productivity ($mg\ C\ m^{-3}\ h^{-1}$)
2	0.26 to 0.48	0.24 to 0.52
4	0.27 to 0.49	0.35 to 0.77
7	0.27 to 0.47	0.36 to 0.76
11	0.34 to 0.56	0.36 to 0.76
17	0.45 to 0.79	0.47 to 0.87
25	0.69 to 1.07	0.25 to 0.29
39	0.49 to 1.25	0.00 to 0.00
Integrated (40m)	18.7 to 34.3 mg m^{-2}	10.64 to 19.17 mg C $m^{-2}\ h^{-1}$ 0.26 to 0.46 gm C $m^{-2}\ d^{-1}$

Table 6. Comparison of nutrient, primary productivity and production concentrations and rates from various polar seas [after Niebauer 1991].

	Nitrate sfc μM	Nitrate max μM	Chl sfc mg m^{-3}	Chl max mg m^{-3}	Chl $\int$40 mg m^{-2}	PP max g C m^{-2} d^{-1}	PP g C m^{-2} y^{-1}
Models	~1	4	1.5	3.4	37–105	0.7–0.9	~24
Arctic "Cota"	0.1	5	~0.5	>3.5	~34	0.95	–
Bering Sea ice edge	<1	>25	22–25	27–41	~680	6.6	309
Bering Sea no ice	<1	>25	17–29	33–47	~950	4	204–350
Bering Strait no ice	1–20	1–20	16	–	–	10	–
Fram Strait ice edge	<1	12	4	15	~112	1.7	–
Weddell Sea ice edge	12	26	15–20	15–20	–	–	<1
Ross Sea ice edge	5–9	25–29	3–4	4	~140	–	1
Barents Sea ice edge	0	12	2–8	2–8	–	1.5–5.3	6–80
Arctic ice pack	–	–	–	1	–	–	13–38
Arctic shelves	–	–	–	–	–	–	27

For the primary productivity (Table 5) Cota et al. [1996] integrated rates averaged ~0.30 gm C m^{-2} d^{-1} with a standard error range of 0.21–0.38 gm C m^{-2} d^{-1}. Maximum and minimum rates were 0.95–0.05 gm C m^{-2} d^{-1}. The model data for 20 (Table 4) were 0.32 gm C m^{-2} d^{-1} with a maximum daily average of 0.65 gm C m^{-2} d^{-1}. For annual Arctic Ocean rates, Pomeroy [1997] suggests an annual primary productivity of 13–38 gm C m^{-2}. If 80 days as the summer is assumed at this latitude, then for model run 20, the annual primary productivity is ~24 gm C m^{-2}. It is interesting to note that this last annual rate is arrived at whether primary productivity from Figure 4 (28 days) or from Figure 16 (84 days) is used.

Cota et al. [1996] measured a chlorophyll average of ~0.66 mg m^{-3} in the upper 40 m with a standard error range of 0.47–0.86 mg m^{-3} (Table 5). Maximum concentrations of >3 mg m^{-3} were measured on the shelf. The model data for 20 averaged ~0.93 mg m^{-3} with a maximum of 3.43 mg m^{-3} (Table 5).

Integrated chlorophyll (over 40 m) for Cota et al. [1996] was ~26.5 mg m^{-2} with a standard error range of 18.7–34.3 mg m^{-2}. For 20, the average integrated chlorophyll was 37 mg m^{-2}, while the maximum by the end of the experiment was 105 mg m^{-2}. Note that 105 mg m^{-2} requires an average chlorophyll of 2.6 mg m^{-3}.

Cota et al. [1996] measured a minimum nitrate of ~0.1 μM in the surface layers, suggesting that any further production was not being fueled by nitrate. However, an estimate of the integrated nitrate in the upper 40 m gives ~100 μM m^{-2}. The best model fit was 23, which includes both background stratification and melt water stratification, with minimum and integrated nitrate of 0.9 μM and 83 μM m^{-2} respectively.

As can be seen from Table 4, the average vertical flux of carbon (as aggregates of phytoplankton) through 50 m was on the order of 0.14 gm C m^{-2} d^{-1} when there was no stratification (20 and 22). This compares with about half this, or ~0.08 gm C m^{-2} d^{-1}, for those with background stratification (21 and 23). In the cases with no stratification to modify vertical diffusion and flux, these fluxes represent 44–59% of the average primary production. With stratification, the fluxes represent ~35% of the primary production. At the end of the 28 day experiment (i.e., 28 May), the instantaneous fluxes were 0.16–0.31 gm C m^{-2} d^{-1}.

Again, for comparison, flux observations from March to August 1997, in the Bering Sea [S. Henrichs and J. Goering at the University of Alaska, pers. comm.] ranged from 0.01–0.15 gm C m^{-2} d^{-1} in sediment traps moored at 40 m. The average was 0.05 gm C m^{-2} d^{-1}. These fluxes were collected under primary production of ~0.15 gm C m^{-2} d^{-1}, and so the fluxes may represent 7–100% of the primary production. Again, we caution that the Bering Sea is a different system some 1000 km farther south. Smith and Dunbar [1998] reported fluxes of 2–92 mg C m^{-2} d^{-1} for the Antarctic Ross Sea which is more comparable to flux through 100 and 150 m in our case (Table 4).

Coastal upwelling ("50") series experiments

This series of experiments addresses objective 2) To model Arctic shelf spring phytoplankton blooms, aggregation and vertical transport of chlorophyll/phytoplankton as a function of physical processes of melt water and/or solar heated surface stratification, wind mixing and wind-driven coastal upwelling of nutrients into the photic zone. These experiments address hypothesis 1) Phytoplankton particle and particle–particle interactions (aggregation) and subsequent sinking provide a dominant pathway for the removal of natural particles, nutrients and carbon from the surface layer. This material goes to the shelf bottom, the Arctic halocline or the deep Arctic basin. Specifically, wind-driven coastal upwelling can drive ice away from the coast, forming polynyas allowing sunlight into surface layers where, in the presence of upwelled nutrients, primary production is enhanced. This production aggregates and sinks, carrying material to the shelf bottom, the Arctic halocline or the deep Arctic basin. This set of experiments also addresses and is motivated by large scale wind events where large areas of the ice covered ocean are suddenly opened up to the atmosphere (e.g., Fig. 18). In this sense these experimants also address hypothesis 2) concerning the effects of variability in environmental conditions on primary production.

The basic set of experiments shown here consists of simulations starting on 1 May and lasting 4 weeks. The experiment matrix is four experiments with and without ice, and with and without winds (Table. 7). In all of the experiments, the left end of the section is closed so that it acts like a coast. When ice is present as an initial condition, it provides a complete cover of 1 m thickness. When there is wind, the

wind stress is 1 dyne cm^{-2} parallel to the coast with the coast to the left of the wind (i.e., off-shore Ekman transport). The wind is applied uniformly in time and space on day 6 for 24 hours. (1 dyne cm^{-2} is ~8 m s^{-1} or ~16 kt.) There is stratification in all of the experiments and density is a function of salinity and temperature only (i.e., no effect from pressure, Fig. 3). No insolation is applied and the water is cold enough that there is no melting of ice.

Table 7. Coastal Upwelling ("50") series of numerical experiments.

Experiment	Initial and Boundary Conditions
50	TS as in Figure 3, **ICE, WIND** on day 6
51	TS as in Figure 3, **NO ICE, WIND** on day 6
52	TS as in Figure 3, **NO ICE, NO WIND**
53	TS as in Figure 3, **ICE, NO WIND**

As a general overview, the experiments with ice cover (50 and 53) show little biological activity as long as ice blocks out the sun. This includes the first 6 days of experiment 50 before wind is applied, and all of 53. The experiments without any ice cover (51 and 52) yield higher levels of nitrate drawdown, primary production and productivity as well as higher vertical carbon flux. These are basic spring blooms. Again, this is no surprise as there is nothing to block the sunlight. The only exception to this is the observation that by the end of experiment 50 (ICE, WIND; Table 7), primary productivity rates had exceeded all of the other experiments. This is basically due to the initial ice cover blocking light and holding back the spring bloom at a time when the sun is lower in the sky (early May) and insolation is lower, then opening up, via wind, when insolation is stronger and the nutrients are upwelled into the photic zone.

The experiments with wind (50 and 51) show an injection of nitrate into the photic zone due to upwelling, resulting in higher levels of primary production and productivity. However, the bloom in experiment 50 lags behind experiment 51 (also 52) because, as noted above, the ice is not removed until the end of the first week of the experiment when insolation is greater.

As before, one can see these generalizations in the comparison of experimental results (Figs. 19–23, and Table 8), but again, in an effort to avoid getting lost in detail, first consider data in Figure 19 which are the integrated nitrate, chlorophyll, primary productivity and vertical chlorophyll flux for the experiments 50–53. Figure 19 shows nitrate levels diffusing upward in the upper 40 meters in experiment 53 because there is no biological uptake due to ice cover blocking the sunlight. In all of the other experiments, nitrate decreases due to biological uptake. In 50 and 51, the 24 hours of upwelling is reflected in the sharp increases in nitrate on day 6.

Table 8. Comparison of nitrate, primary productivity and production concentrations and rates from the coastal upwelling ("50") series of numerical experiments.

Experiment	50 (ICE–WIND)	51 (NO ICE–WIND)	52 (NO ICE–NO WIND)	53 (ICE–NO WIND)
Primary Productivity (gm C m^{-2} d^{-1}, $\int$40m)				
average	0.16	0.25	0.22	0.0
maximum				
(instantaneous)	0.54	0.52	0.48	0.0
(daily average)	0.37	0.31	0.31	0.0
Primary Production				
average	0.5	1.03	0.6	0.05
maximum (mg m^{-3})	1.9	2.5	0.88	0.14
integrated average	20	41	35	2
integrated max (mg m^{-2}, $\int$40m)	58	75	68	8
Vertical Flux (gm C m^{-2} d^{-1}) (% of ave PP)				
average				
50 m	0.02 (13%)	0.08 (33%)	0.08 (37%)	0.01 (nan)
100 m	0.01 (7%)	0.02 (10%)	0.02 (11%)	0.01 (nan)
150 m	0.01 (7%)	0.01 (4%)	0.01 (5%)	0.01 (nan)
maximum @ 50 m (% of max daily ave PP)	0.04 (12%)	0.20 (65%)	0.17 (56%)	0.02 (nan)
Nitrate				
Photic zone				
minimum (μM)	2.8	1.0	3.7	4.0
integrated minimum (μM m^{-2}, $\int$40m)	152	102	91	206
(Initial integrated nitrate started at 160 μM m^{-2}, $\int$40m)				

In the total chlorophyll (primary production) and primary productivity (Fig. 19), one can see the hierarchy of the effects of ice and wind. For the most straightforward, if not trivial, experiment of ice with no wind (53), primary production is zero and thus the method by which the initial condition chlorophyll disappears is by sinking out of the surface layers. For the experiment in which the ice is opened in the upwelling process (50), and the no-ice experiments (51 and 52), chlorophyll levels reach 58–75 mg m^{-2} (Table 8) with production rates of 0.31–0.37 mg C m^{-2} d^{-1}. Neglecting 53 as trivial; of the other experiments 50–52, the lowest levels of chlorophyll and primary productivity are associated with 50 where the bloom is held back, in time, by ice cover. However, once the ice cover is blown off, the rate of change or slope in 50 (Fig. 19) tends to be steeper than in 51 and 52. In fact, the productivity in 50 exceeds 51 and 52 during the last week in the experiment (0.31 vs. 0.37 mg C m^{-2} d^{-1}, Table 8 and Fig. 19). In comparing just the no-ice experiments (51 and 52), the wind-driven upwelling nutrient increase in 51 drives higher primary productivity resulting in slightly higher chlorophyll concentrations. These increases due to upwelling are 12–17% as calculated from Table 8.

Finally, in looking at the vertical carbon flux in Figure 19, for 53 there is very little as there is no primary production. Experiments 50 and 53 are identical (~0) until the ice opens on day 6. In fact, on day 6 in 50 (as well as 51), the flux becomes slightly positive indicating upward flux due to the upwelling. By the end of the experiment, the flux in 50 is 0.04 gm C m^{-2} d^{-1} which is ~12% of the average primary production (Table 8). The vertical flux in 51 and 52 is much higher at 0.17–0.20 gm C m^{-2} d^{-1}, which is 56–65% of the primary productivity. Again, the highest levels are in 51 which is the no-ice experiment with the added wind-driven nutrient kick.

In looking at some cross sections in closer detail for these experiments (Figs. 20, 22 and 23), notice the upwelling structure in the density and nutrient fields after 1 day of upwelling. Notice also that the ice is being pushed away from the coast. This opens up the coastal region to bloom conditions of primary productivity of 0.05 gm C m^{-2} d^{-1} (Fig. 19) with maximum values of ~0.1 mg C m^{-3} h^{-1}. Maximum chlorophyll is ~0.15 mg m^{-3}. These levels are low when compared to Cota et al. [1996] who measured rates of ~0.30 gm C m^{-2} d^{-1} and 0.6 to 0.7 mg C m^{-3} h^{-1} with chlorophyll levels of 0.4 to 0.9 mg m^{-3}. However, our data are collected just as the winds are turned off. By the end of the experiment (e.g., Figs. 19 and 21, and Tables 5 and 8) model data do rise to the Cota et al. [1996] field observations. In Figure 20, the under ice activity is zero although chlorophyll levels look elevated due to the aggregating and sinking of the initial condition concentrations. Actually, there is a build up of chlorophyll on the bottom that has reached 0.43 mg m^{-3}.

Figures 22 and 23 illustrate the current fields for 50 (ICE, WIND) and 51 (NO ICE, WIND). The upwelling, offshore Ekman transport and coastal jet associated with sloping isopycnals (Fig. 20), are indicative of classic coastal upwelling. In 51 (Fig. 23), without ice, the upwelling velocities are a maximum of ~13–14 m d^{-1} with several large areas of 2 m d^{-1}. The offshore Ekman transport speeds are ~10 cm s^{-1} falling off to ~4–5 cm s^{-1} farther from the coast. The along-shore velocities in the coastal jet are ~7 cm s^{-1}, while the speeds farther offshore are ~1–4 cm s^{-1}.

Including the moveable ice cover as in experiment 50 (Fig. 22) intensifies the circulation. This is because the transfer of stress from the wind to water is modeled as approximately twice as efficient when the stress goes from wind to ice and then to water than if the stress goes straight from wind to water (see Methods). So in 50, with ice, the upwelling velocities are a maximum of ~13–14 m d^{-1} (~same as 51) but with several areas of 6 m d^{-1}. The offshore Ekman transport speeds are ~6–7 cm s^{-1} right at the coast but

rise offshore under the ice to ~15 cm s^{-1}. The along-shore velocities in the coastal jet are ~10 cm s^{-1} while the speeds farther offshore are ~6–7 cm s^{-1}.

To frame the cross sections in Figures 20 and 22 against the full 28 day experiments, Figure 21 shows time series of the total chlorophyll and chlorophyll flux as well as the largest size class of chlorophyll aggregates, and nitrate. Ice covers the ocean until day 6 when the wind is turned on for 24 hours. The ice is mostly blown off by day 7. The upwelling is illustrated in both the displacement of nitrate toward the surface and upward directed chlorophyll flux during day 6. After the upwelling, a bloom forms but does not really gain momentum until approximately a week later. By day 14, chlorophyll is accumulating coincident with nitrate uptake and increased downward chlorophyll flux. In the time series of the largest chlorophyll aggregate (c10), an initial blob of particles forms after day 7, sinks, and disappears in the fourth week. The accumulation can be seen on the bottom. But in days 26–28, another particle cloud is forming at 50 m, driven by the increasing surface productivity and production.

Convection ("70") series experiments

This last set of experiments addresses objective 3) To model the vertically downward transport of water, both in conjunction with and as a separate process from the flux of natural/primary production particles and particle aggregation. This physical emphasis includes modeling higher density surface water formation and deep convection through processes such as ocean surface cooling, ice formation and brine rejection, and possible interaction with eddies. These experiments address hypothesis 1b) Phytoplankton particle aggregation and subsequent sinking provide a dominant pathway for the removal of natural particles, nutrients and carbon from the surface layer. Specifically, during ice formation, polynyas (events) and larger ice-spreading events (e.g., Fig. 18) when open water is exposed to freezing temperatures, ice formation causes brine rejection and downward convection of cold, salty, dense water carrying material to the benthos and into the Arctic Ocean halocline. An important factor in this convection is the effect of pressure on temperature and salinity, hence density. These experiments also address hypothesis 2) concerning the effects of variability in environmental conditions on primary production.

Some of the motivation for these experiments comes from Figure 18 as well as Weingartner et al.'s [1998] observations and analysis of winter water mass modification processes on the northeast Chukchi Sea shelf leading to dense water production.

The basic set of experiments are simulations (again) starting on 1 May and lasting 4 weeks. There are six experiments (Table 9), each with 1 m of ice across the entire section as an initial condition. All experiments are quiescent for the first day, followed by application of cyclonic winds for 48 hours (days 2 and 3) to generate divergence of the ice cover and cyclonic eddy-like motion in the water, resulting in upwelling. The wind stress is 1 dyne cm^{-2} which is ~8 m s^{-1} or ~16 kt.

The first experiment is conducted with density as a function of temperature and salinity, or TS (70 in Table 9), while in 71, density is a function of temperature, salinity and pressure, or TSp. In the next two experiments (72 and 73), cooling of the surface waters was applied for 4 days (days 4–7) following the cyclonic winds. The cooling is ~800 watts m^{-2}, equivalent to an air temperature of about –20°C over sea water near freezing, and causes ice formation. As in the first two experiments, these runs are done with density a function of TS (72), and with density a function of TSp (73).

The last two experiments, 74 and 79, are similar to 73 except that the initial water conditions are isothermal (−1.7°C) and isohaline (32 psu). Also in 74, density is a function of TSp, while in 79, density is a function of just TS. However, this does not mean that the water is isopycnal in 74, as the density is also a function of pressure (Fig. 3). Also, the water does not remain isothermal and isohaline in either 74 or 79 due to the effects of cooling and brine rejection during ice formation.

Table 9. Convection ("70") series of numerical experiments.

Experiment	Initial and Boundary Conditions
70	TS as in Figure 3, **ICE, CYCLONIC WIND** on days 2–3 **NO COOLING, PRESSURE** ≡ 0
71	TSp as in Figure 3, **ICE, CYCLONIC WIND** on days 2–3 **NO COOLING, PRESSURE** ≠ 0
72	TS as in Figure 3, **ICE, CYCLONIC WIND** on days 2–3 **COOLING/ice formation on days 4–7, PRESSURE** ≡ 0
73	TSp as in Figure 3, **ICE, CYCLONIC WIND** on days 2–3 **COOLING/ice formation on days 4–7, PRESSURE** ≠ 0
74	Isothermal and isohaline, **ICE, CYCLONIC WIND** on days 2–3 **COOLING/ice formation on days 4–7, PRESSURE** ≠ 0
79	Isothermal and isohaline, **ICE, CYCLONIC WIND** on days 2–3 **COOLING/ice formation on days 4–7, PRESSUR E** ≡ 0

For a general overview as done in previous sections, experiments 70 and 71 can be lumped together as can 72 and 73, while 74 and 79 have similarities. Experiments 70 and 71 are cases of no biological production while there is ice cover followed by a strong bloom when the wind opens up the ice and upwells nutrients into the photic zone. Experiments 72 and 73 exhibit minor biological production following the cyclonic winds on days 2 and 3, but the production drops to near zero under ice formation over days 4–7 and remains near zero for the duration of the experiments because of the ice. There is some convection associated with instabilities caused by the ice formation and rejection of salt in 72 and 73. In none of the first four cases does the density as a function of pressure make much of a difference. However, in the last two, 74 and 79, with less density stratification, after a few days of surface cooling leading to ice formation and brine rejection, deep convection is observed. The difference between 74 and 79 is that when density is a function of pressure, the convection is stronger.

As before, one can see these generalizations in the comparison of experimental results (Figs. 24–32), but again, as before, in an effort to avoid getting lost in detail, consider first Figure 24 which shows the integrated nitrate, chlorophyll, primary productivity and vertical chlorophyll flux for the six experiments. Figure 24 reinforces what was stated above for 70 and 71 (winds but no cooling) tracking together, 72

and 73 (winds with subsequent cooling) tracking together, and finally 74 and 79 (winds, cooling but less stratification) tracking together except for nitrate and the vertical carbon flux. When density is a function of TSp (74), the maximum vertical flux of carbon is more than twice as strong then when density is a function of TS (79).

In more detail: experiments 70 and 71 are basically blooms caused by winds opening the ice canopy (Figs. 25 and 26) and upwelling nutrients on days 2 and 3 (Figs. 24 and 25). The nitrate is subsequently drawn down by primary productivity, resulting in accumulation of chlorophyll leading to increased vertical flux of carbon (Figs. 24 and 25). Figure 26 is a time series of wind-driven ice and water showing the ice canopy opening up and the upwelling. The wind stress is 1 dyne cm^{-2} which is ~8 m s^{-1} (~16 kt); it is applied at the beginning of day 2 and is turned off at the end of day 4. These winds are driving ice at speeds of ~20 cm s^{-1} and ~30 cm s^{-1} in the cross-ice (Ekman) and long-ice directions respectively. The corresponding speeds for water under the ice are ~9 cm s^{-1} and ~12 cm s^{-1} in the cross-ice and long-ice directions respectively. Upwelling velocities are on the order of 6 m d^{-1} with a maximum of 27 m d^{-1}. (Note that to this point, all six experiments are essentially identical.)

Experiments 72 and 73 are basically blooms that begin in the upwelling/opening of the ice but are then thwarted by the cutting off of light by re-growth of the ice under the cooling conditions over days 4–7. The ice conditions are similar to the ice shown in Figures 27 and 28. There are some small instabilities caused by the brine rejection that do cause some convection with maximum speeds of 7 m d^{-1} in 72 and ~9 m d^{-1} in 73. (Note that these vertical velocities are different than the gravitational sinking rates of the aggregated particles, which in all these experiments are a maximum of ~5 m d^{-1}. However, the sinking rates of the particles are always modified by the vertical advection.

In experiments 74 and 79, the vertical density gradient is reduced by making the initial water column isothermal and isohaline in order to more easily induce convection. However, in 74 there is still a density gradient caused by pressure (Figs. 27 and 29). In both 74 and 79, the only way salinity and temperature are changed is by cooling the surface, causing ice to form and resulting in salt rejection. This occurs over the period of day 4 through day 7 (Figs. 27 and 29 for 74; Figs. 31 and 32 for 79).

For experiment 74, early on day 5, convection is ~9 m d^{-1} while by mid-day convection has increased to ~26 m d^{-1}. By early the next day, on day 6, convection is ~155 m d^{-1}, finally reaching a maximum mid-day 6 at ~365 m d^{-1}. Snapshots at the point of maximum convection at day 6.4 are shown in Figures 27 and 28, with the time series shown in Figure 29. The penetrative convection subsides quickly, well before the cooling is shut off at the end of day 7. The ice sub-model insulates the water as a function of ice thickness and thus freezing and brine rejection will eventually stop. By mid-day 6, the ice has grown to ~65 cm, undoubtedly accounting for at least some of the reduction in convection.

The main difference between 74 and 79 is that when density is a function of TS only and pressure is not included as in 79, the vertical convection is significantly reduced. The difference in density can be seen in comparing Figures 27 and 29 with Figures 31 and 32. In comparing Figures 28 and 30, the maximum vertical convection is ~199 m d^{-1}, or a little more than 50% of the maximum in experiment 74. In comparing the vertical fluxes in Figure 24, the maximum flux in 79 (~0.09 gm C m^{-2} d^{-1}) is half that in 74 (~0.18 gm C m^{-2} d^{-1}).

What is happening in experiment 74 is that because the vertical density has been reduced by making the water isothermal and isohaline, the surface water has become dense enough to force convection deep enough so that pressure augments or controls density and penetrative convection begins. That is, there is a buoyancy acceleration downward driven by pressure causing density to increase with greater depth. An analogy (not exact) in the atmosphere is in a thunderstorm or hurricane where water vapor laden air is lifted high enough to force enough cooling to cause condensation. In this case, the change of state of water vapor to rain releases latent heat which accelerates the process.

In experiment 74, at the maximum speed of 365 m d^{-1}, this dense water can reach the Arctic halocline in 3–4 hours, and the 300 m depth of the model in less than one day. This is illustrated in Figures 27–29. Cross-sectional snapshots taken at day 6.4 (Fig. 27) show the convection effects on/of temperature, salinity, density and along-ice velocity as well as nitrate, chlorophyll, chlorophyll flux and primary productivity. The baroclinic geostrophically driven horizontal currents are >15 cm s^{-1} while the convective velocities of >300 m d^{-1} are shown in Figure 28 at maximum penetrative convection. The effect on primary productivity is basically where ice is thick, productivity is low and where ice is thin and light can get into the water, primary productivity is higher. In all of the snapshots, there appear to be double convective plumes. In the model this depends on grid spacing and over which grid spaces cooling is invoked.

The last paragraph basically also describes the results of experiment 79 (Figs. 30–32). The only real difference is that the values of vertical convection and flux are halved because pressure effects are not aiding the vertical convection.

Finally, the time series in Figure 29 for experiment 74 and Figure 31 for experiment 79 show where the convection is obvious between days 4–7. For 74, the vertical carbon flux is not very high at ~0.18 gm C m^{-2} d^{-1} but it is ~9 times greater than the primary productivity of ~0.02 gm C m^{-2} d^{-1} (Fig. 24). Again, these numbers are approximately half for experiment 79.

Discussion

The significance and relevance of this project are related to several CMI Framework Issues, which are similar to objectives of a major, new, joint National Science Foundation/Office of Naval Research program entitled "Western Arctic Shelf Basin Interactions (SBI). SBI is slated to start in 2002 and last 7–10 years in the region of interest in the Chukchi/Beaufort Seas. The reason for pointing this out is that this SBI project will greatly enhance and expand our small effort in modeling in addition to doing much more in the area of field observations. To help frame our particular project against the CMI/BSI goals and to quote from the BSI Announcement of Opportunity (AO), "... studies of shelf/slope water mass modification and exchange processes and biogeochemical cycles are a priority for improving our capacity to predict environmental change. The topics are particularly important because they profoundly influence the thermohaline and biogeochemical structure of the Arctic Ocean." The Shelf Basin Interactions "... program will focus on shelf/slope water mass modifications, material fluxes and biogeochemical cycles in the Chukchi/Beaufort Seas and adjacent slopes/basins, and the ultimate generalization of these results into pan-Arctic and global models". Further in the BSI AO it is stated, "The shelves profoundly influence the thermohaline structure and maintenance of the ice cover of the Arctic Ocean. These same

processes must markedly affect biogeochemical cycles and the biological productivity that support the living marine resources of the Arctic Ocean. However, a mechanistic understanding of the processes that affect the magnitude and rates of biological production, physical and chemical modification of shelf and slopewater masses, and water–mass exchange with the central basin is lacking."

In this context and relevant to the CMI goals, and to the modeling, a sensitive issue in the Arctic is the potential for contamination of the shelf and basin waters and benthos by a variety of petrochemicals from mining and oil exploration, development and transport. Although beyond the scope of this present proposal, we eventually plan to incorporate interaction/aggregation of natural and anthropogenic particles or material into the present biophysical model which should provide information into the fate and modes of transport of this material, as well as provide a description of the transfer between surface and subsurface waters. In addition, modeling should lead to more efficient use of field experiment resources, such as ships, to field test hypotheses. For example, approximately 25% of the shelf area of the world ocean is in the Arctic. There is not enough money or ships to cover this area. Here again, the NSF/ONR BSI project will greatly help.

Of the four objectives listed in the original proposal, the first objective was to modify our numerical model of Arctic waters [Niebauer and Smith 1989; Smith and Niebauer 1993] to realistically model the vertical flux of phytoplankton as aggregates of cells. This objective, which really has two parts, has basically been met. The first part was to get the particles or cells to aggregate realistically, while the second part was to model the vertical flux of the various particle size classes realistically with the larger, more dense particles sinking faster. A problem or constraint is that if the particles aggregate too quickly and sink out of the photic zone too fast, the bloom is extinguished for lack of light as shown in the Methods section above. If the particles aggregate too slowly, the bloom sinks too slowly, contrary to observations.

For the experiments, 10 size classes were used, with particles ranging from 30 phytoplankton cells per aggregate (or cells per particle) to 300 cells per particle. For a single cell of size 10 μm, this gives a particle diameter range of 45–123 μm and a corresponding sinking range of ~1.7 to 5.5 m d^{-1} [Riebesell and Wolf-Gladrow 1992]. We have run many numerical experiments (see Methods above) to "tune" the aggregation parameter "stickiness" which dictates how rapidly smaller, slower sinking particles aggregate to form larger, faster sinking particles. The results of tuning experiments were compared with available experimental and observational data [e.g., Kiorboe et al. 1990] in choosing a stickiness of 0.025. As regards the actual sinking rates, open ocean estimates range from almost zero to >100 m d^{-1} [e.g., Hill 1992] to as high as 250 m d^{-1} [Gardner 1997]. Sinking data from ice related blooms is sparse and sinking observations are not available for the Chukchi/Beaufort Seas. However, we do have data from ice edge related blooms on the Bering Sea shelf which suggest sinking rates of ~7 m d^{-1} [Niebauer et al. 1995] and sinking rates ~5.5 m d^{-1} from the Ross Sea in the Southern Ocean [Smith and Dunbar 1998]. Future work will include increasing the number of size classes and raise the maximum particle diameter to ~500 μm to better fit the range of size of particles observed in the ocean [e.g., Gardner 1997]. This will also expand the maximum sinking speed to ~30 m d^{-1}.

The second objective was to model Arctic shelf spring phytoplankton blooms. This includes the blooming, aggregation and vertical transport of chlorophyll/phytoplankton as a function of physical processes of melt water and/or solar heated surface stratification, and wind mixing and wind-driven coastal upwelling of nutrients into the photic zone. We have been successful in modeling the heat driven

33

melt water stratification generating an ice edge spring phytoplankton bloom ("20" series of experiments) with subsequent aggregation of phytoplankton into larger, denser particles which sink faster. We have also been successful at modeling the coastal upwelling in ice infested waters ("50" series of experiments).

One way to consider these various series of experiments is to ask the question: What was right and what was wrong with the model/results? As regards the "ice edge" experiments, the modeling seems to have gotten much of the ice edge bloom right without a great deal of tuning of the model, at least when compared with results from the Bering Sea. A problem here is that there are not yet observations of a spring/ice edge bloom in the higher latitude Chukchi Sea. However, the productivity and production values from the model seem to relate well to the summer data from Cota et. al. [1996] for the Chukchi Sea. One process that is undoubtedly important but which we have not yet modeled is the vertical mixing of phytoplankton up and down, or in and out of the photic zone. This supposedly results in no net production until stratification stops the mixing and holds the phytoplankton in the photic/upper mixed layer. This requires a wave model and is being worked on.

The ice sub-model seems to work adequately in allowing the ice to melt to give a salinity-based surface stratification. The ice model also works adequately to limit light under the ice as a function of ice thickness and amount of cover.

The aggregation sub-model seems to work reasonably well in modeling vertical flux of the chlorophyll and carbon. The big problem again is that there are few data to verify the results. The values we quoted from the Bering Sea and the Ross Sea are in the same range as the modeling results. Again, flux in the Bering Sea is probably different from that in the Chukchi Sea. Another problem is that the aggregation sub-model only has 10 size classes of particles and so the structure of the flux may not be correct. Flux depends upon surface production.

The physical and biochemical sub-models seem adequate in simulating the interaction of the stratification, nutrients and phytoplankton with melting ice. Much work can be done in tuning the biology such as the phytoplankton productivity vs. intensity of light curves and characteristics of nutrient uptake—"small" vs. "large" phytoplankton, zooplankton grazing, etc. In the aggregation process, "stickiness" is important. In all of the experiments outlined here, we have not varied any of these parameters.

As regards the "50" series of experiments: What is right and what is wrong with the model/results of the coastal upwelling? Again, the ice sub-model seems reasonable. The drag between wind and ice, and between ice and water is about twice that between wind and water. This means that water is more strongly driven, with movable ice as an intermediary. In the model, these relationships are modified by how much ice cover there is at individual grid points as outlined in Methods above. A possible problem here is that the ice sub-model makes little provision for ice–ice interaction (i.e., no friction). However, this seems not to have been a problem here as ice is not pushed against itself or the coast. In other words, friction does not come into play as long as the wind, hence ice, is not convergent. A provision was added to keep the ice from building, or rafting, too much if the ice transport is convergent.

The physical and biochemical models seemed adequate. Classical coastal upwelling occurred with associated vertical and horizontal currents and fluxes. One problem here was that the coast was modeled as a vertical wall with the bottom at 300 m. The only record of coastal upwelling occurring on the north

coast of Alaska was observed by Johnson [1989] and was in water ~40 m deep. The Johnson [1989] report does not provide very much data for initial and boundary conditions or for verification.

The third objective was to model the convective sinking of water, both in conjunction with, and as a separate process from the flux of natural/primary production particles and particle aggregation. Studies [e.g., Cavalieri and Martin 1994] suggest that brine rejection over the Arctic Ocean shelf is the source of the cold, salty water that maintains the Arctic Ocean halocline via convective sinking. Probably most of the time this involves low speed (also known as convective mixed layer deepening, ~meters per day) convection rather than advective or penetrative convection with speeds ~10s to 1000s m d^{-1}. (Note that while 1000s m d^{-1} seems like a very high velocity for vertical flow in the ocean, and it is, penetrative velocities of up to 8 cm s^{-1} [8 cm s^{-1} translates to almost 7000 m d^{-1}] have been observed [e.g., Denbo and Skyllingstad 1996]). However, Drijfhout et al. [1996] suggest that in this region off Alaska, at least one event per year occurs where a penetrative column caused by surface cooling reaches at least 200 m. These events are probably penetrative convection.

What is right and what is wrong with the model/results as regards the "convection" experiments? Again, the ice sub-model seems reasonable in that the winds cleared out the ice in a realistic manner. Then, setting a realistic heat flux out of the ocean caused a change of state of water to ice, rejecting brine which lead to convection. The thickening of the ice slowed the heat loss to the point that convection ceased. The physics sub-model seemed reasonable as far as the experiments went—the simulation of preconditioning the water by opening ice and then cooling the open water until ice formed, rejecting salt leading to convection. However, the model was not able to simulate convection with the original initial conditions of temperature and salinity in Figure 3. It was not until the water was made isothermal and isohaline that convection occurred. It does appear that the horizontal grid spacing here (3 km) may be too big to correctly model convection in the sense that in the Greenland Sea the convection cells have dimensions in the order of meters to a kilometer. Other convection models have grid spacing of order 10s of meters [e.g., Kampf and Backhaus 1998]. Clearly, more work is needed here.

For the biochemical sub-model, the phytoplankton was primarily a tracer. While calculations were made on vertical flux of chlorophyll and carbon, the original concentration of material at the surface to be caught up in the convection depends on the prior history of the surface waters. With the model, this can be set or driven to whatever level desired. The important comparison is then between biologically identical experiments. Given all of this, we found that including pressure in the equation of state increased flux by about 2 times.

Again, the biggest problem in all of this is a lack of data to verify results, either how much carbon or chlorophyll was being carried alone, or how much brine was actually being convected downward. Some help as regards the vertical transport of brine is available from Cavalieri and Martin [1994], who estimate that dense water production off the Chukchi\Alaska coast ranges from 0.006 to 0.119 Sv (1 Sv = 10^6 m^3 s^{-1}, and for a scale, the mass transport of the Mississippi River is ~0.018 Sv). But we still do not really know what form this vertical flux or vertical transport takes or what the convective speed is. Weingartner et al. [1998] estimate a horizontal transport of salty brine across the shallow Chukchi shelf at ~0.25 Sv although this is probably due to brine production in both the Bering Sea and the southern Chukchi. For comparison to these transports, Aagaard et al. [1981] and Bjork [1989, 1990] suggest that 1–2 Sv of Arctic shelf water brine of salinity 34.75 psu are required to maintain the halocline layer. Calculated rates from actual data for brine from Arctic polynyas [Cavalieri and Martin 1994] are

estimated at ~0.9 Sv with a range of 0.7–1.2 Sv. Renewal time for the halocline is estimated at 10–40 years [Aagaard et al. 1981; Wallace et al. 1987]. On a somewhat different point, the net horizontal transport through the Bering Strait, from south toward north, is ~2 Sv. However, recent estimates of the net flow are ~0.7 Sv [T. Weingartner, pers. comm.], suggesting significant interannual variability.

To further address the comparison of sinking and convection, Figure 33 shows the time series of chlorophyll moving through the water column from experiments 20, 50, 74 and 79. In 20, the flux is entirely gravitational sinking of particles with no water motion. However, there is very little chlorophyll at all (note that the chlorophyll scale is ~$1/5$ to $1/10$ of the other scales) so a relatively small amout of the material ends up on the bottom over the 28 days. In 50, the winds and upwelling clear the ice and the surface bloom accelerates, resulting in aggregation and much more material accumulating on the bottom. In 50 the flux is also entirely gravitational sinking of particles except during the upwelling. In contrast, in both 74 and 79 the main event is flux driven by vertical convection that is far faster but shorter lived than aggregate sinking. These convective events are concentrated in day 6 (Fig. 33). In both of these cases, 74 and 79, more material gets to the bottom faster. Though, in a sense, how much material gets to the bottom in each of these cases is not a fair comparison. Obviously advection of the material through the water at 100–300 m d^{-1} will get material to the bottom faster than gravitational sinking at 5 m d^{-1}. However, the amount of material advected can easily be varied by adjusting the amount of material caught up in the convection; a convection event in the middle of a spring bloom will transport much more production and carbon than an event in winter.

Our fourth objective was to interact with field/data groups and individuals who are working on different aspects of the Alaska Arctic shelves, as recommended by the National Academy of Science. Real data are required for initial and boundary conditions as well as for verification. The point here is for modelers to interact with field and data processing groups so that the modeling is grounded in reality. But there is not enough money and support to study every aspect of the whole region in detail so that models must be used to fill these needs. We are using available data and interacting with field researchers such as Dr. Tom Weingartner of the University of Alaska and Dr. Walker O. Smith, Jr. of the University of Tennessee. This is ongoing.

The comparison of the model output and the field data outlined above in the Results was, at times, quite good, suggesting that the model that was used for this research appears to have reasonably portrayed some of the complex physical and biological mesoscale processes and their interaction in Arctic waters. The modeling appears to have allowed a better understanding of the coastal and shelf marine environment of these high-latitude, ice-impacted seas. What is most lacking are field data to verify, for example, the ice edge blooms in spring, effects of wind-driven upwelling, and the strong convective flux of mass and material.

Study Products

Niebauer, H.J. 1997. Physical–biological numerical modeling on Alaskan Arctic shelves. Presentation at CMI Annual Research Review, February 1997, University of Alaska Fairbanks.

Niebauer, H.J. 1998. Physical–biological numerical modeling on Alaskan Arctic shelves, p. 27–38. *In* University of Alaska Coastal Marine Institute Annual Report No. 4.

Niebauer, H.J. 2000. Physical–biological numerical modeling on Alaskan Arctic shelves. Final report, University of Alaska Coastal Marine Institute. 84 p.

References

Aagaard, K., L.K. Coachman, and E. Carmack. 1981. On the halocline of the Arctic Ocean. Deep-Sea Res. 28:529–545.

Aagaard, K., C.H. Pease and S.A. Salo. 1988. Beaufort Sea mesoscale circulation study—Preliminary results. NOAA Technical Memorandum ERL PMEL-82, 171 p.

Alexander, V., and H.J. Niebauer. 1981. Oceanography of the eastern Bering Sea ice edge zone in spring. Limnol. Oceanogr. 26:1111–1125.

Alldredge, A.L. and P. McGillivary. 1991. The attachment probabilities of marine snow and their implications for particle coagulation in the ocean. Deep-Sea Res. 38:431–443.

Bennett, J.R. 1974. On the dynamics of wind-driven lake currents. J. Phys. Oceanogr. 4:400–414.

Bjork, G. 1989. A one-dimensional time-dependent model for the vertical stratification of the upper Arctic Ocean. J. Phys. Oceanogr. 19:52–67.

Bjork, G. 1990. The vertical distribution of nutrients and oxygen 18 in the upper Arctic Ocean. J. Geophys. Res. 95:16025–16036.

Cavalieri D.J. and S. Martin. 1994. The contribution of Alaskan, Siberian, and Canadian coastal polynyas to the cold halocline layer of the Arctic Ocean. J. Geophys. Res. 99:18343–18362.

Conway, H.L. 1977. Interactions of inorganic nitrogen in the uptake and assimilation of marine phytoplankton. Mar. Biol. 39:221–232.

Cota, G.F., L.R. Pomeroy, W.G. Harrison, E.P. Jones, F. Peters, W.M. Shelton, Jr., T.J. Weingartner. 1996. Nutrients, primary production and microbial heterotrophy in the southeastern Chukchi Sea: Arctic summer nutrient depletion and heterotrophy. Mar. Ecol. Prog. Ser. 135:247–258.

Coyle, K.O. and R.T. Cooney. 1988. Trophic implications of cross-shelf copepod distributions in the southeastern Bering Sea. Mar. Biol. 70:187–196.

Denbo, D.W. and E.D. Skyllingstad. 1996. An ocean large-eddy simulation model with application to deep convection in the Greenland Sea. J. Geophys. Res. 101:1095–1110.

Doronin, Y.P. and D.E. Kheisin. 1977. Sea Ice. Amerind, New Delhi, 323 p.

Drijfhout, S.S., E. Maier-Reimer and U. Mikolajewicz. 1996. Tracing the conveyor belt in the Hamburg large-scale geostrophic ocean general circulation model. J. Geophys. Res. 101:22563–22575.

Dugdale, R.C. and J.J. Goering. 1967. Uptake of new and regenerated forms of nitrogen in primary productivity. Limnol. Oceanogr. 12:196–206.

Eppley, R.W. 1972. Temperature and phytoplankton growth in the sea. Fish. Bull. 72:1063–1085.

Feldman, U., P.J. Howarth and J.A. Davies. 1979. Estimating the surface wind speed over drifting pack ice from surface weather charts. Boundary-Layer Meteorol. 16:421–429.

Gardner, W.D. 1997. The flux of particles to the deep sea: Methods, measurements, and mechanisms. Oceanography. 10:116–121.

Grebmeier, J.M. and L.W. Cooper. 1995. Influence of the St. Lawrence Island Polynya upon the Bering Sea benthos. J. Geophys. Res. 100:4439–4460.

Hamilton, P. and M. Rattray, Jr. 1978. A numerical model of the depth-dependent, wind-driven circulation on a continental shelf. J. Phys. Oceanogr. 8:437–457.

Harrison, W.G. and T. Platt. 1985. Photosynthesis–irradiance relationships in polar and temperate phytoplankton populations. Polar Biol. 5:153–164.

Hewes, C.D., O. Holm-Hansen and E. Sakshaug. 1985. Alternate carbon pathways at lower trophic levels in the Antarctic food web, pp. 277–283. *In* W.R. Siegfried, P.R. Condy and R.M. Laws [eds.], Antarctic Nutrient Cycles and Food Webs. Springer-Verlag, New York.

Hibler, W.D., III. 1979. A dynamic thermodynamic sea ice model. J. Phys. Oceanogr. 9:815–846.

Hill, P. 1992. Reconciling aggregation theory with observed vertical fluxes following phytoplankton blooms. J. Geophys. Res. 97:2295–2308.

Jackson, G.A. 1990. A model of the formation of marine algal flocs by physical coagulation processes. Deep-Sea Res. 37:1197–1211.

Jamart, B.M., D.F. Winter, K. Banse, G.C. Anderson and R.K. Lam. 1977. A theoretical study of phytoplankton growth and nutrient distribution in the Pacific Ocean off the northeastern U.S. coast. Deep-Sea Res. 24:753–773.

Jerlov, N. 1968. Optical Oceanography. Elsevier, New York, 199 p.

Johnson, W.R. 1989. Current response to wind in the Chukchi Sea: A regional coastal upwelling event. J. Geophys. Res. 94:2057–2064.

Kampf, J. and J.O. Backhaus. 1998. Shallow, brine-driven free convection in polar oceans: Non-hydrostatic numerical process studies. J. Geophys. Res. 103:5577–5593.

Kiorboe, T., C. Lundsgaard, M. Olsen and J.L.S. Hansen. 1990. Aggregation and sedimentation processes during a spring phytoplankton bloom: A field experiment to test coagulation theory. J. Mar. Res. 52:297–323.

Kremer, J.N. and S.W. Nixon. 1978. A Coastal Marine Ecosystem. Springer-Verlag, New York, 217 p.

Maykut, G.A. and T.C. Grenfell. 1975. The spectral distribution of light beneath first-year sea ice in the Arctic Ocean. Limnol. Oceanogr. 20:554–563.

McCave, I.N. 1975. Vertical flux of particles in the ocean. Deep-Sea Res. 22:491–502.

McPhee, M.C. 1980. An analysis of pack ice drift in summer, p.62–75. In R.S. Pritchard [ed.], Sea Ice Processes and Models. Univ. Washington Press, Seattle.

Millero, F.J., C.-T. Chen, A. Bradshaw and K. Schleicher. 1980. A new high-pressure equation of state for seawater. Deep-Sea Res. 27A:255–264.

Millero, F.J. and A. Poisson. 1981. International one-atmosphere equation of state of seawater. Deep-Sea Res. 28A:625–629.

Müller-Karger, F. and V. Alexander. 1987. Nitrogen dynamics in a marginal sea-ice zone. Cont. Shelf Res. 7:805–623.

Munk, W.H. and E.R. Anderson. 1948. Notes on a theory of the thermocline. J. Mar. Res. 7:276–295.

Niebauer, H.J. 1982. Wind and melt driven circulation in a marginal sea ice edge frontal system: A numerical model. Cont. Shelf Res. 1:49–98.

Niebauer, H.J. 1991. Bio-physical interactions at the edge of the Arctic ice pack. J. Mar. Syst. 2:209–232.

Niebauer, H.J. and V. Alexander. 1985. Oceanographic frontal structure and biological production at an ice edge. Cont. Shelf Res. 4:367–388.

Niebauer, H.J., V. Alexander, and S. Henrichs. 1990. Physical and biological oceanographic interaction in the spring bloom at the Bering Sea marginal ice zone. J. Geophys. Res. 95:22229– 22241.

Niebauer, H.J., V. Alexander and S. Henrichs. 1995. A time-series study of the spring bloom at the Bering Sea ice edge, I. Physical processes, chlorophyll and nutrient chemistry. Cont Shelf Res. 15:1859–1877.

Niebauer, H.J. and W.O. Smith, Jr. 1989. A mesoscale model of the physical–biological interactions in the Fram Strait marginal ice zone. J. Geophys. Res. 94:16151–16175.

Overland, J.E. 1985. Atmospheric boundary layer structure and drag coefficients over sea ice. J. Geophys. Res. 90:9029–9049.

Pease, C.H. and J.E. Overland. 1984. An atmospherically driven sea-ice drift model for the Bering Sea. Ann. Glaciol. 5:111–114.

Petipa, T.S. 1966. Relationship between growth, energy, metabolism and ratio in *A. clausi*, p. 82–91. *In* Physiology of Marine Animals. Oceanographical Commission, USSR Academy of Science, Moscow.

Platt, T., C.L. Gallegos and W.G. Harrison. 1980. Photoinhibition of photosynthesis in natural assemblages of marine phytoplankton. J. Mar. Res. 38:687–701.

Pomeroy, L.R. 1997. Primary production in the Arctic Ocean estimated from dissolved oxygen. J. Mar. Syst. 10:1–8.

Riebesell, U. and D.A. Wolf-Gladrow. 1992. The relationship between physical aggregation of phytoplankton and particle flux: A numerical model. Deep-Sea Res. 39:1085–1102.

Riley, G.A. 1956. Oceanography of Long Island Sound, 1952–1954, IX. Production and utilization of organic matter. Bull. Bingham Oceanogr. Collect. 15:324–343.

Semtner, A.J., Jr. 1976. A model for the thermodynamic growth of sea ice in numerical investigations of climate. J. Phys. Oceanogr. 6:379–389.

Smith, W.O., Jr. 1987. Phytoplankton dynamics of marginal ice zones. Oceanogr. Mar. Biol. 25:11–38.

Smith, W.O., Jr., M.E. Baumann, D.L. Wilson and L. Aletsee. 1987. Phytoplankton biomass and productivity in the marginal ice zone of the Fram Strait during summer 1984. J. Geophys. Res. 92:6777–6786.

Smith, W.O., Jr. and R.B. Dunbar. 1998. The relationship between new production and vertical flux on the Ross Sea continental shelf. J. Mar. Syst. 17:445–457.

Smith, W.O., Jr. and G. Kattner. 1988. Phytoplankton nitrogen uptake in the Fram Strait marginal ice zone. J. Cons. Int. Explor. Mer. 188:90–97.

Smith, W.O., Jr. and D.M. Nelson. 1985. Phytoplankton bloom produced by a receding ice edge in the Ross Sea: Spatial coherence with the density field. Science. 227:163–166.

Smith, W.O., Jr. and H.J. Niebauer. 1993. Interactions between biological and physical processes in Arctic seas: Investigations using numerical models. Rev. Geophys. 31:189–209.

Smith, W.O., Jr, H.J. Niebauer and V. Asper. 1999. Coupling of surface layer biological processes and vertical flux in the Ross Sea, p. 151–157. *In* F. Faranda, L. Guiglielmo and A. Ianora [eds.], Ross Sea Ecology. Springer, Berlin.

Smith, W.O., Jr. and E. Sakshaug. 1990. Polar phytoplankton, p. 477–526. *In* W.O. Smith, Jr. [ed.], Polar Oceanography; Part B, Chemistry, Biology and Geology. Academic Press, Inc.

Sverdrup, H.U. 1953. On conditions for the vernal blooming of phytoplankton. J. Cons. Explor. Mer, 18:287–295.

Wallace, D.W.R., R.M. Moore and E.P. Jones. 1987. Ventilation of the Arctic Ocean cold halocline: Rates of diapycnal and isopycnal transport, oxygen utilization and primary production inferred using chlorofluoromethane distributions. Deep-Sea Res. 34A:1957–1979.

Walsh, J.J. 1975. A spatial simulation model of the Peru upwelling ecosystem. Deep-Sea Res. 22:201–236.

Walsh, J.J., C.P. McRoy, L.K. Coachman, J.J. Goering, J.J. Nihoul, T.E. Whitledge, T.H. Blackburn, P.L. Parker, C.D. Wirick, P.G. Shuert, J.M. Grebmeier, A.M. Springer, R.B. Tripp, D.A. Hansell, S. Djenidi, E. Deleersnijder, K. Henriksen, B.A. Lund, P. Andersen, F.E. Müller-Karger and K. Dean. 1989. Carbon and nitrogen cycling within the Bering/Chukchi Seas: Source regions for organic matter effecting AOU demands of the Arctic Ocean. Prog. Oceanogr. 22:277–359.

Weingartner, T.J., D.J. Cavalieri, K. Aagaard and Y. Sasaki. 1998. Circulation, dense water formation and outflow on the Northeast Chukchi shelf. J. Geophys. Res. 103:7647–7661.
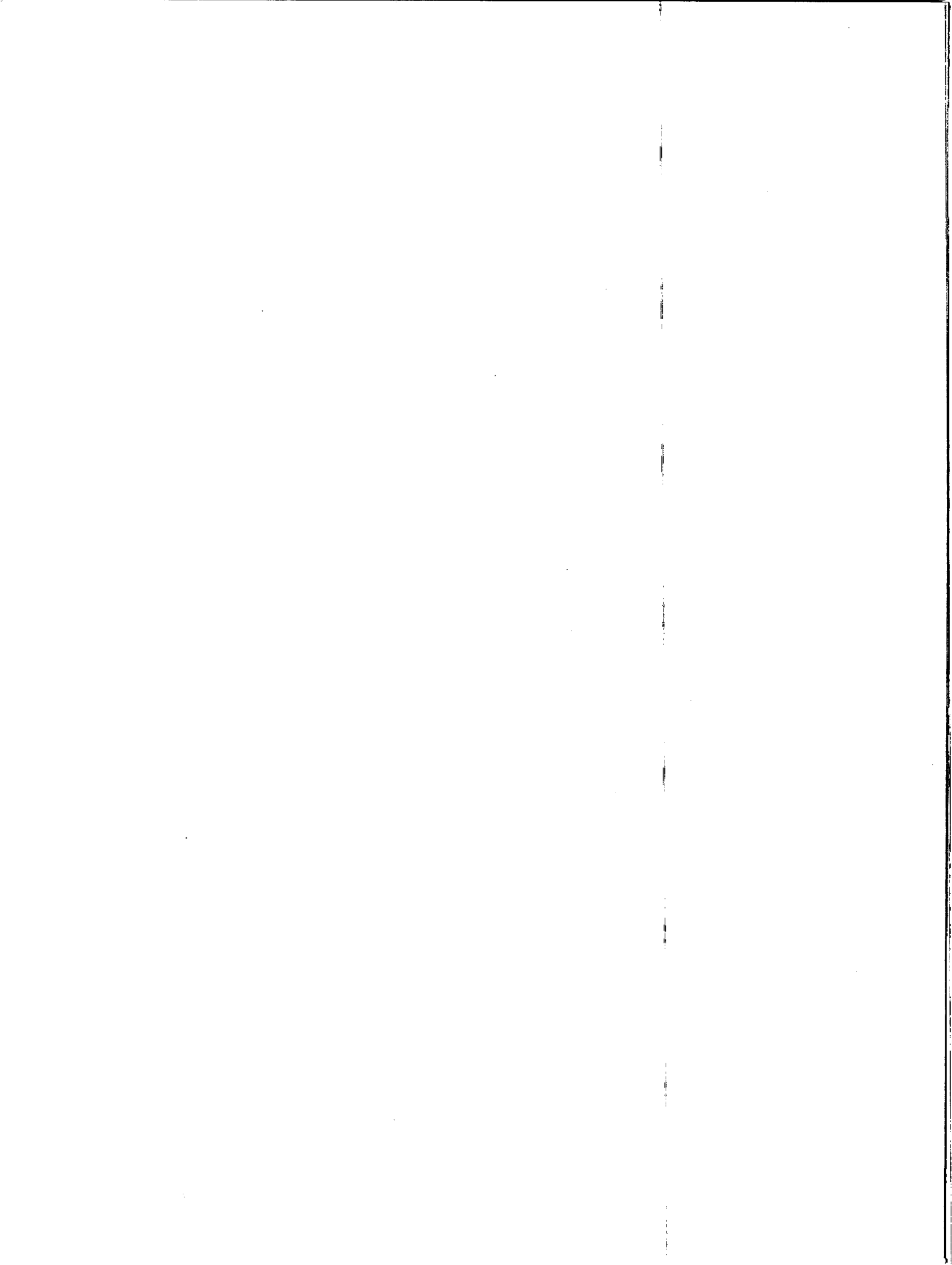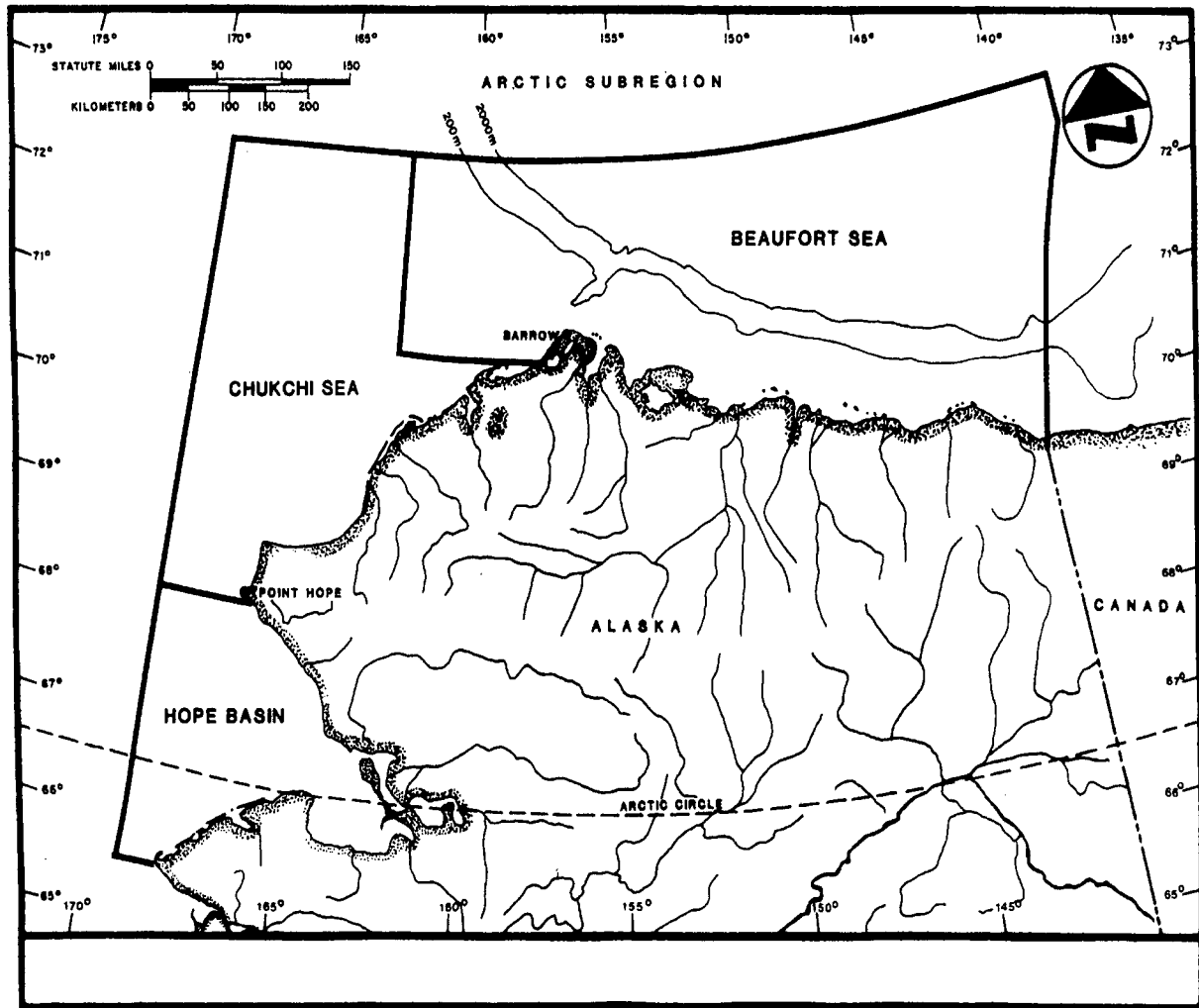
Figure 1. Focus area for "Physical–Biological Numerical Modeling on Alaskan Arctic Shelves", especially in the Chukchi and Beaufort Seas region near the Barrow Canyon.

43
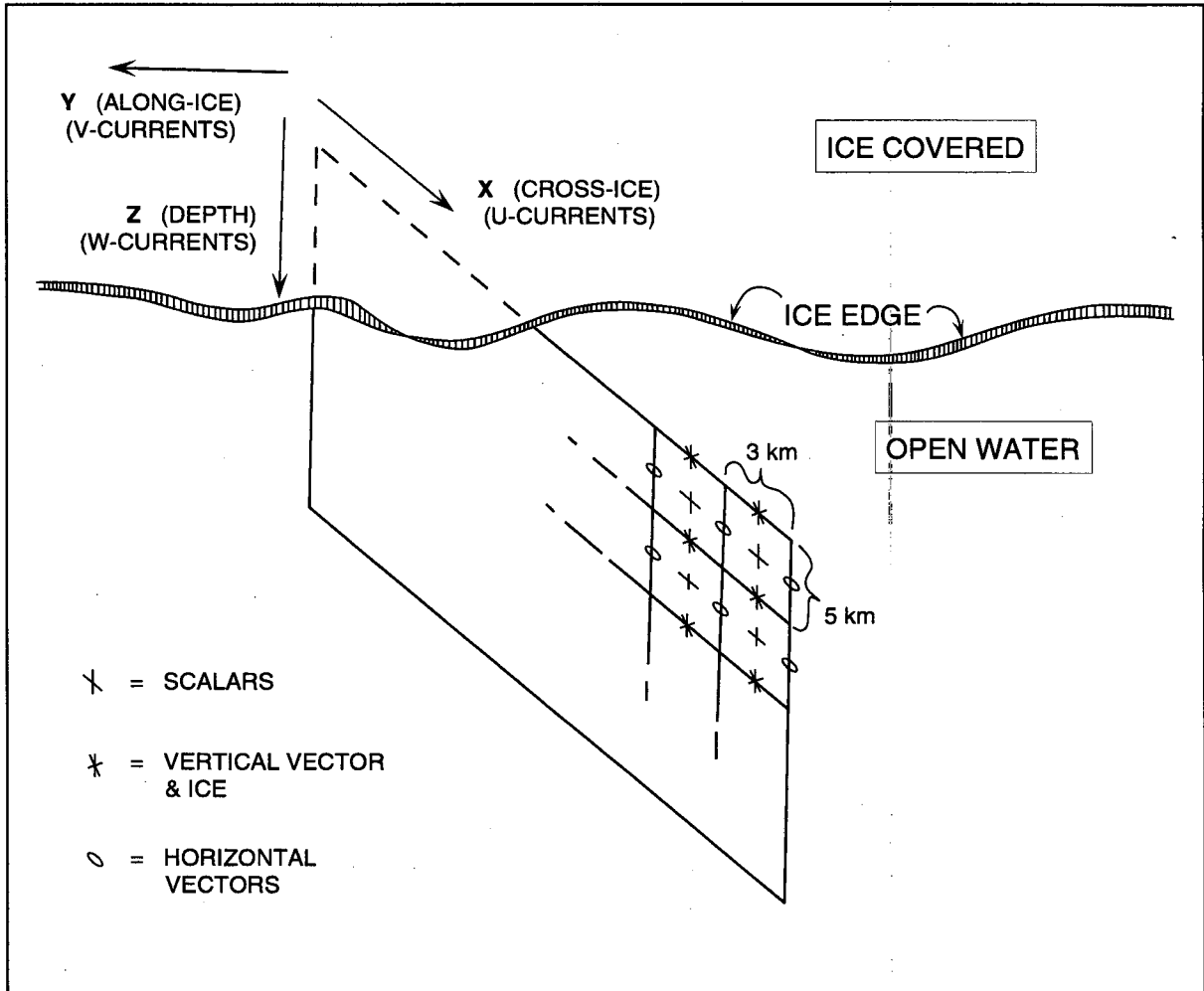
Figure 2. Schematic of the marginal ice zone with the model cross section superimposed. The x, y, and z coordinates and grid points are also shown.
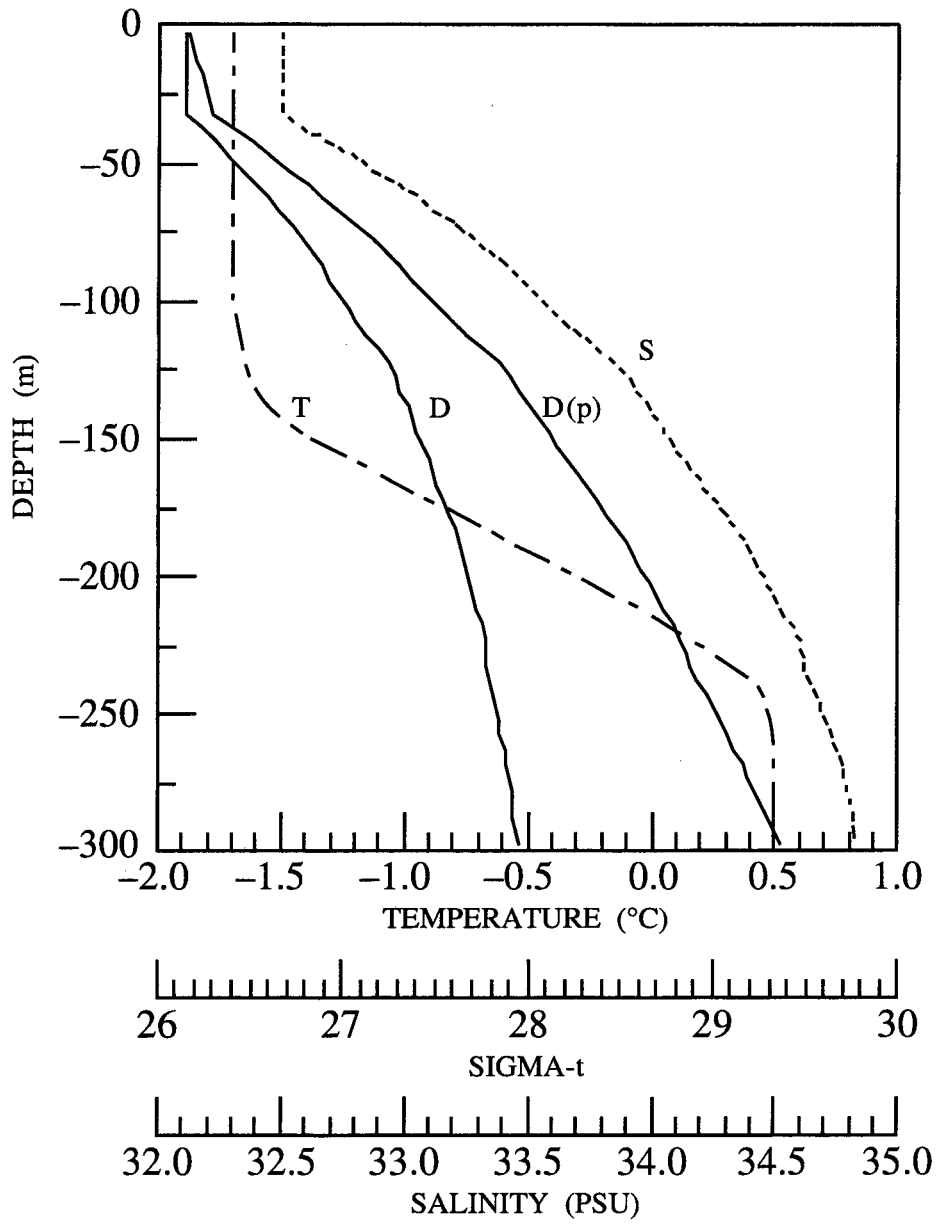
Figure 3. Initial conditions. "D" = density as a function of T and S only.
"D(p)" = density of T, S and pressure.
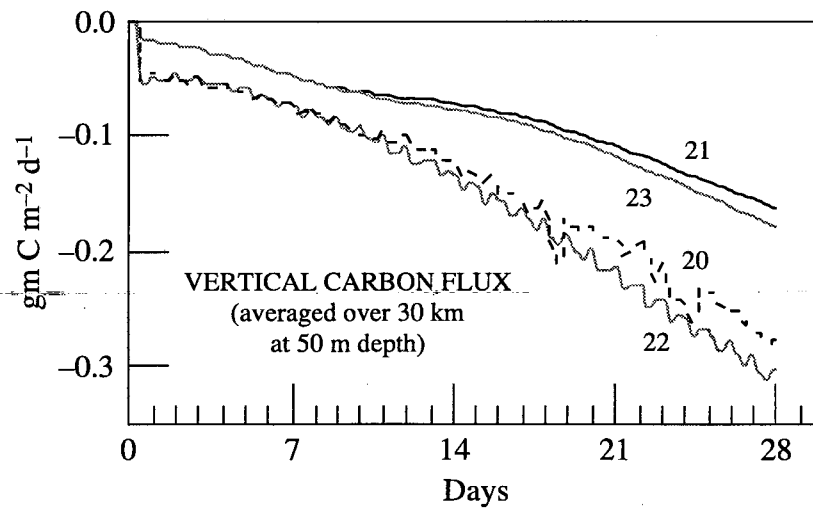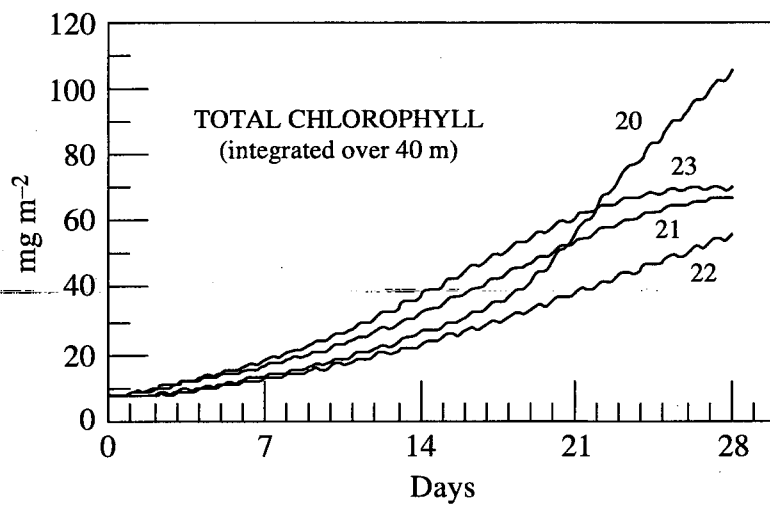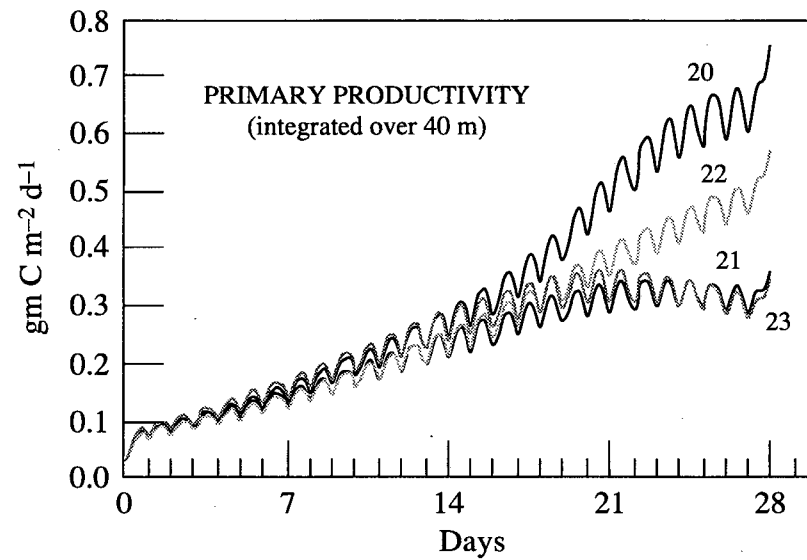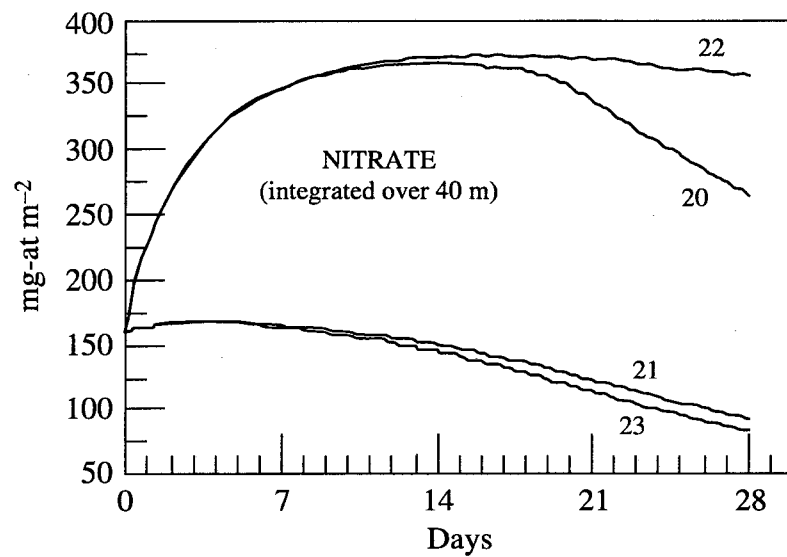
Figure 4. Time series of depth integrated data from the "20" series experiments. Primary productivity is smoothed with a 3-point running mean.
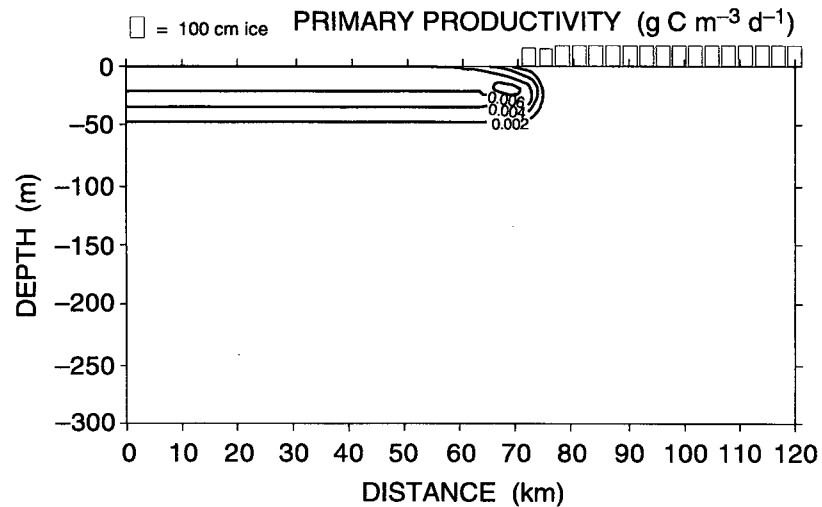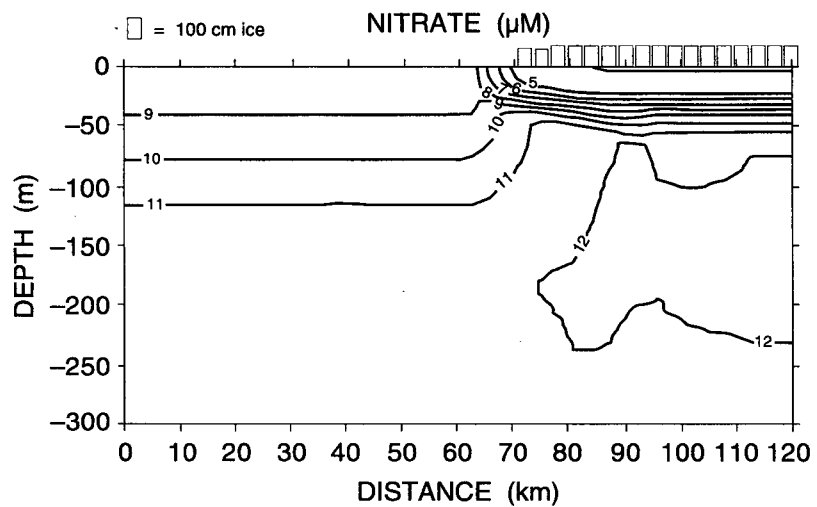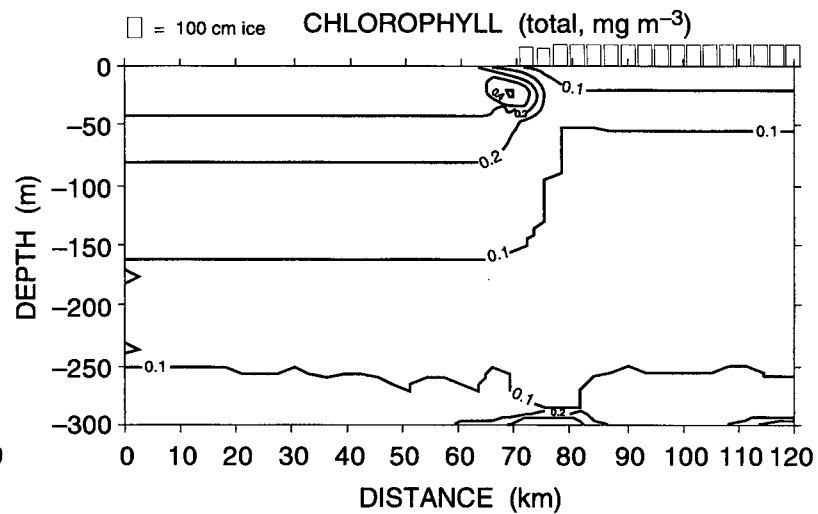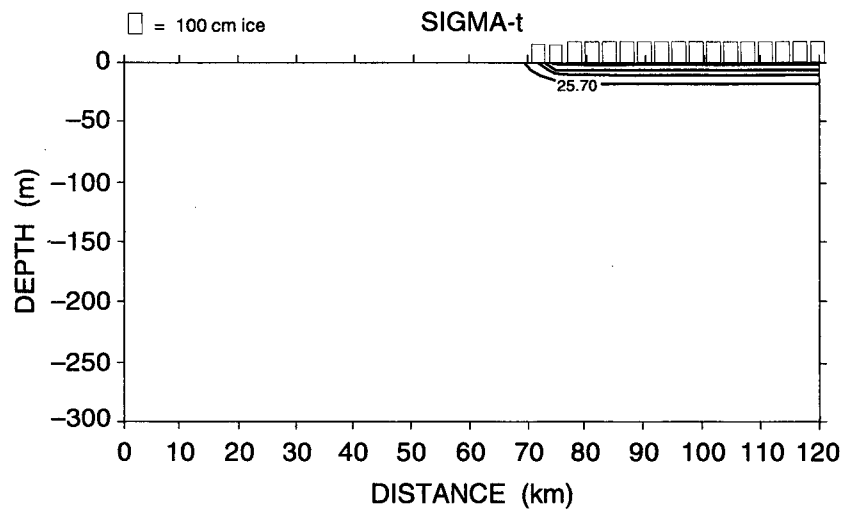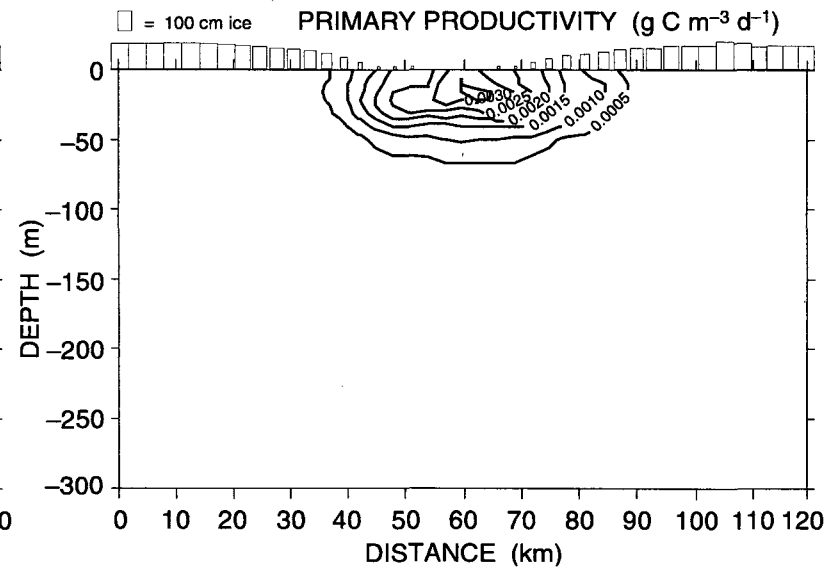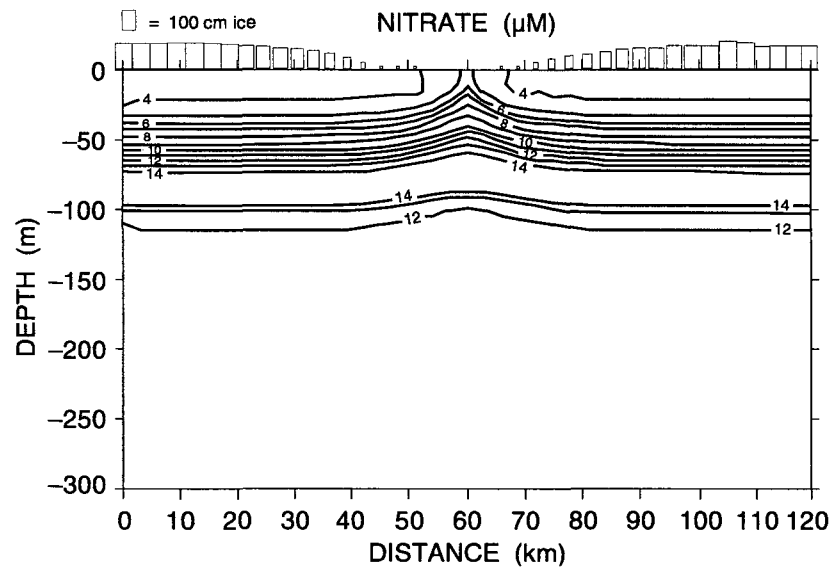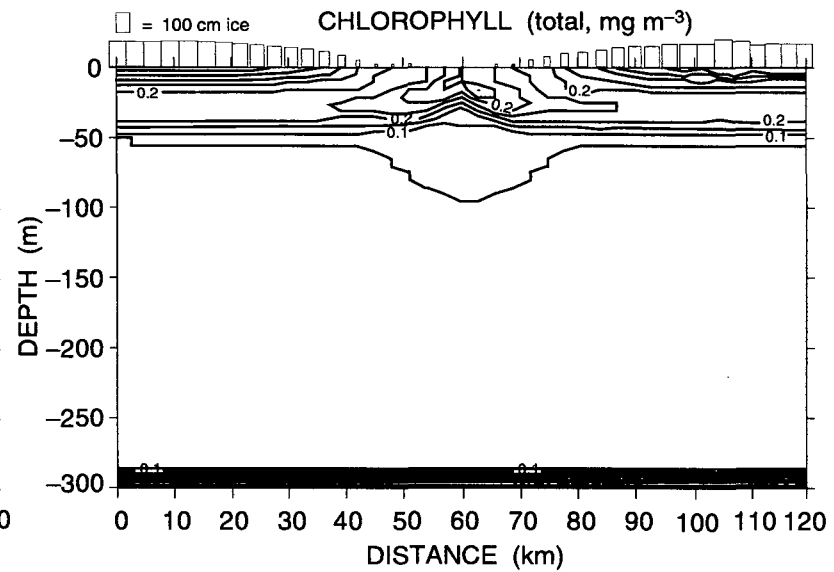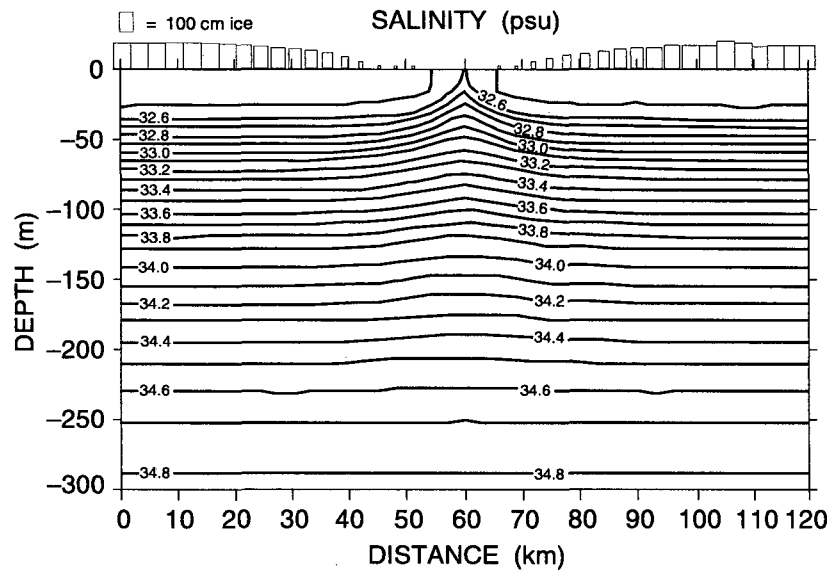
Figure 5. Cross section contours for data from experiment "20" on day 7.

□ = 100 cm ice   CHLOROPHYLL (total, mg m^{-3})

□ = 100 cm ice   NITRATE (μM)

□ = 100 cm ice   CHLOROPHYLL (c10, mg m^{-3})

□ = 100 cm ice   CHLOROPHYLL FLUX (mg m^{-2} d^{-1})
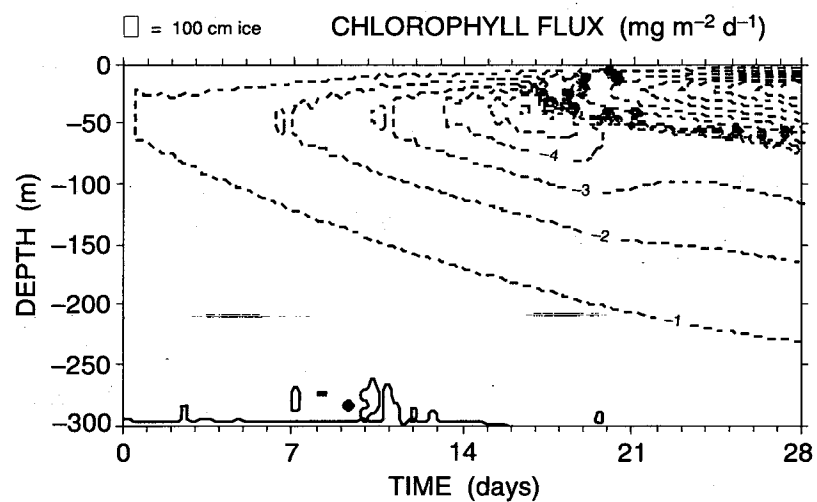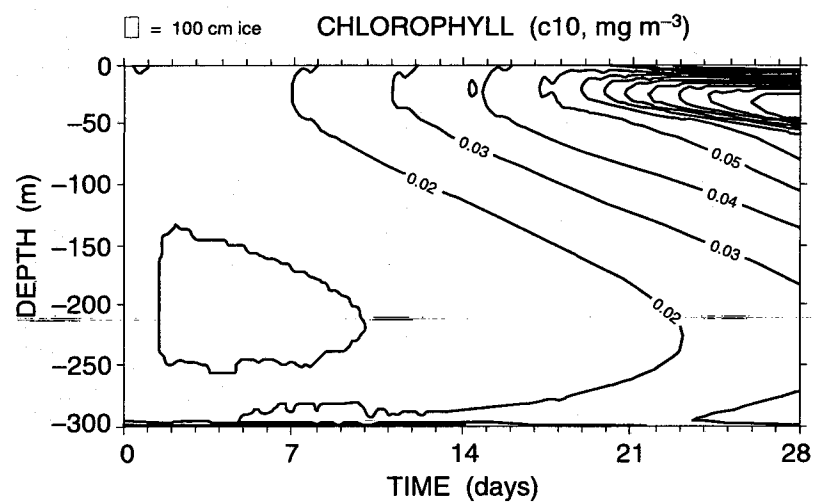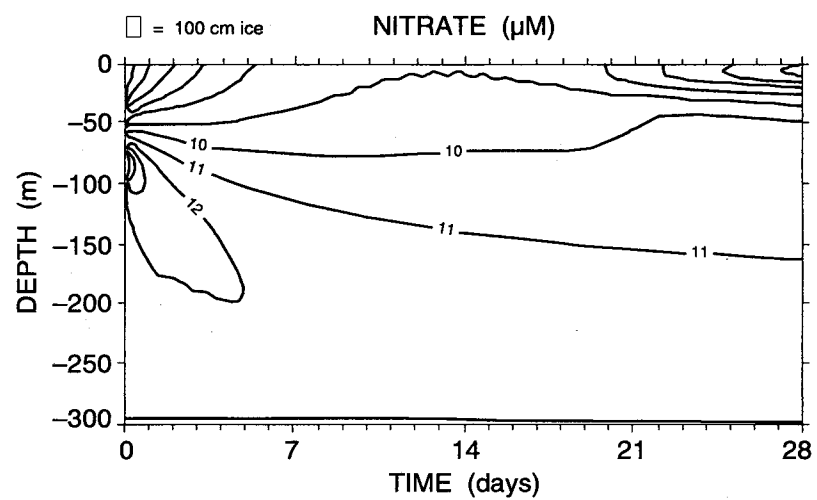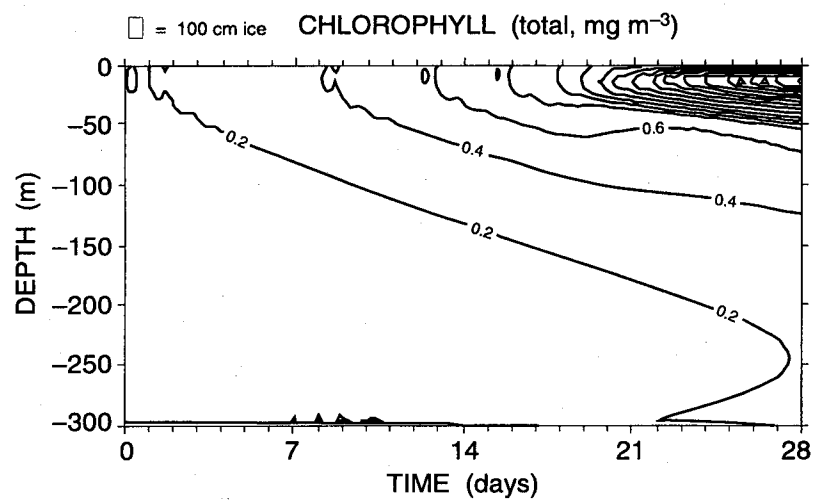
Figure 6.   Time series contours over 28 days of data from experiment "20". Dashed lines are negative.
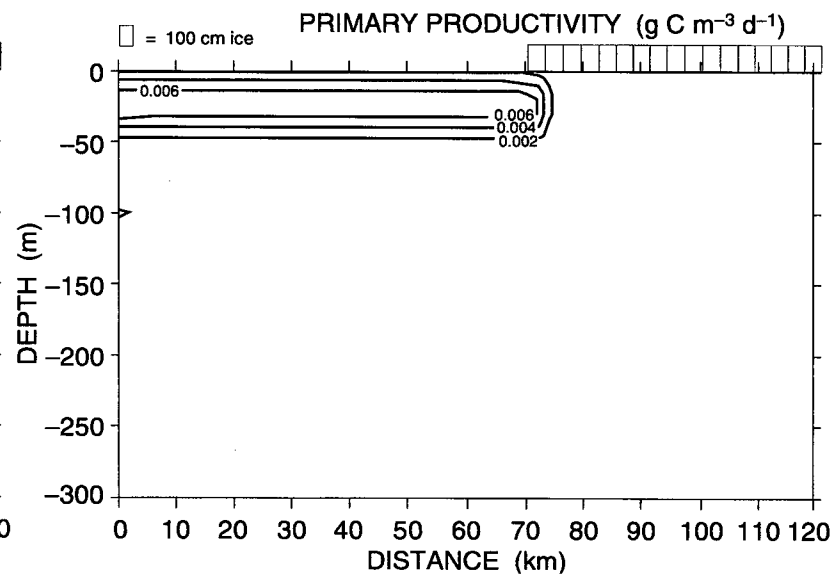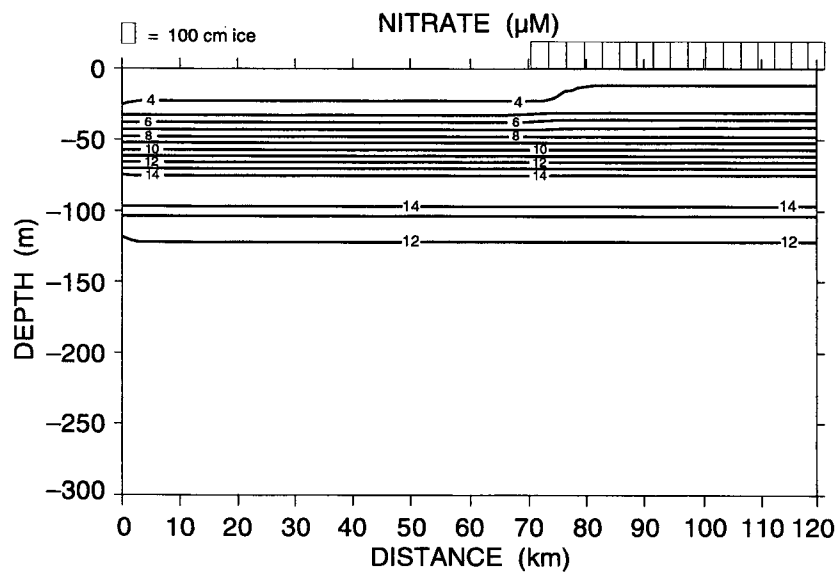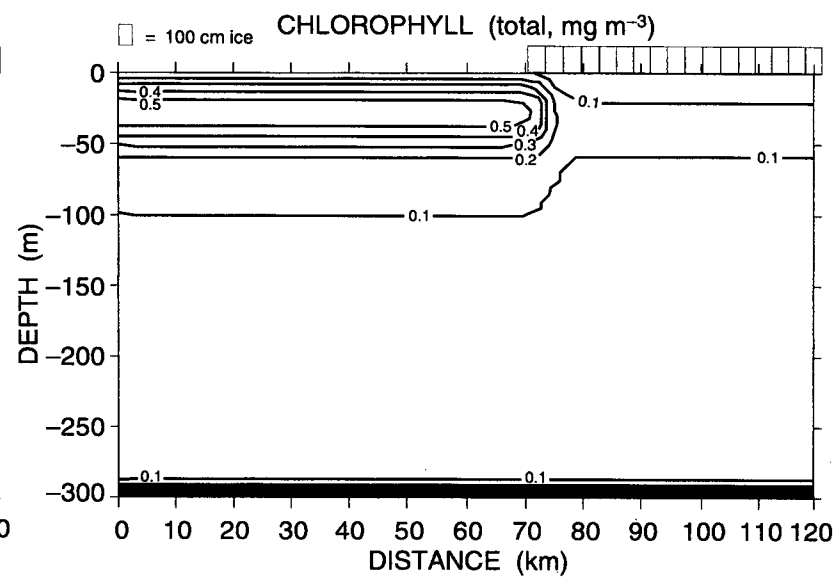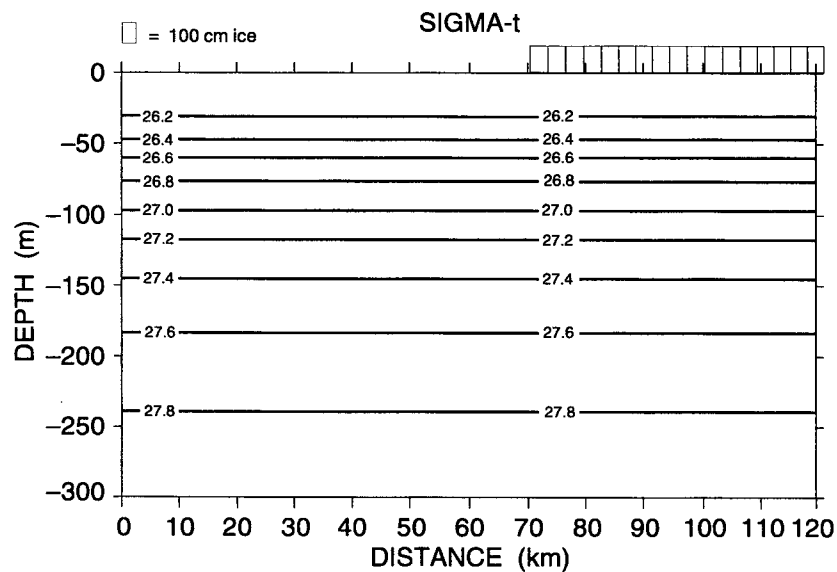
Figure 7. Cross section contours for data from experiment "21" on day 7.

□ = 100 cm ice   CHLOROPHYLL (total, mg m⁻³)

□ = 100 cm ice   NITRATE (μM)

□ = 100 cm ice   CHLOROPHYLL (c10, mg m⁻³)

□ = 100 cm ice   CHLOROPHYLL FLUX (mg m⁻² d⁻¹)
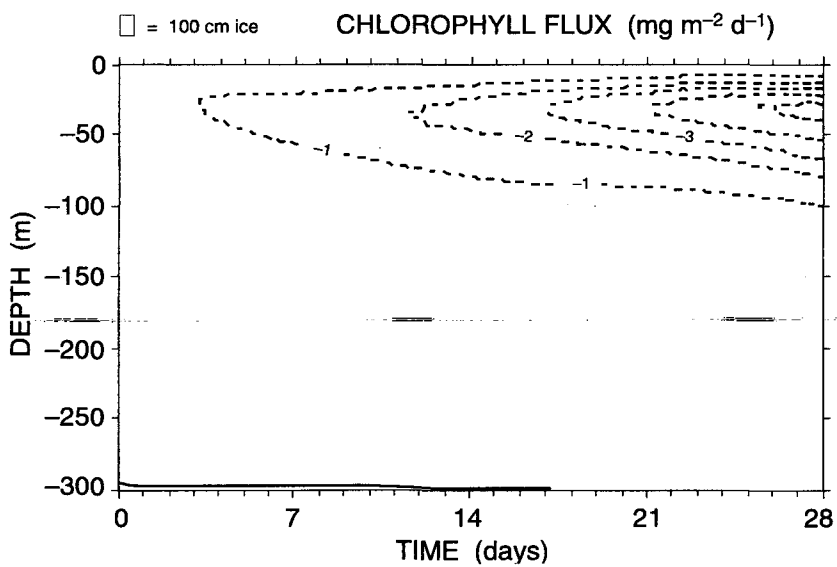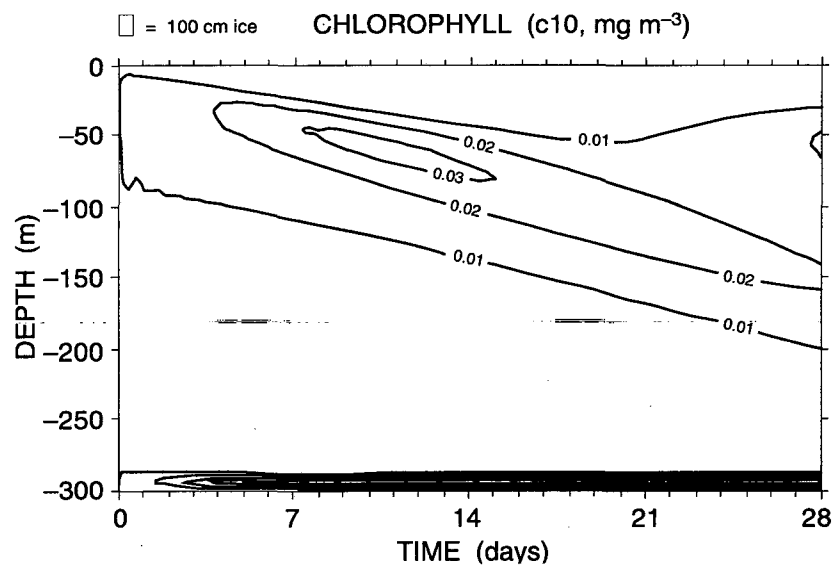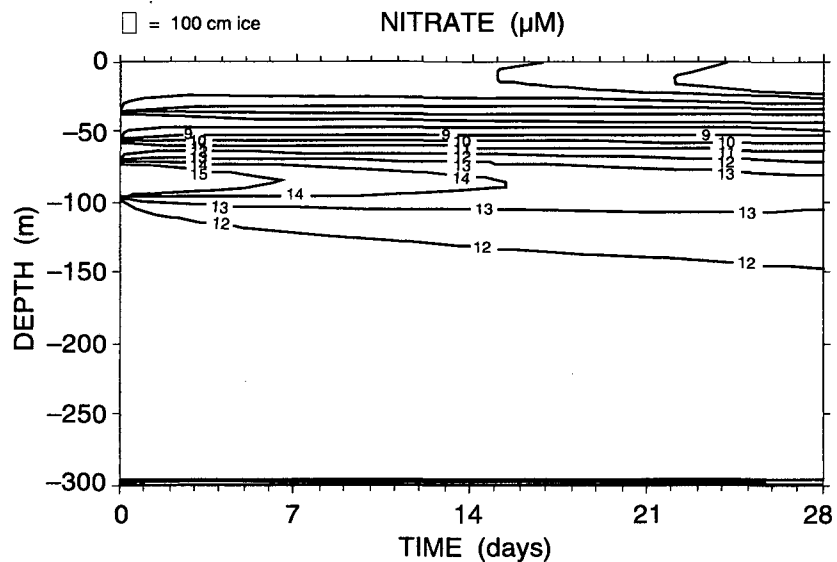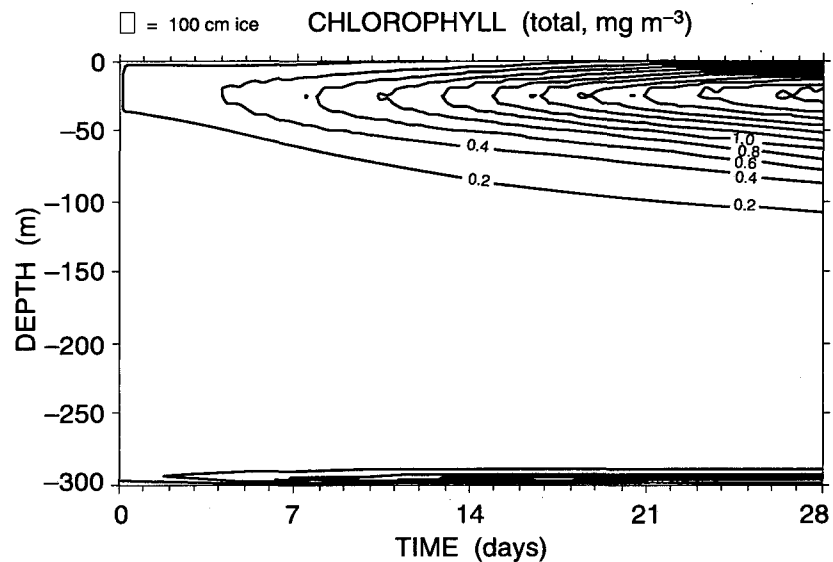
Figure 8. Time series contours over 28 days of data from experiment "21". Dashed lines are negative.

CHLOROPHYLL (total, mg m^{-3})

□ = 100 cm ice

ISOHALINE AND ISOTHERMAL
SO NO SIGMA-t GRADIENTS

51

NITRATE (µM)

□ = 100 cm ice

PRIMARY PRODUCTIVITY (g C m^{-3} d^{-1})

□ = 100 cm ice
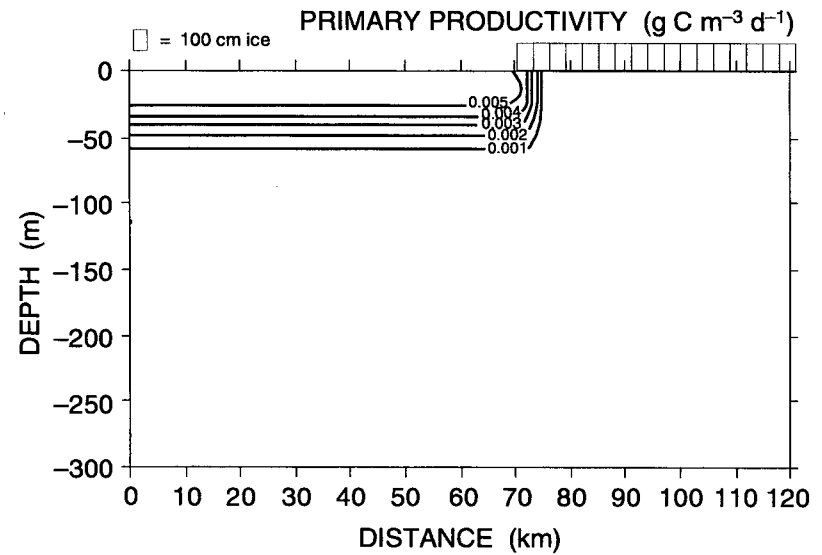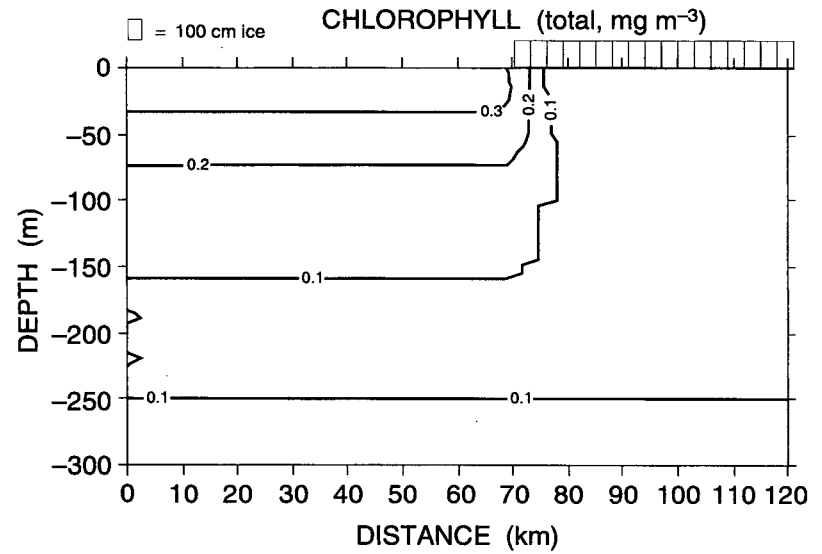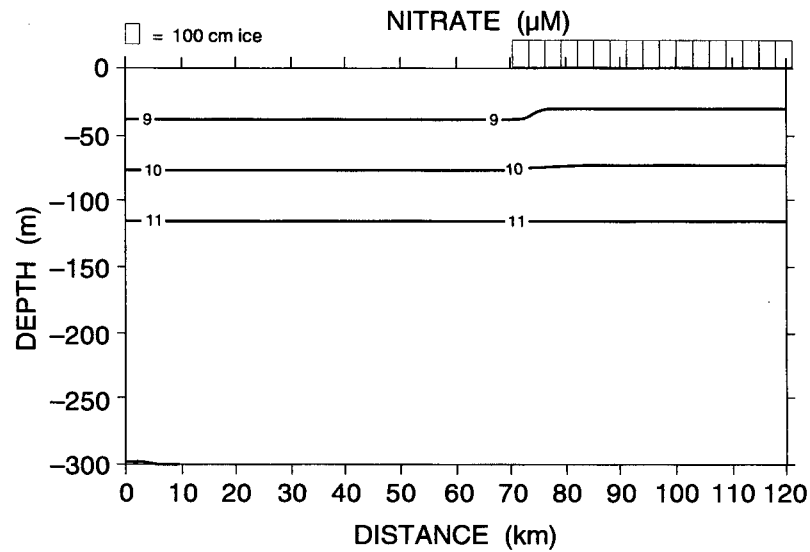
Figure 9. Cross section contours for data from experiment "22" on day 7.
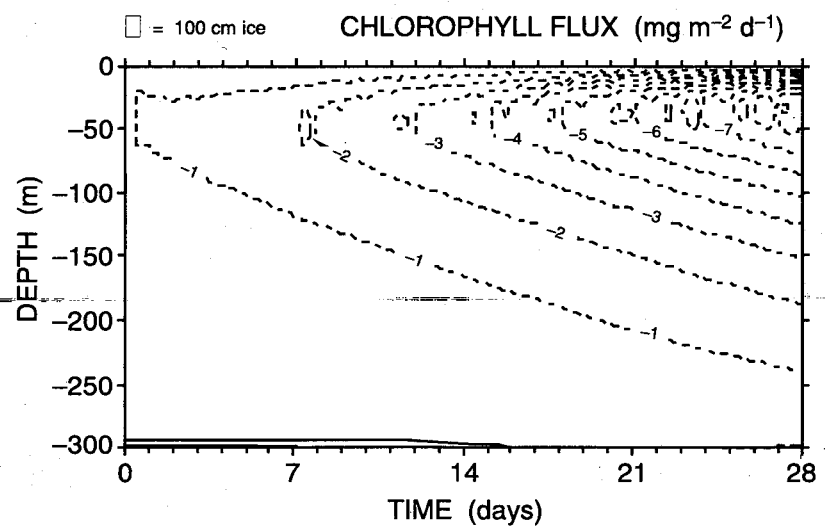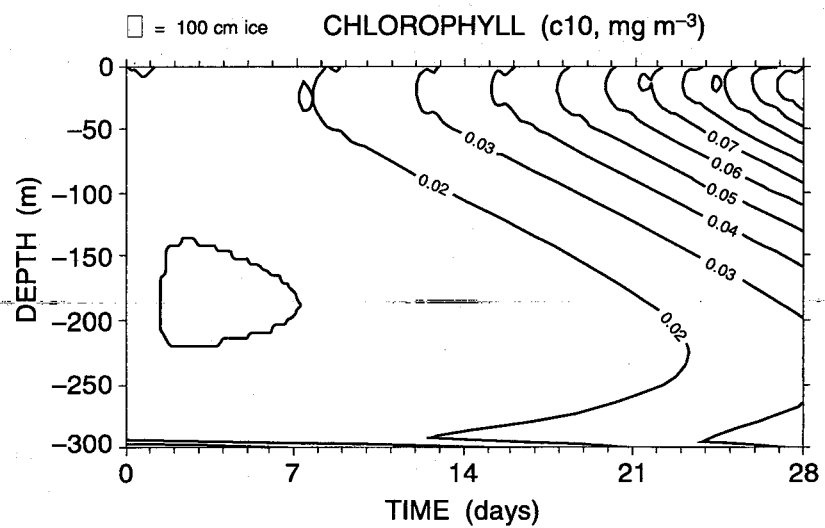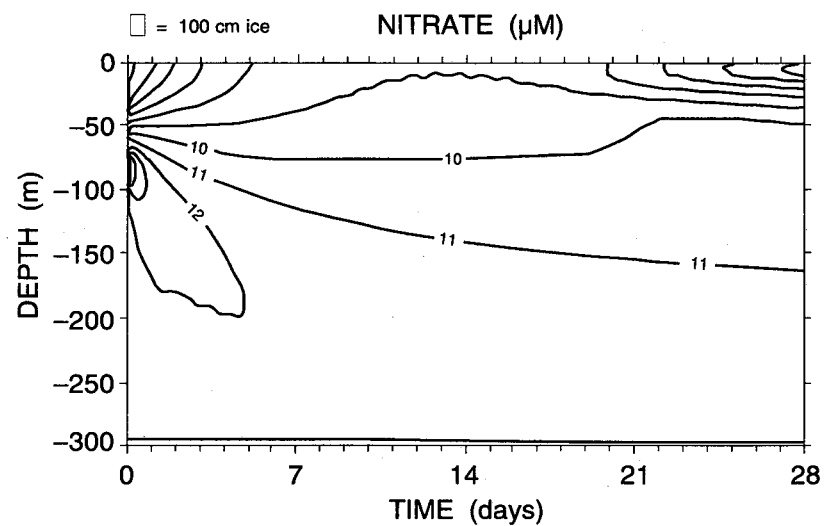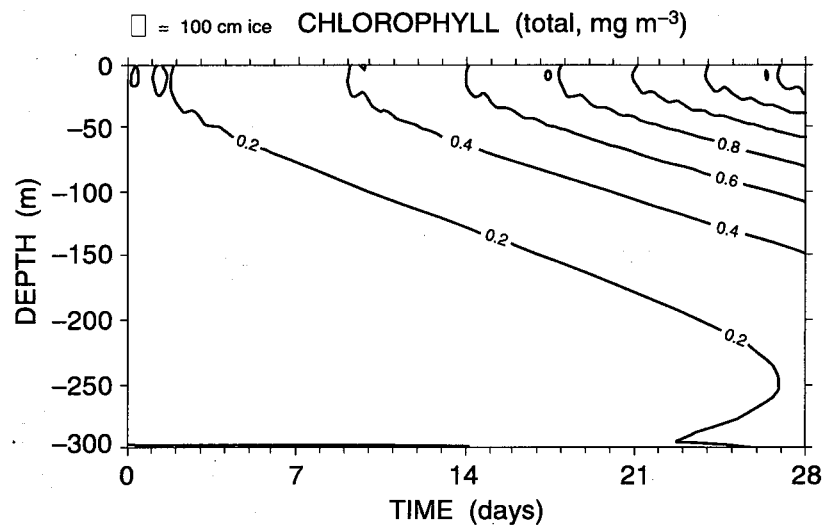
Figure 10. Time series contours over 28 days of data from experiment "22". Dashed lines are negative.
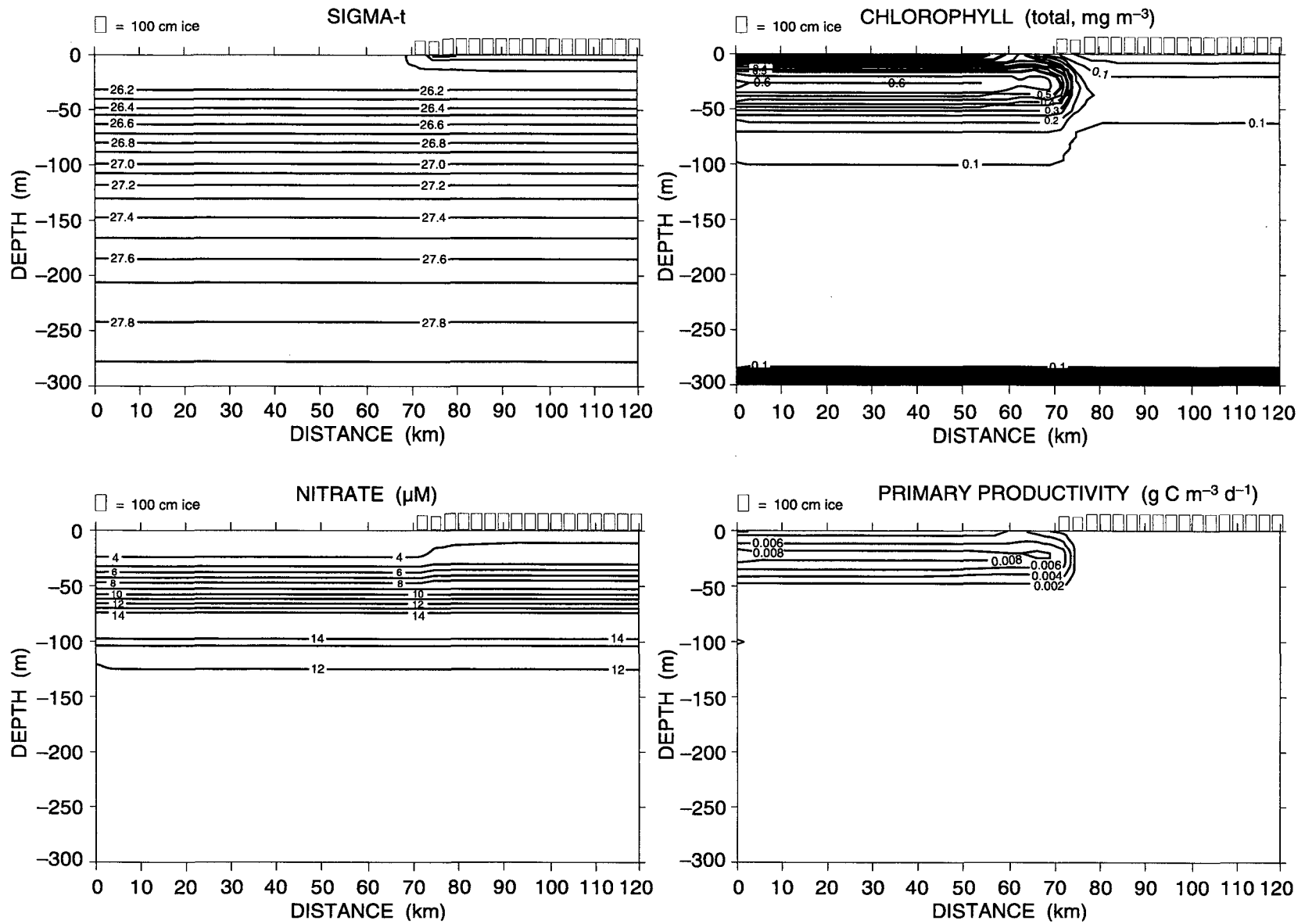
Figure 11. Cross section contours for data from experiment "23" on day 7.
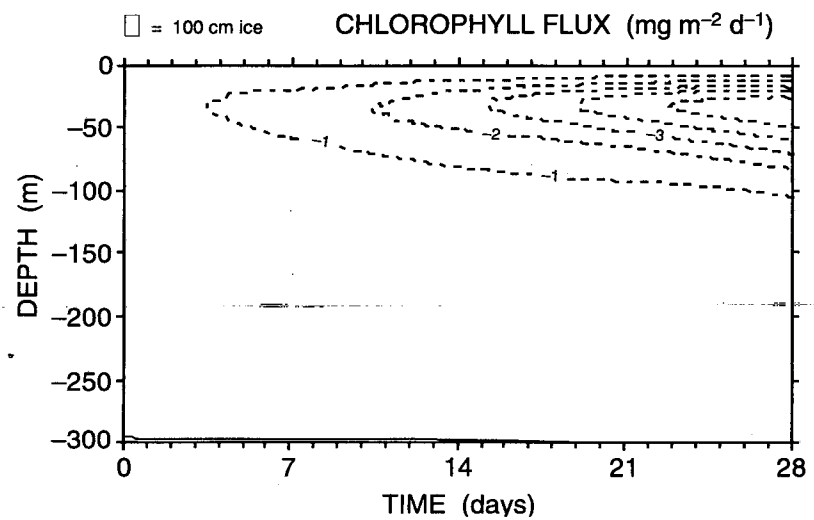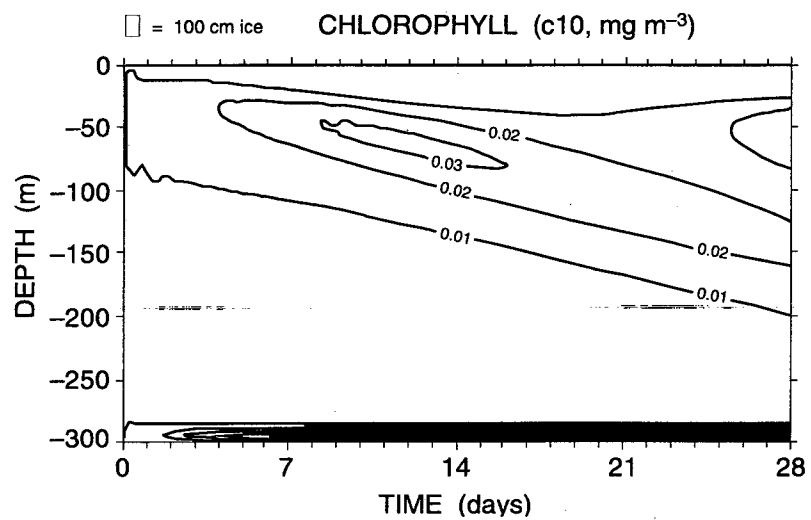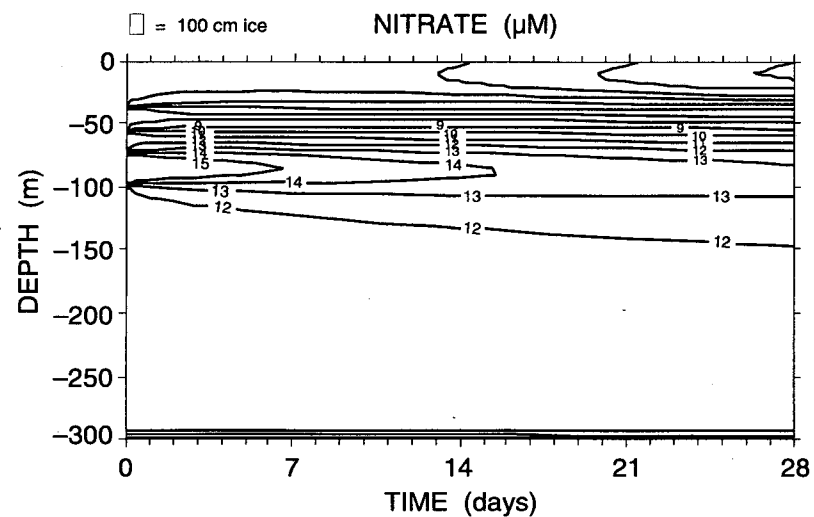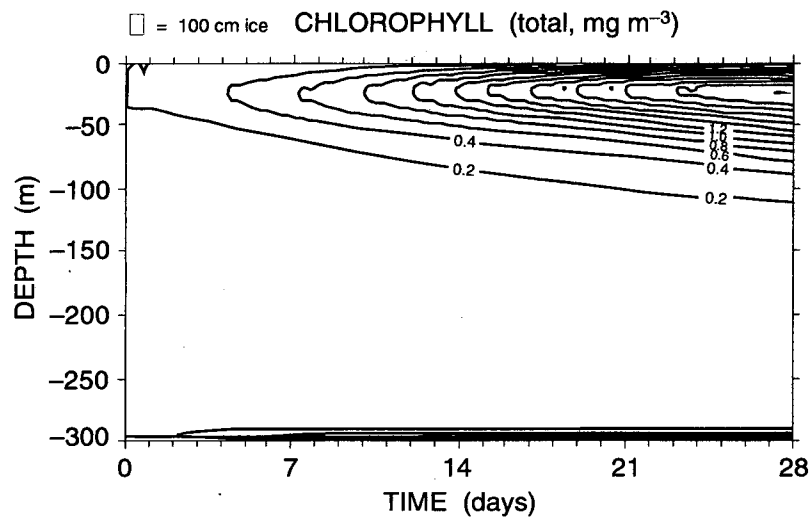
Figure 12. Time series contours over 28 days of data from experiment "23". Dashed lines are negative.
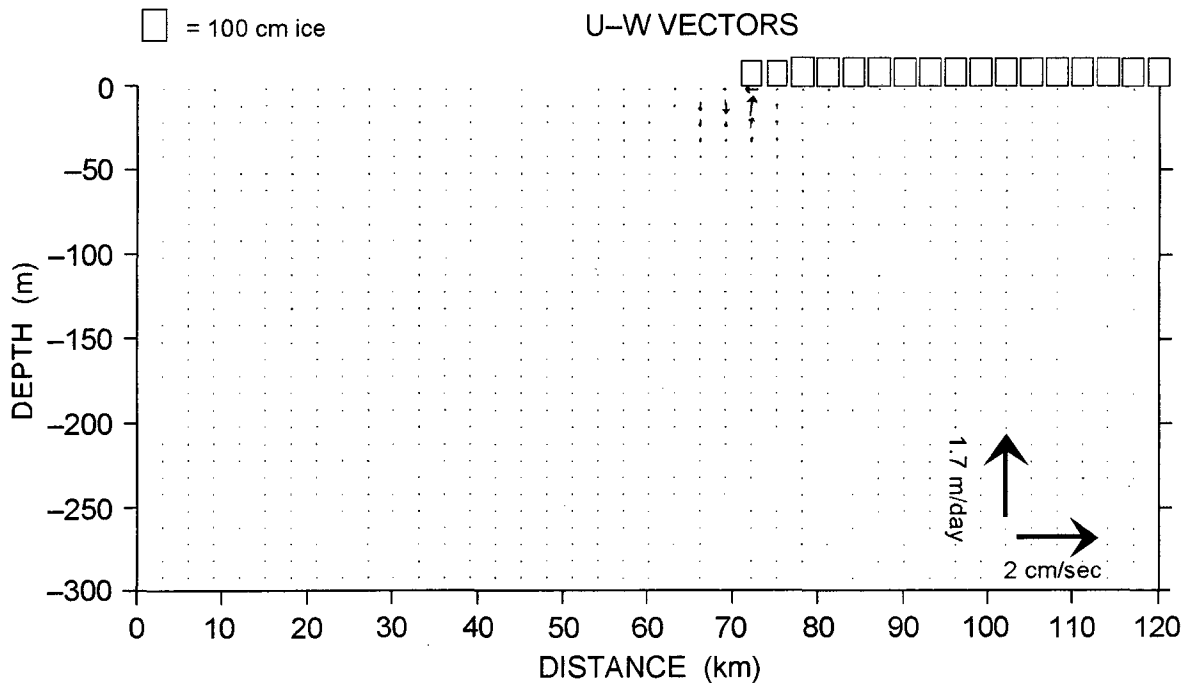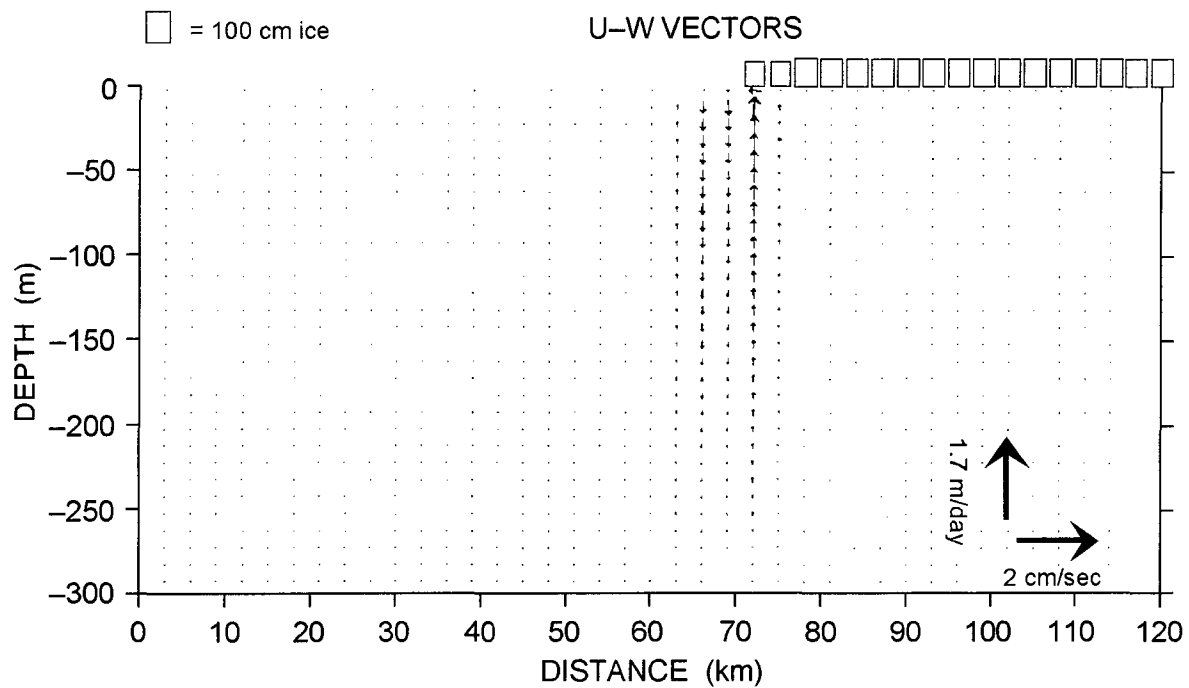
Figure 13. Vector cross sections of the u and w component of the flow on day 7 for experiments "20"and "23".
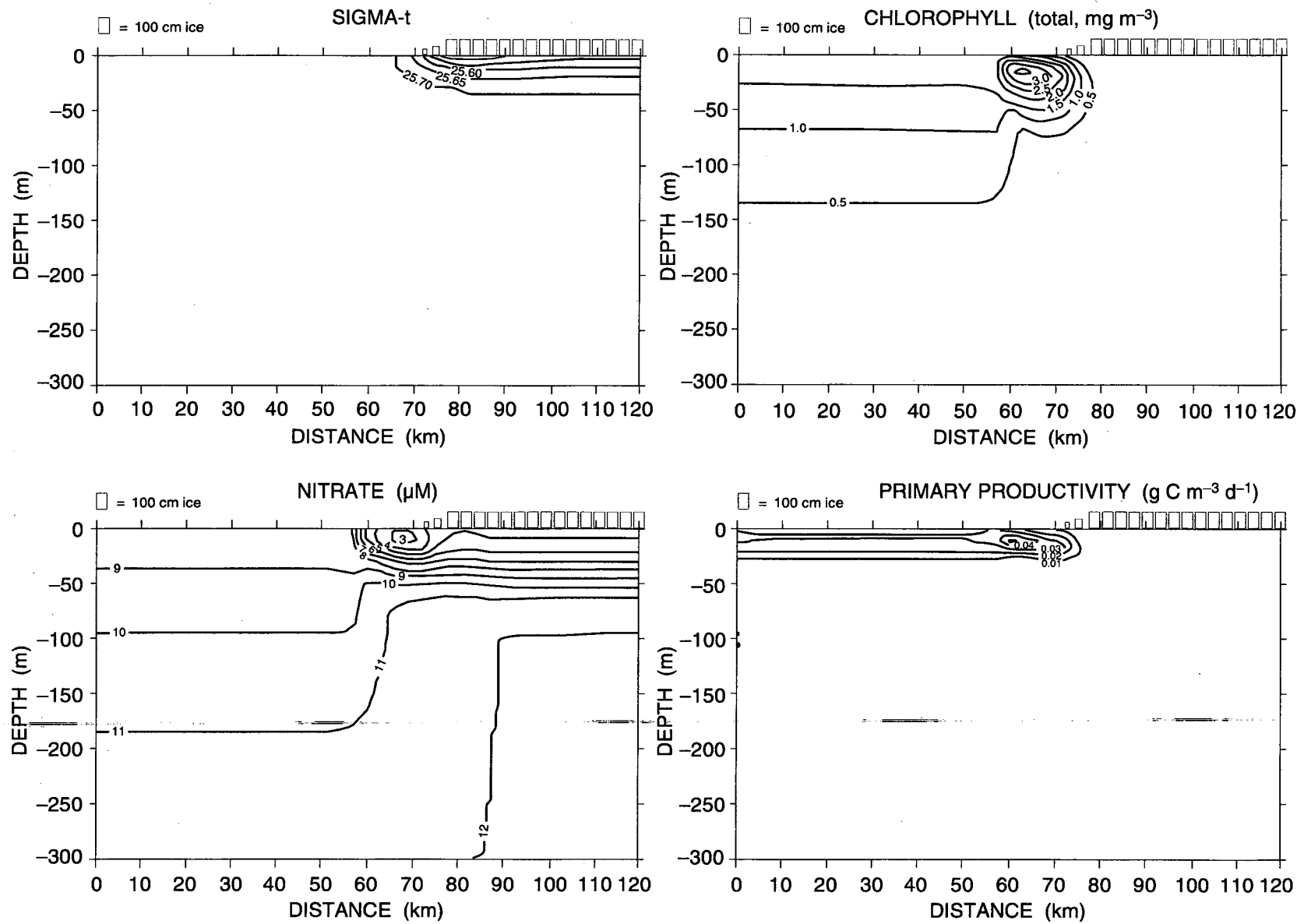
Figure 14a. Cross section contours for data from experiment "20" on day 28.
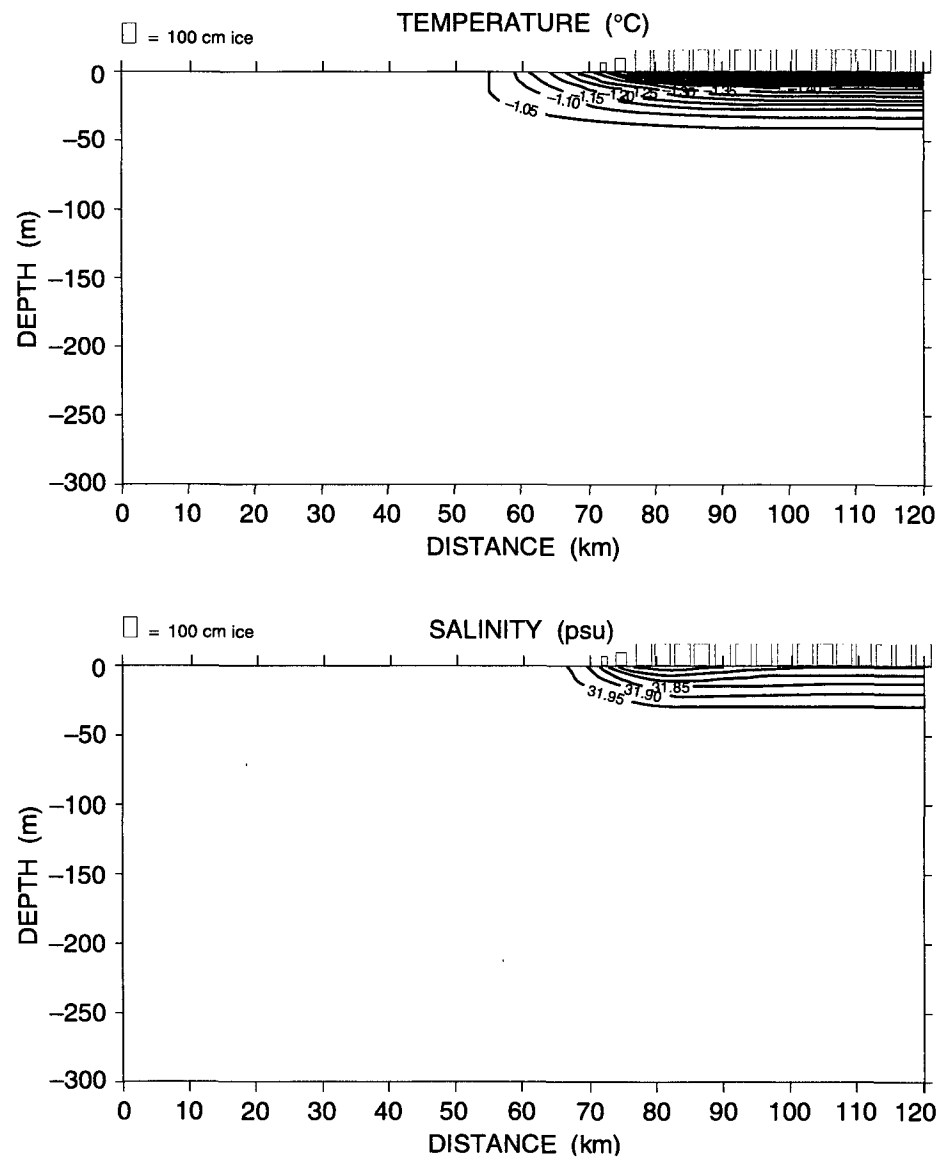
Figure 14b. Cross section contours for data from experiment "20" on day 28.
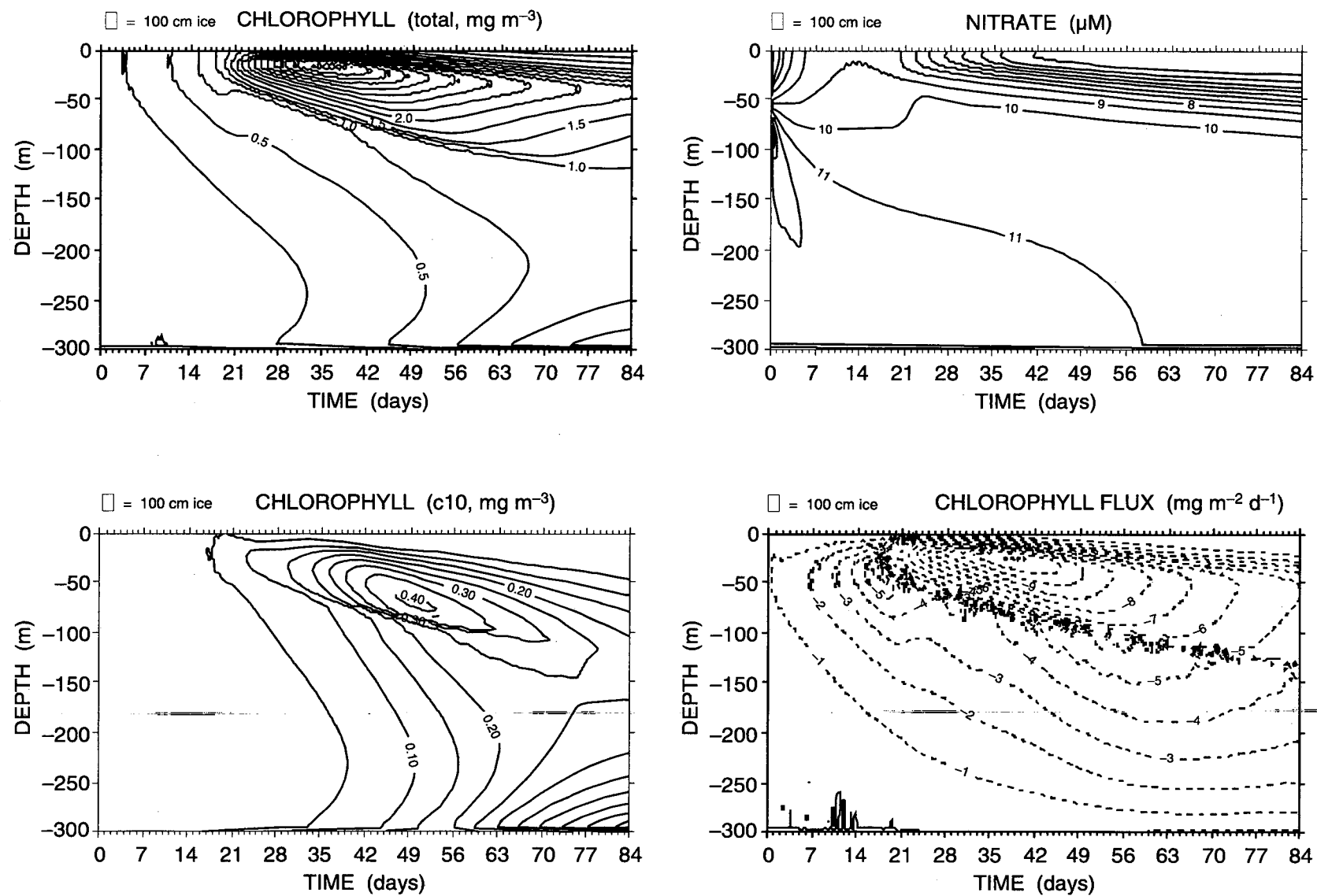
Figure 15a. Time series contours over 84 days of data from experiment "20". Dashed lines are negative.

TEMPERATURE (°C)

□ = 100 cm ice

SALINITY (psu)

□ = 100 cm ice

SIGMA-t

□ = 100 cm ice
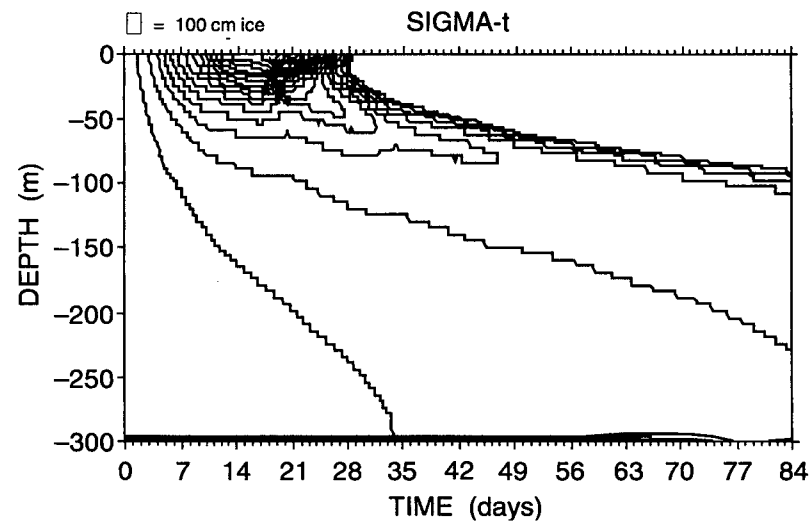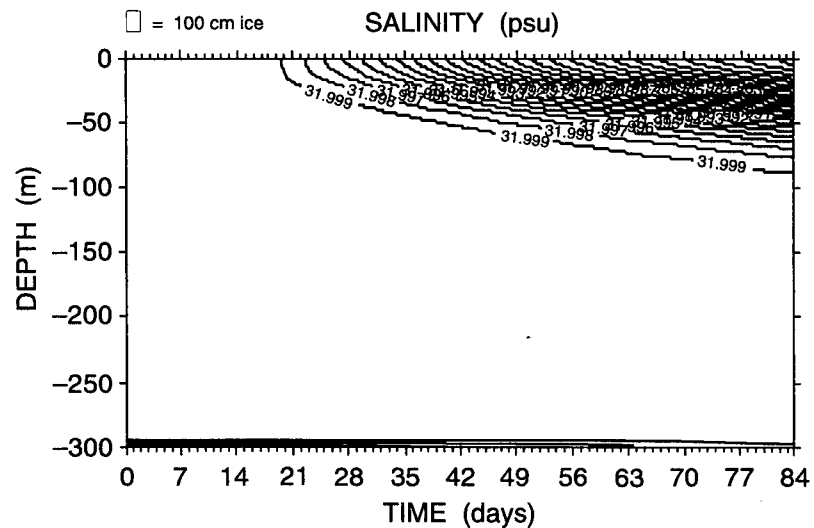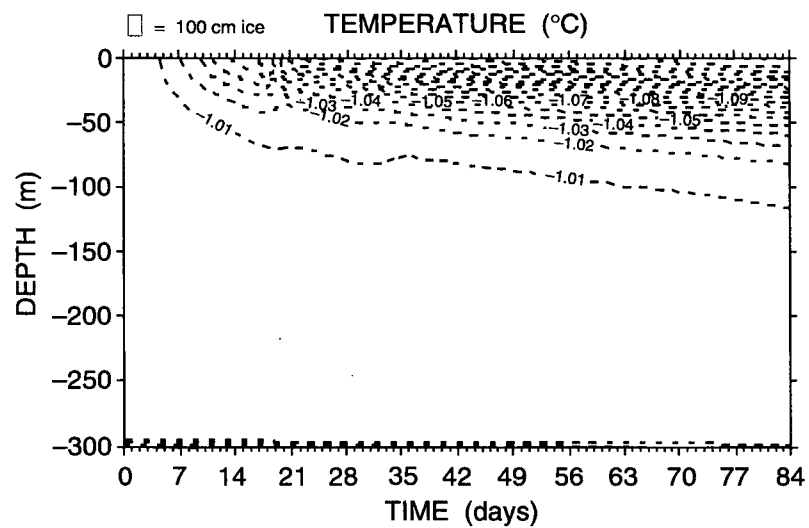
Figure 15b. Time series contours over 84 days of data from experiment "20". Dashed lines are negative. Sigma-t less than 25.722 are not shown for clarity.
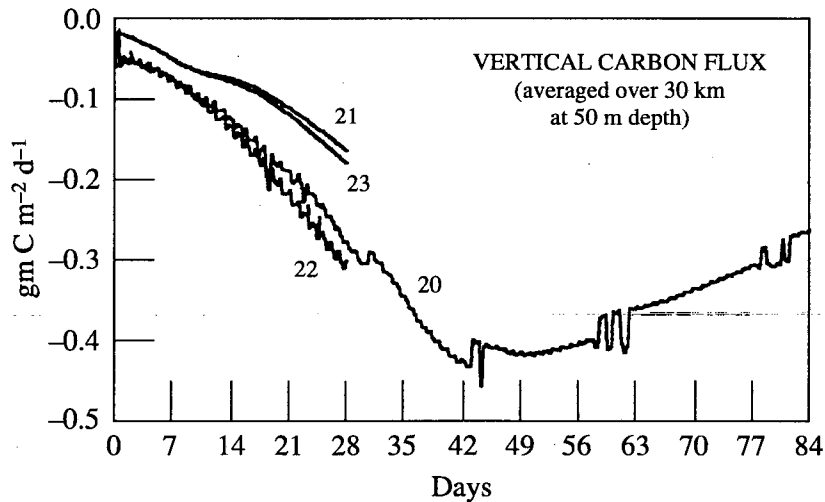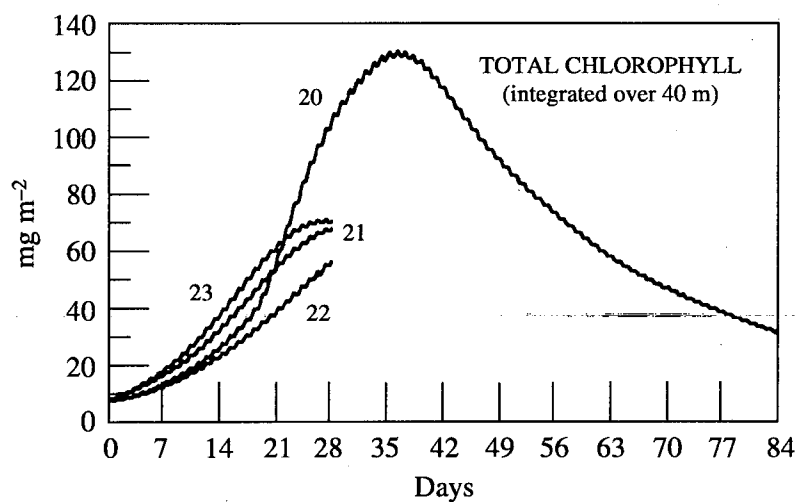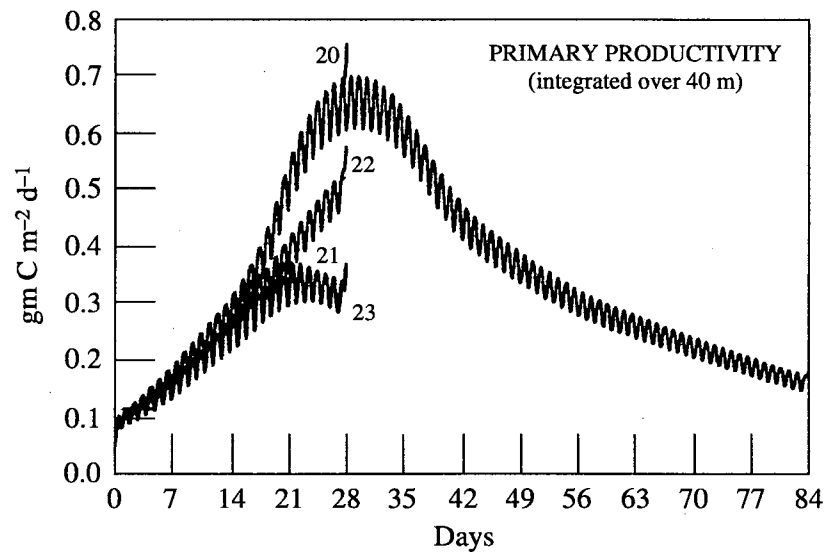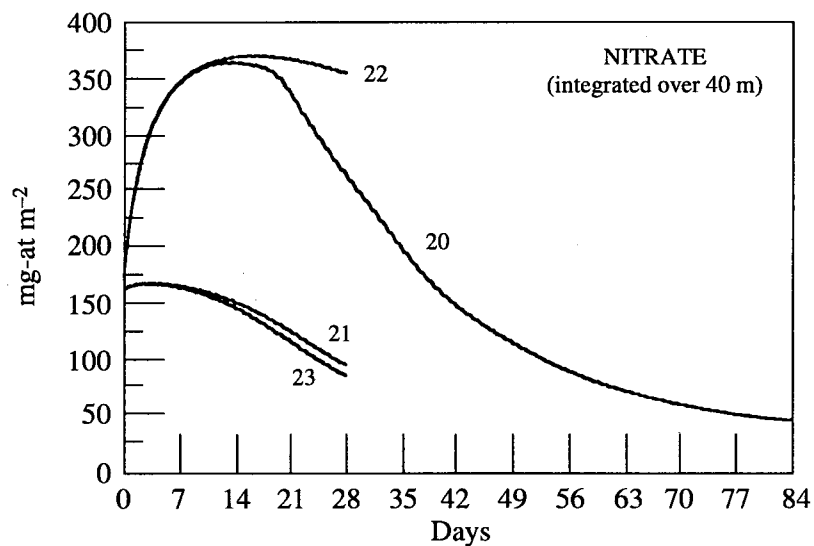
Figure 16. Time series of depth integrated data from the "20" series experiments. Primary productivity is smoothed with a 3-point running mean.
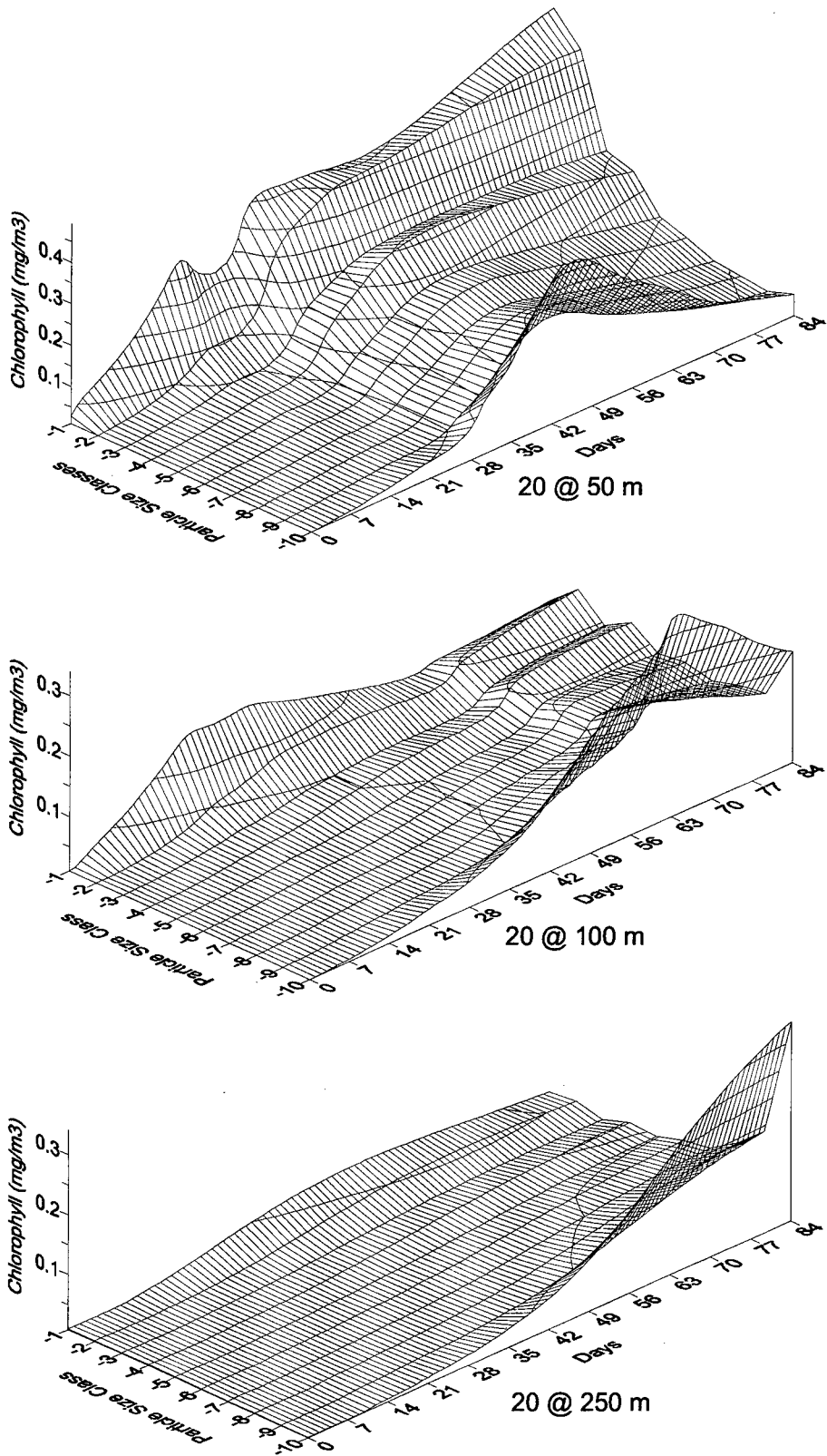
Figure 17. Distribution of particle size classes of chlorophyll over depth and time at depths 50, 100 and 250 m for experiment "20".
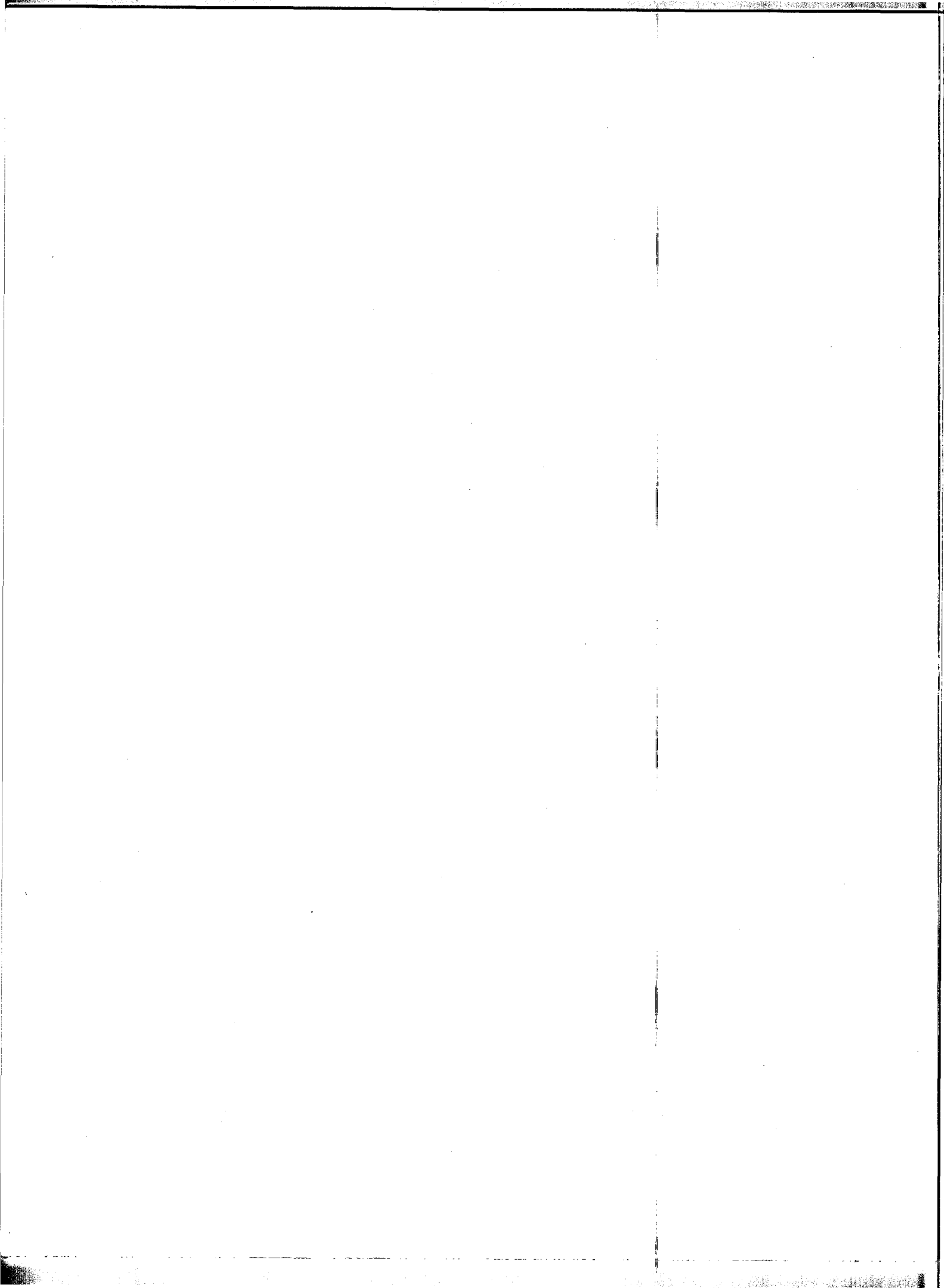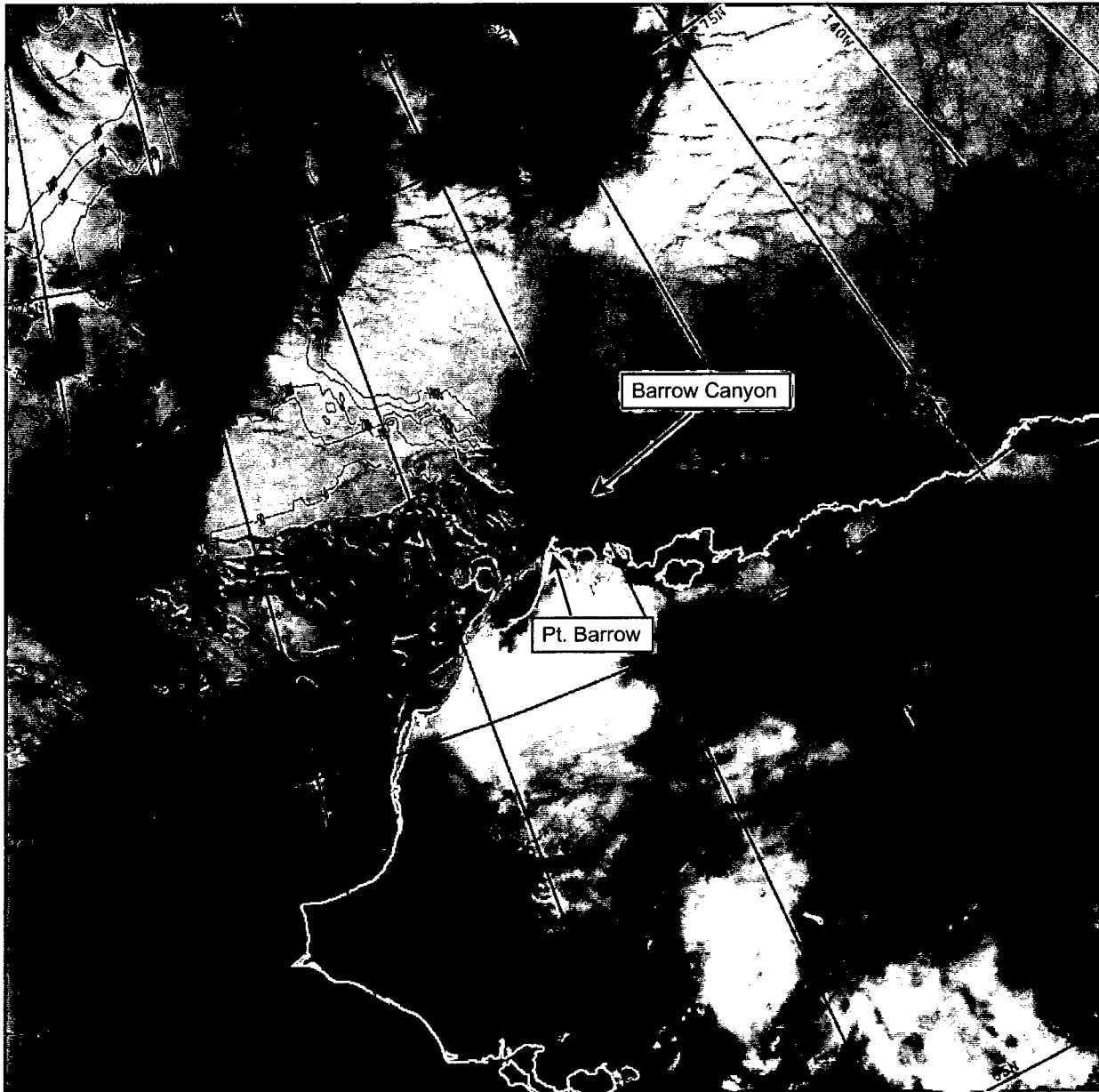
Figure 18. NOAA 12 satellite image of the Chukchi and Beaufort Seas off of the north coast of Alaska for 15 December 1994. Sea ice is light grey in color while open water is darker over the ocean part of the image. This divergence in the ice pack was caused by storm winds. Air temperatures were well below freezing so that there must have been considerable cold, salty brine produced by ice formation, especially right over and upstream of the Barrow Canyon.
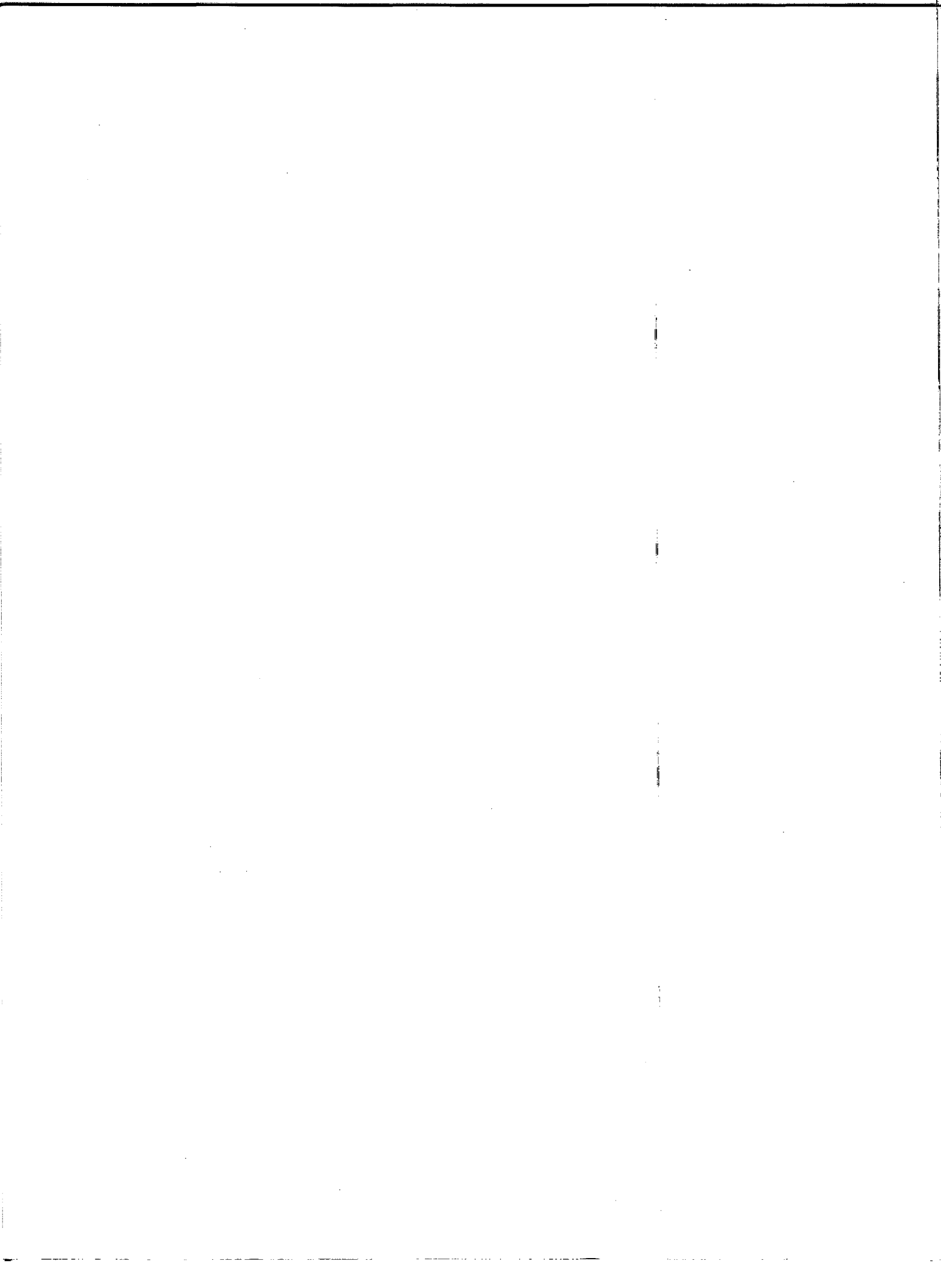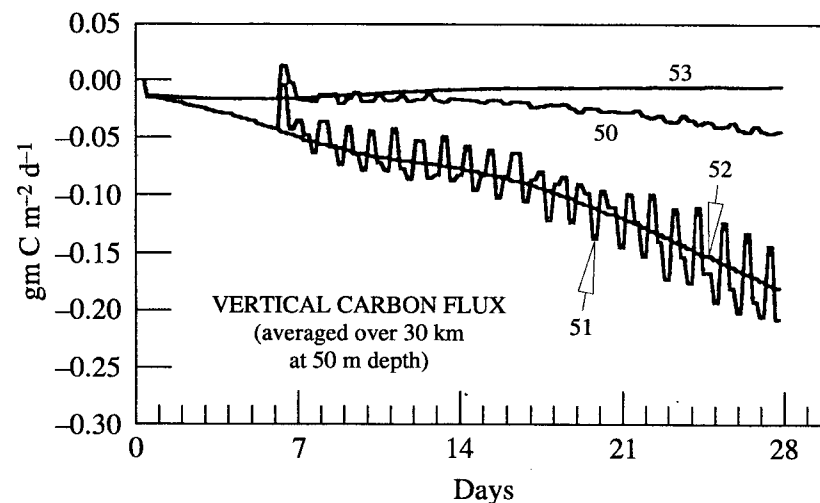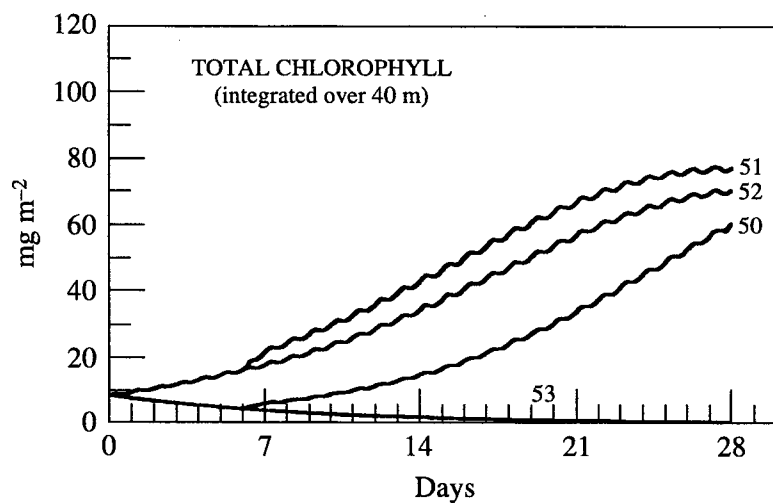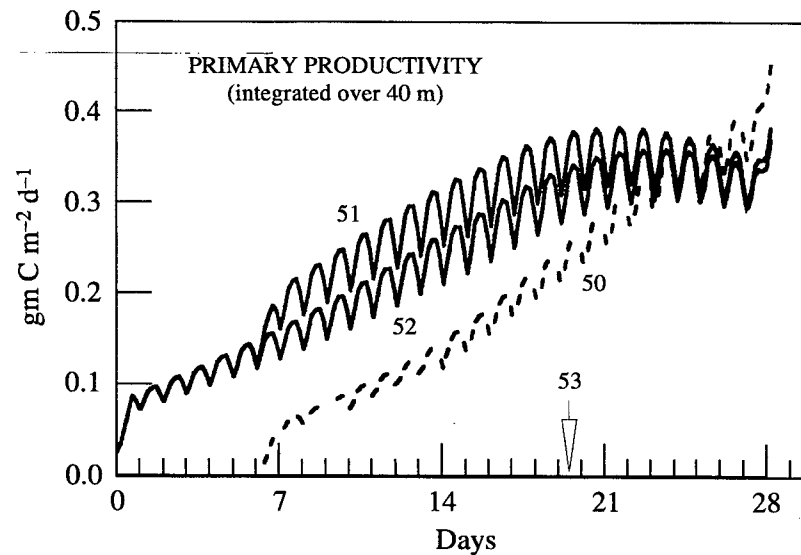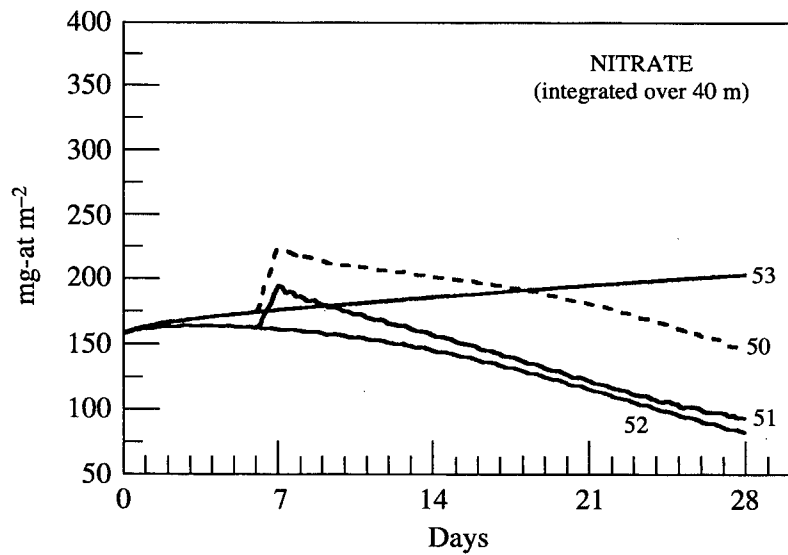
Figure 19. Time series of depth integrated data from the "50" series experiments. Primary productivity is smoothed with a 3-point running mean.
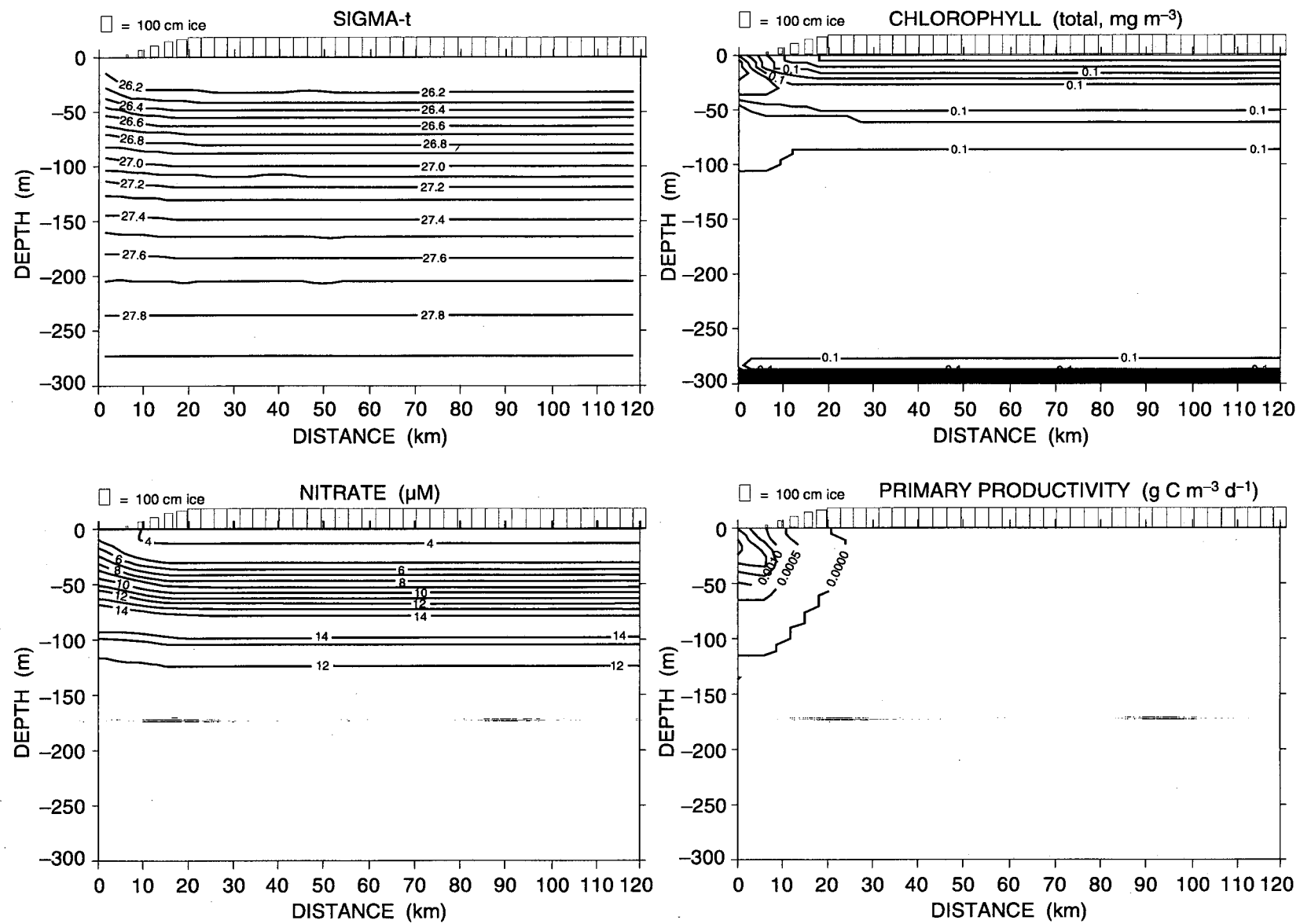
Figure 20. Cross section contours for data from experiment "50" on day 7.
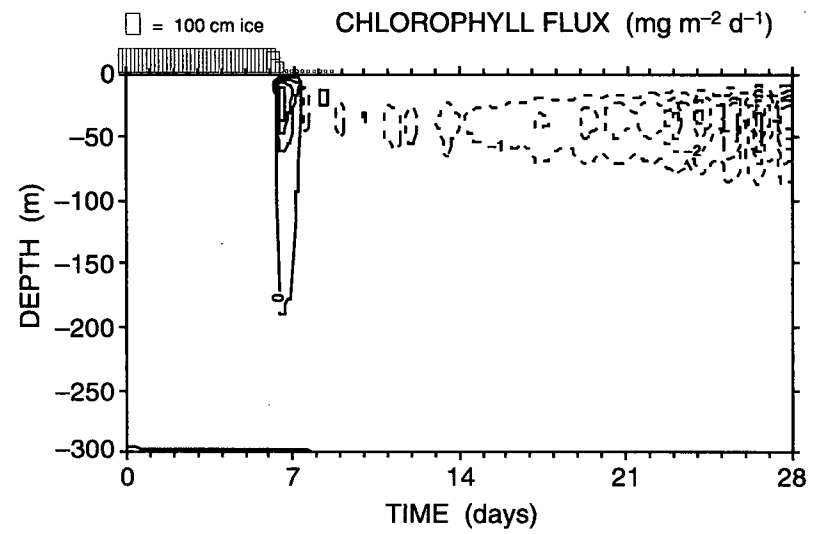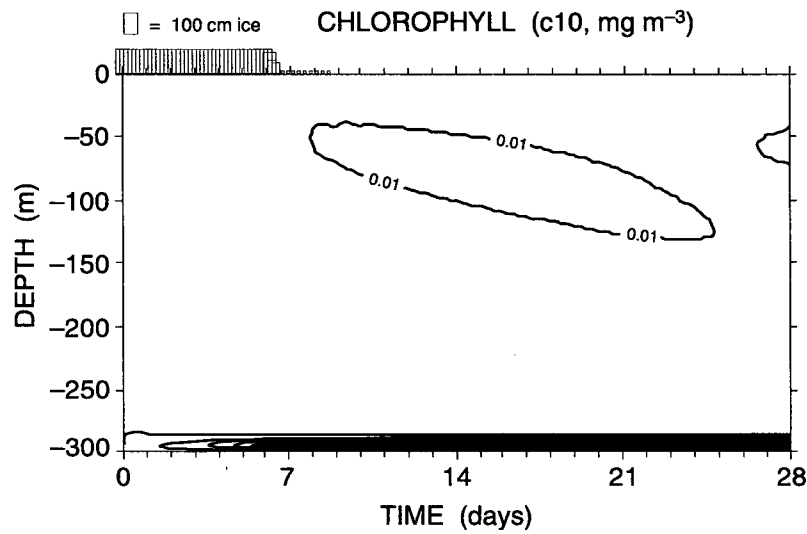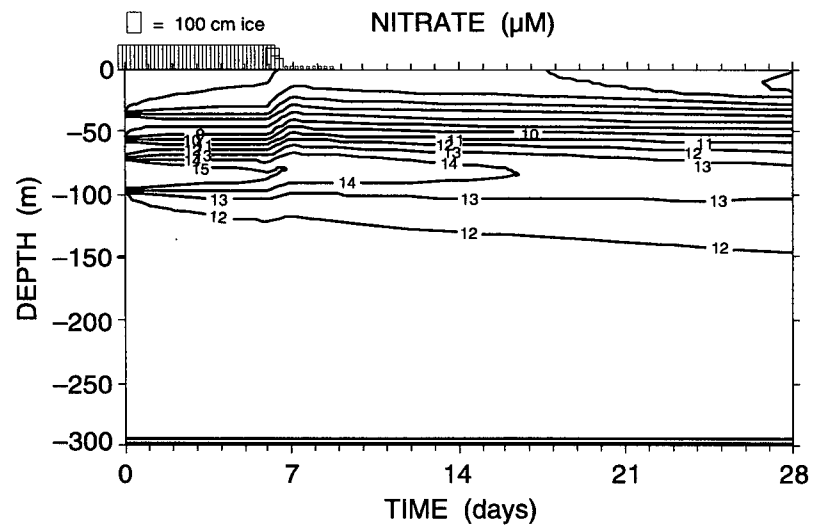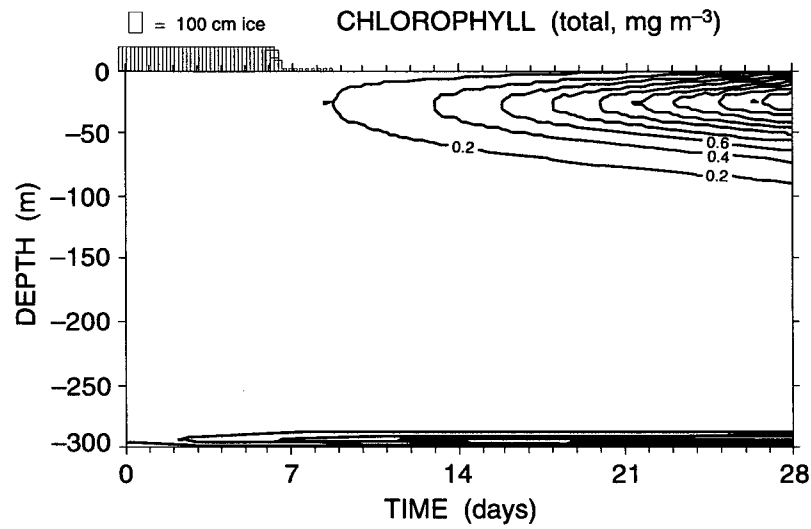
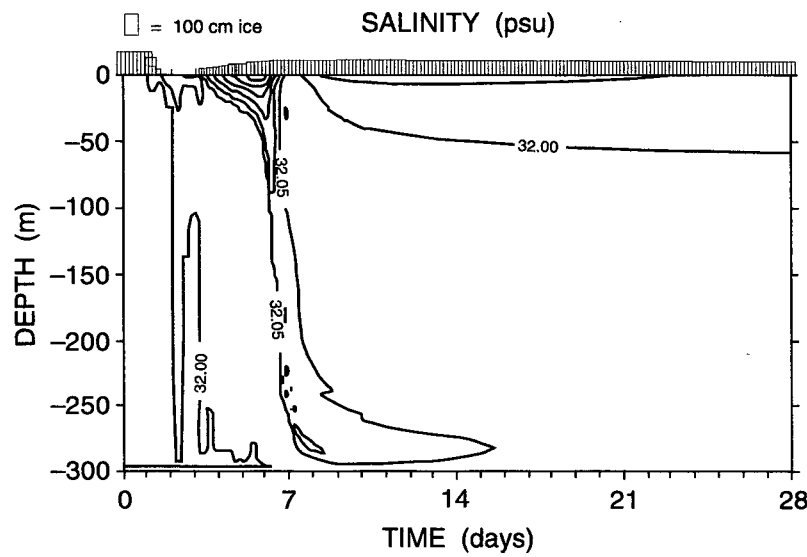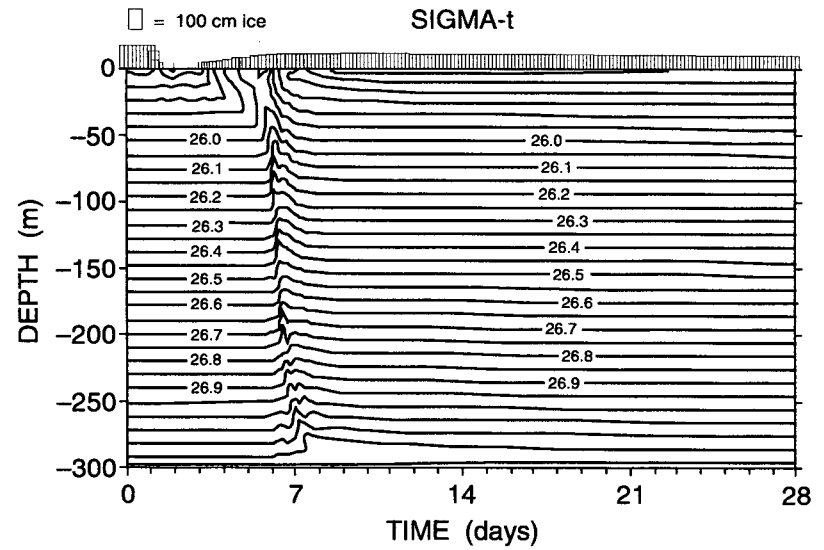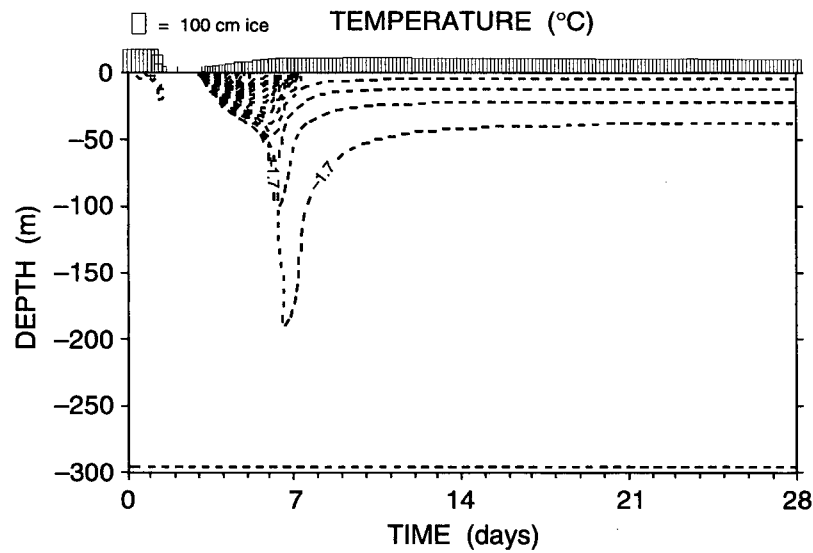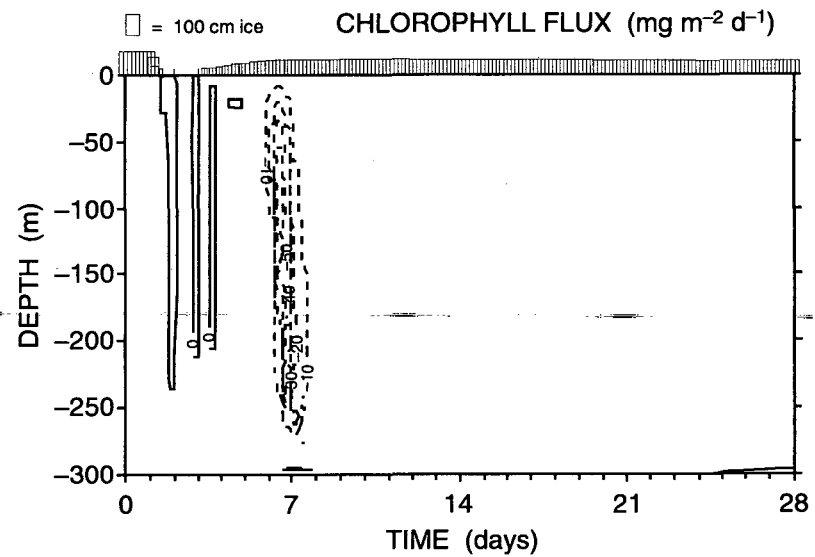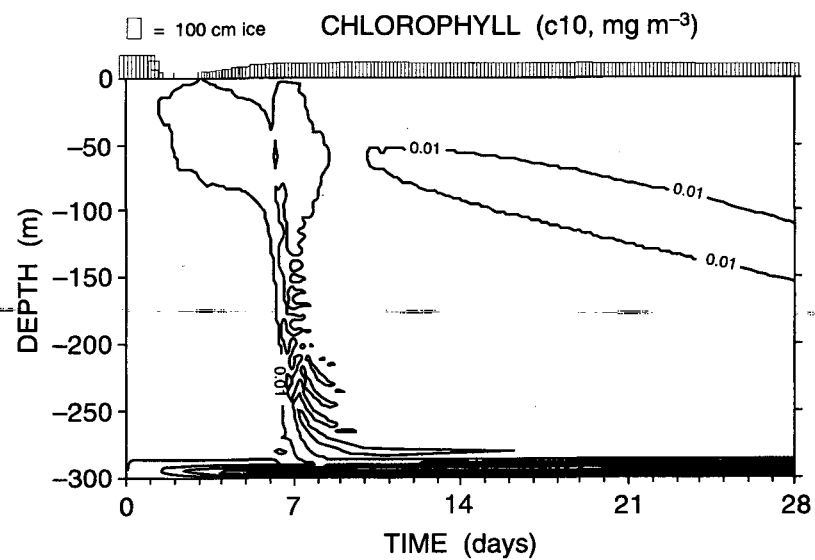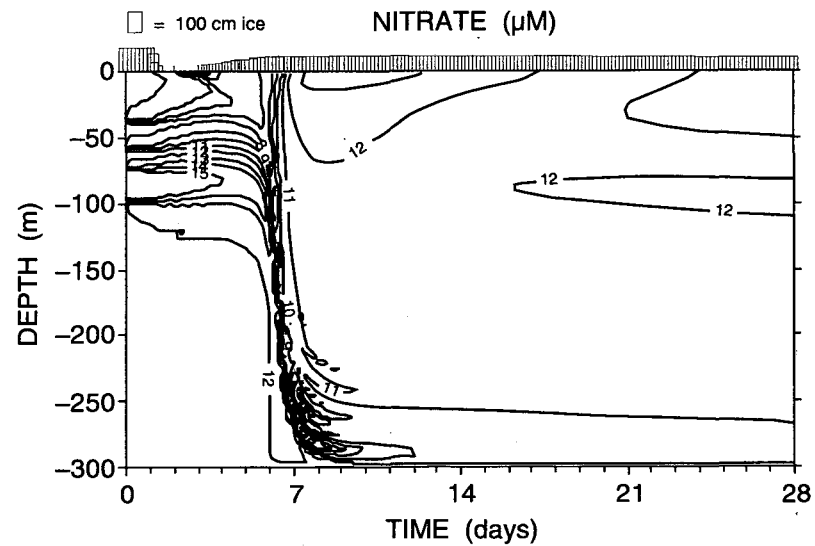Figure 21. Time series contours over 28 days of data from experiment "50". Dashed lines are negative.
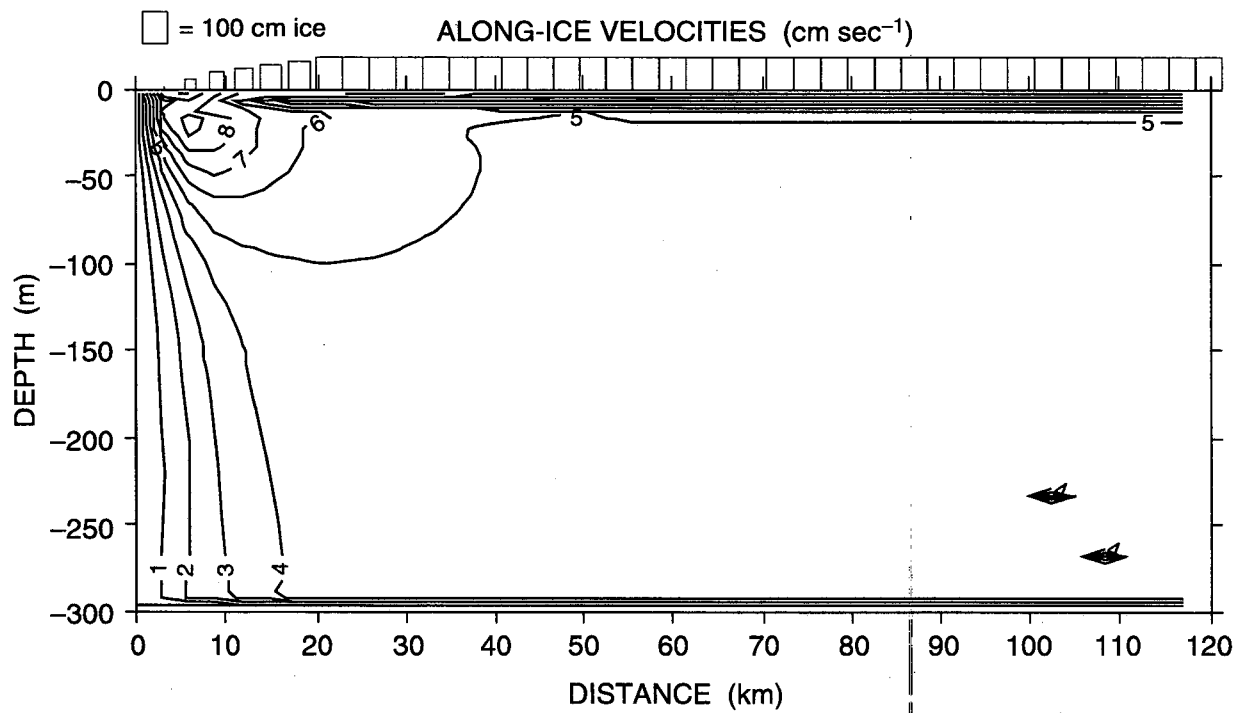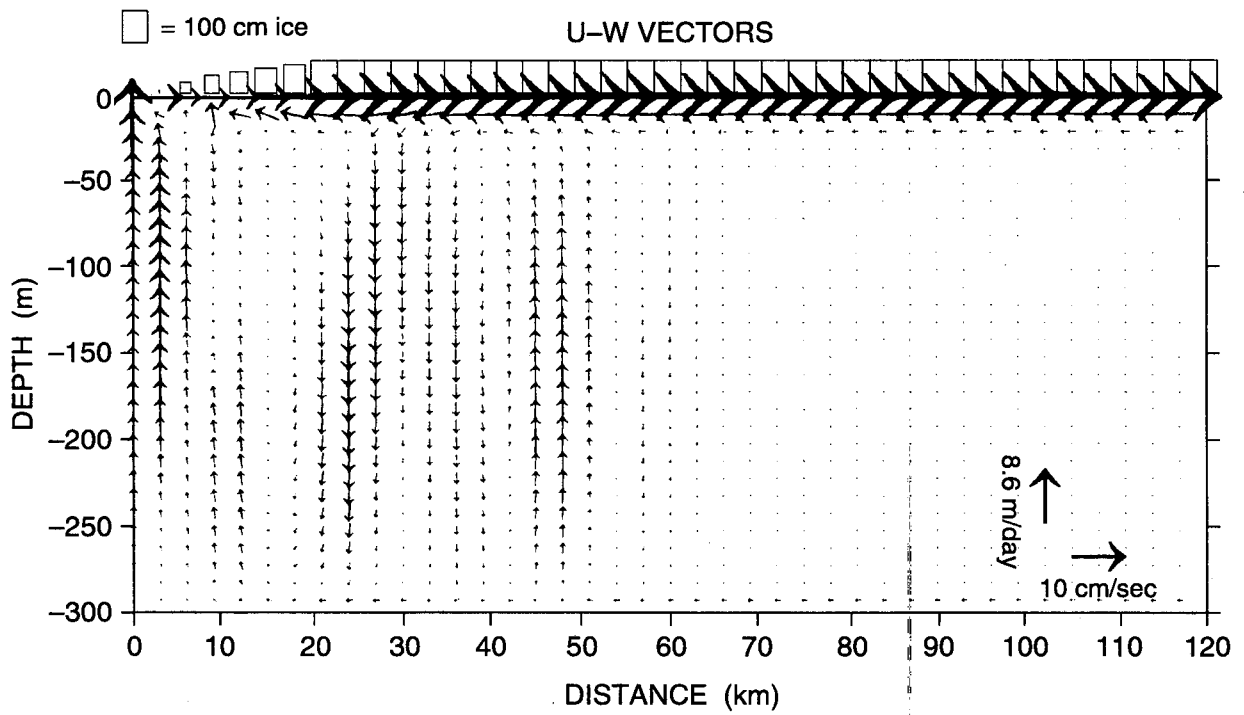
Figure 22. Ocean currents in vector cross sections of the u and w (top panel), and along-ice v
component (bottom panel) for experiment "50" on day 7. Positive flow is into page.
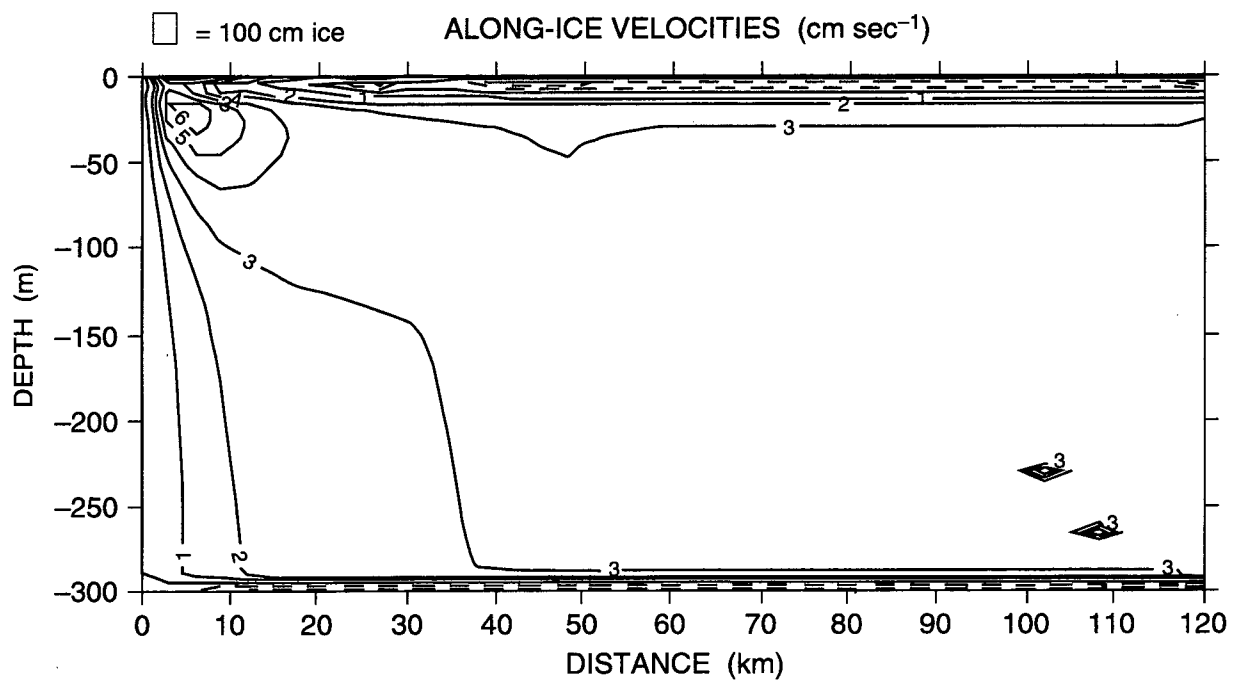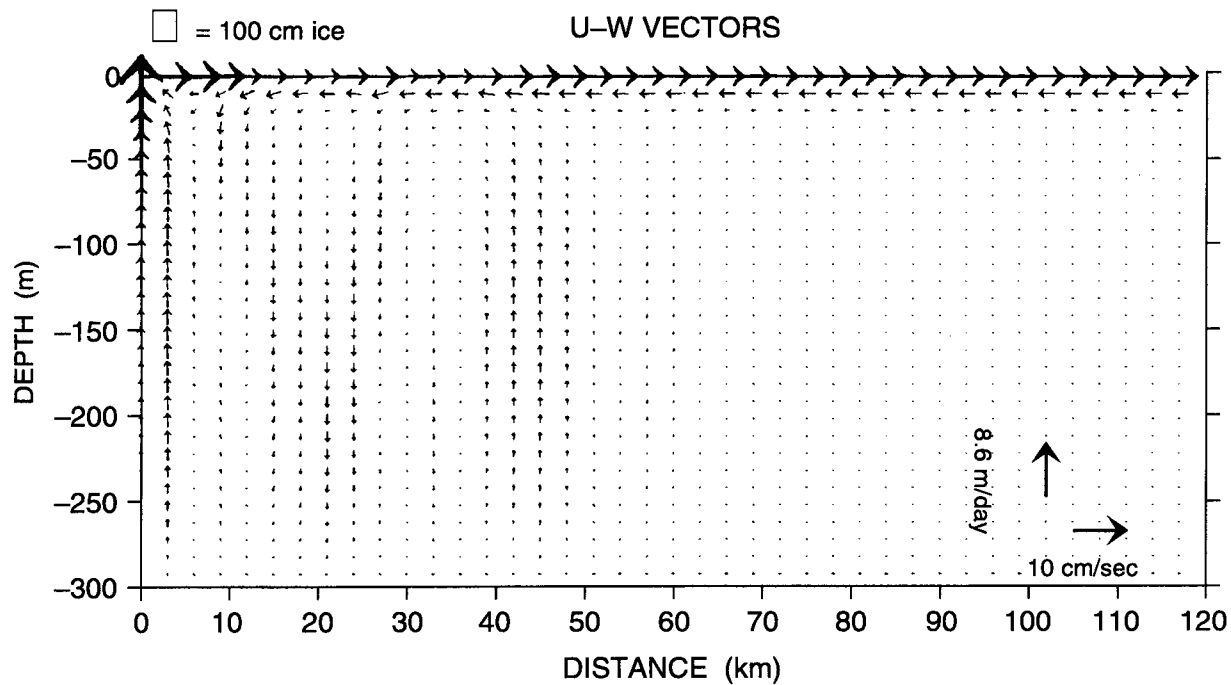
Figure 23. Ocean currents in vector cross sections of the u and w (top panel), and along-ice v component (bottom panel) for experiment "51" on day 7. Positive flow is into page.
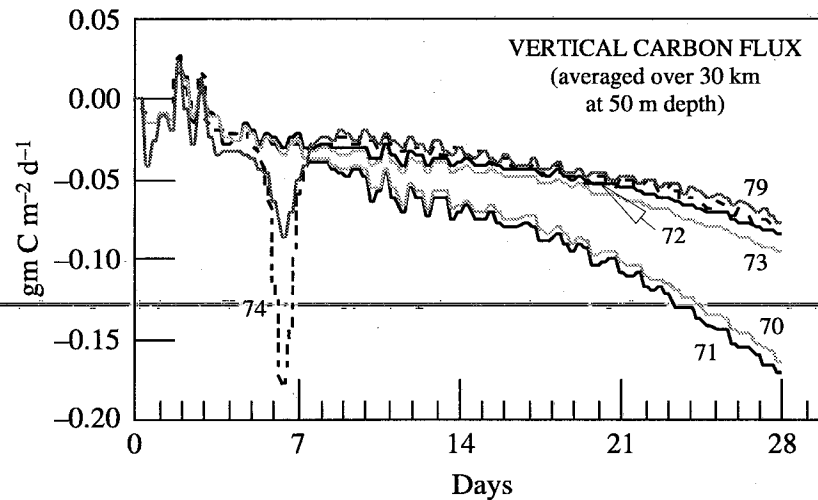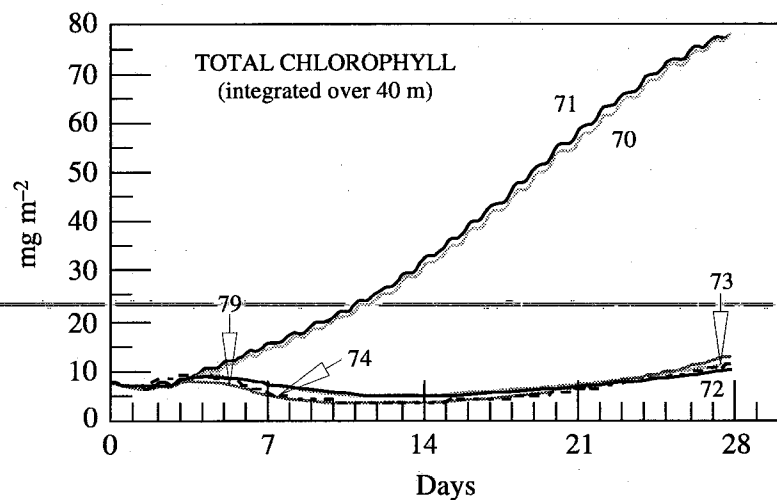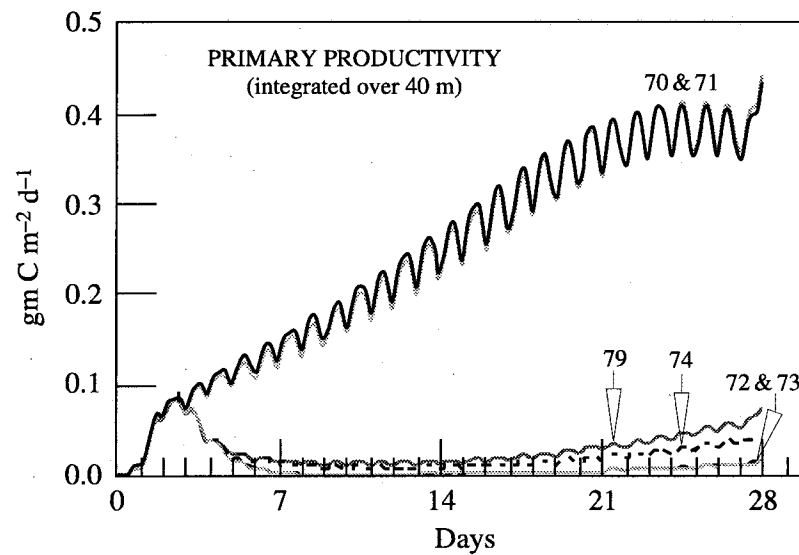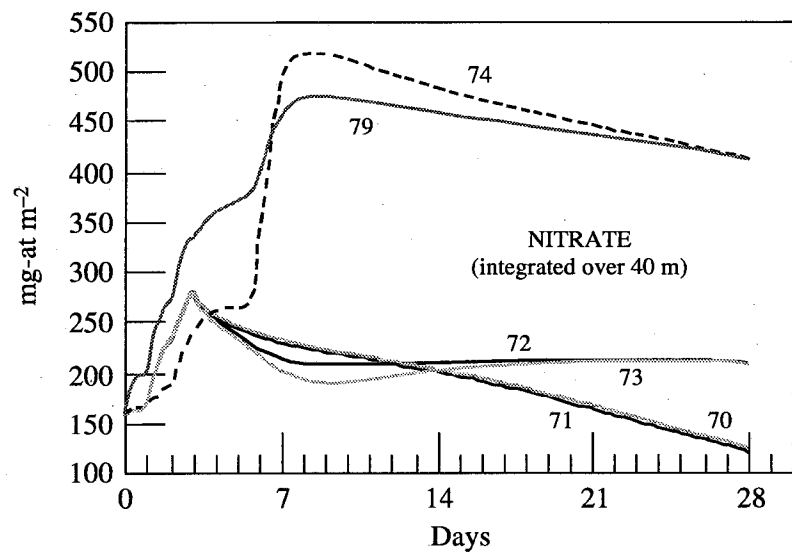
Figure 24. Time series of depth integrated data for the "70" series experiments. Primary productivity is smoothed with a 3-point running mean. "74" is dashed.

Figure 25. Cross section contours for data from experiment "70" on day 3.
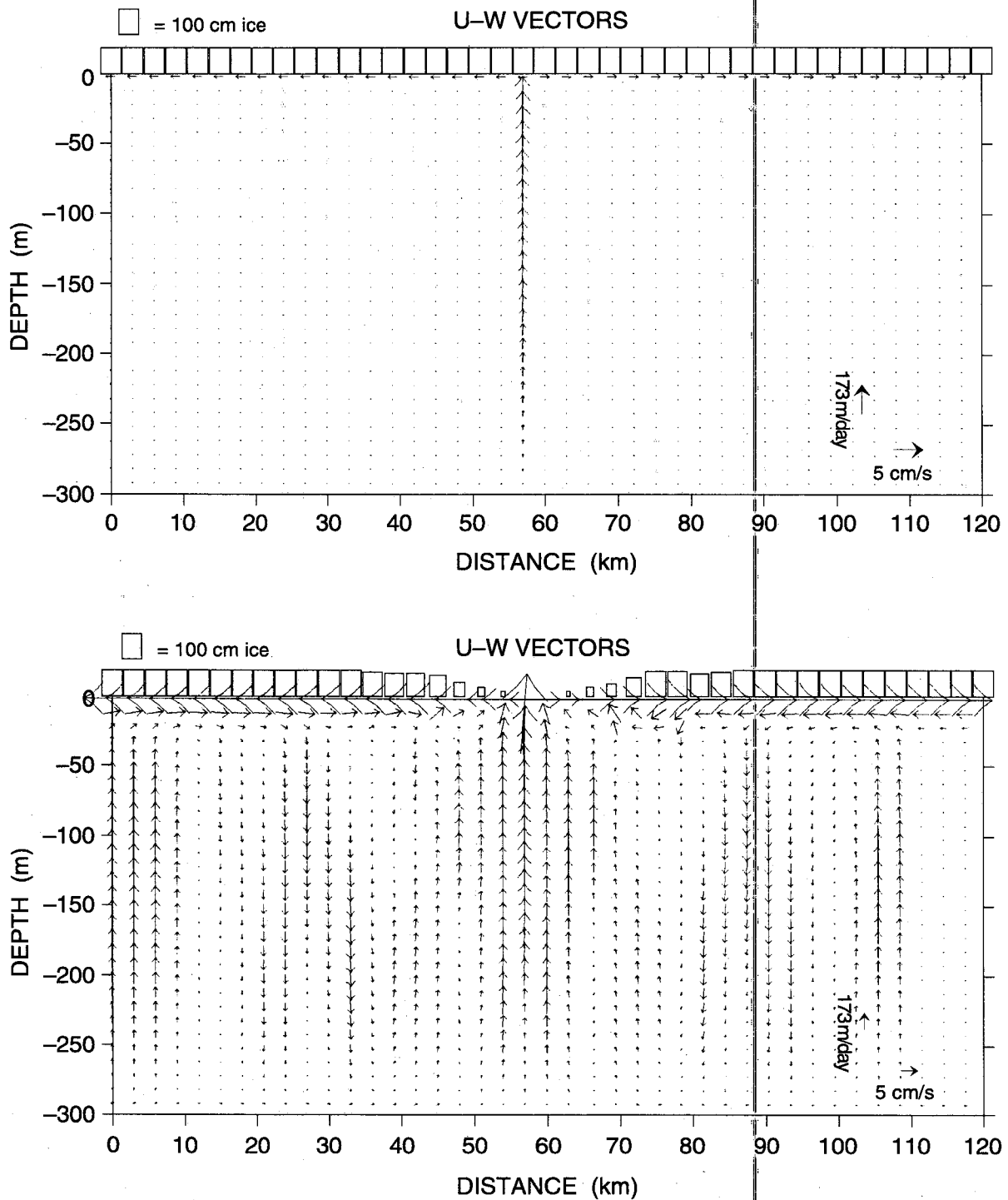
Figure 26a.   Vector cross sections of the u and w component of the flow at the end of days 1 (top panel) and 2 (bottom panel) for all of the "70" series experiments.
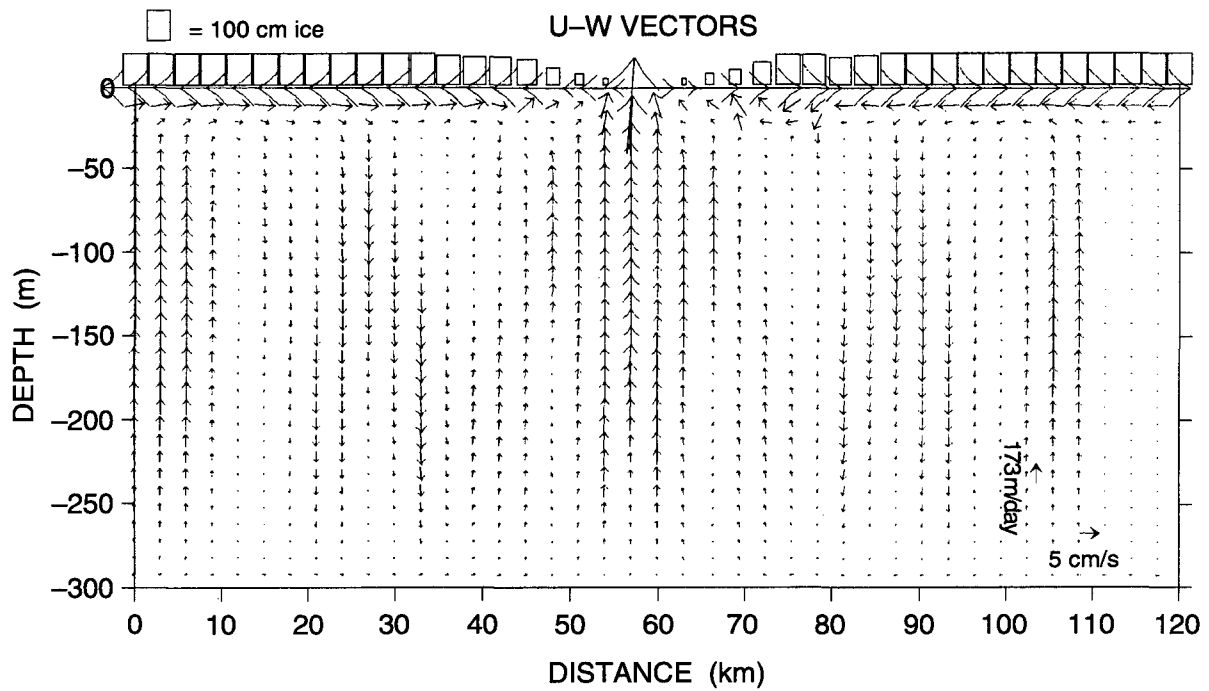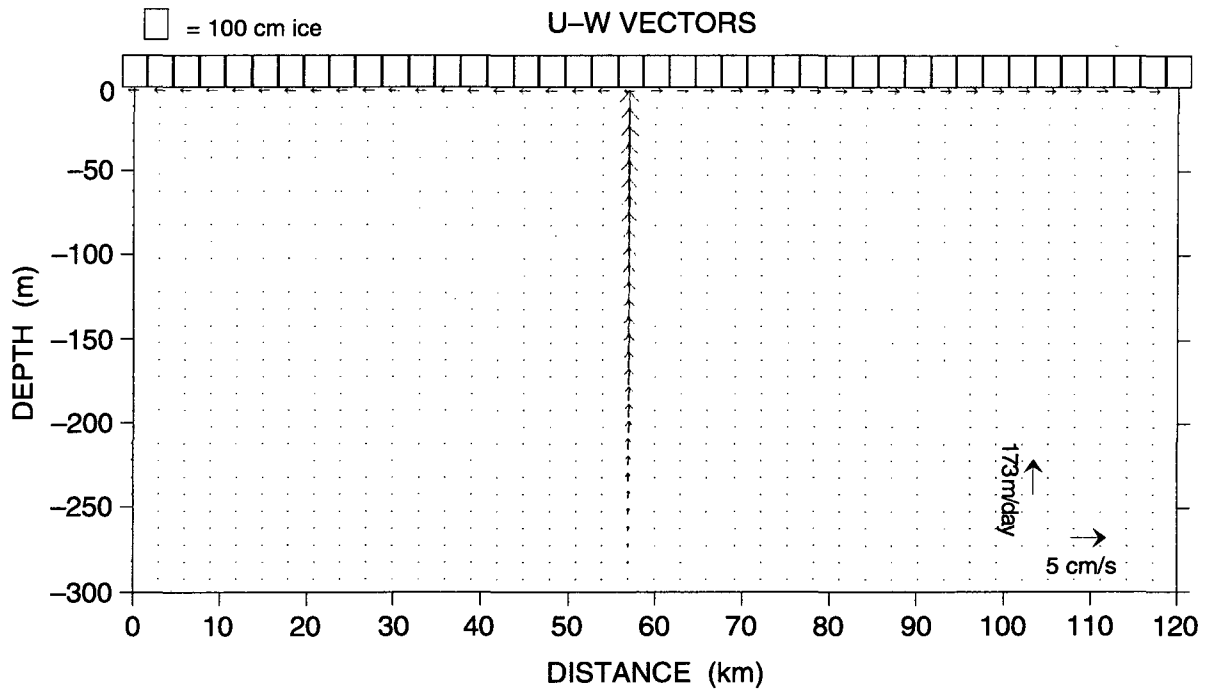
Figure 26b.   Same as Figure 26a except for end of day 3 (top panel) and day 4 (bottom panel).
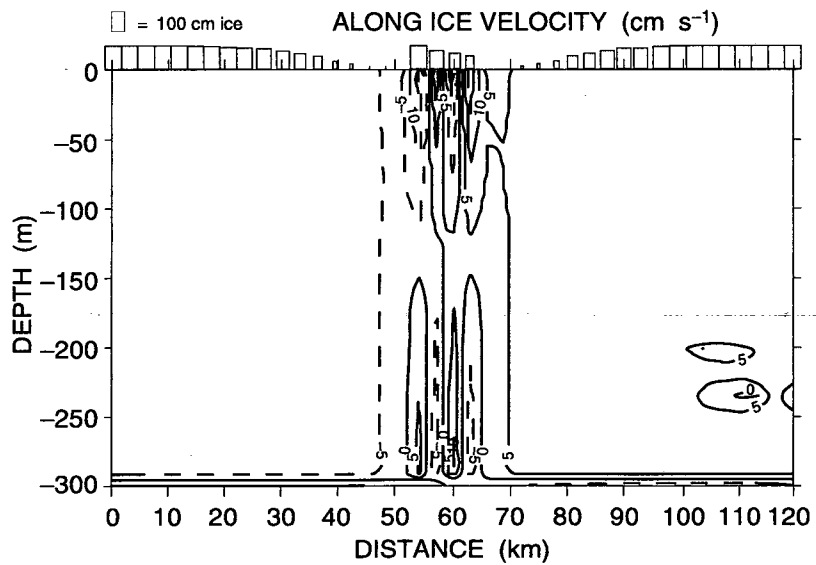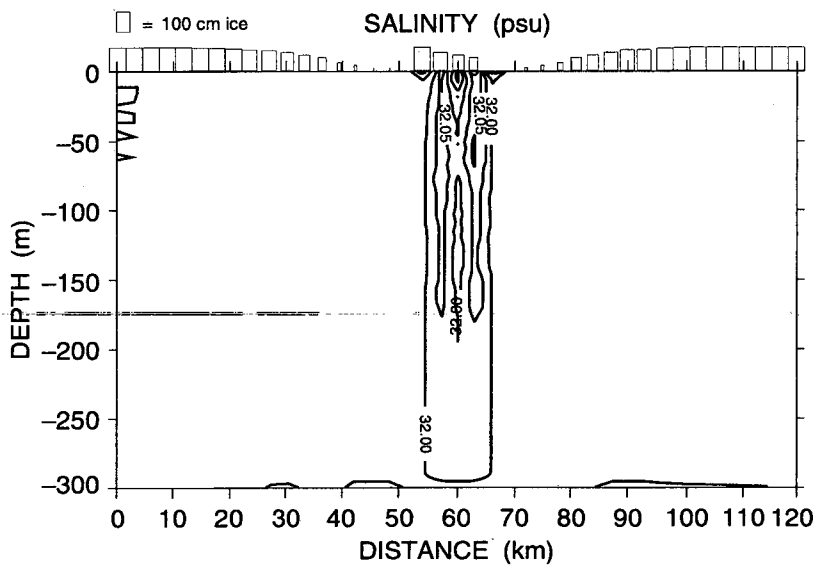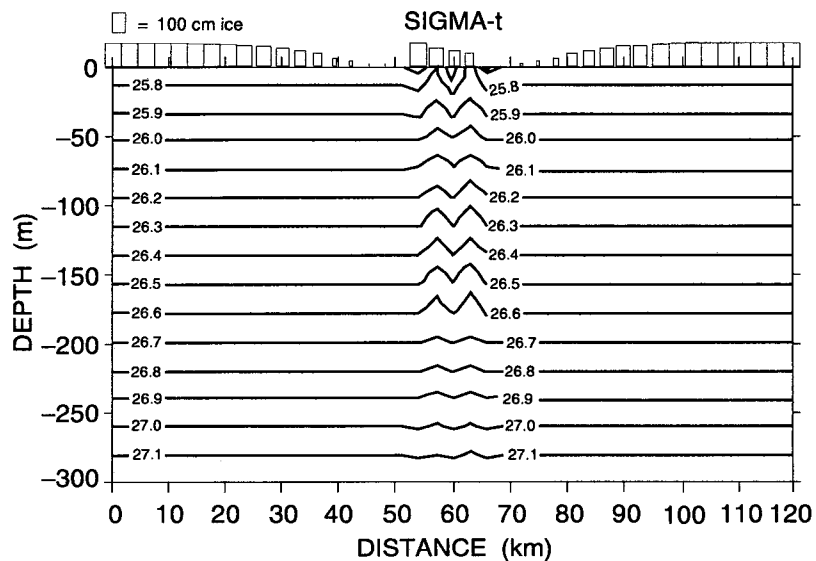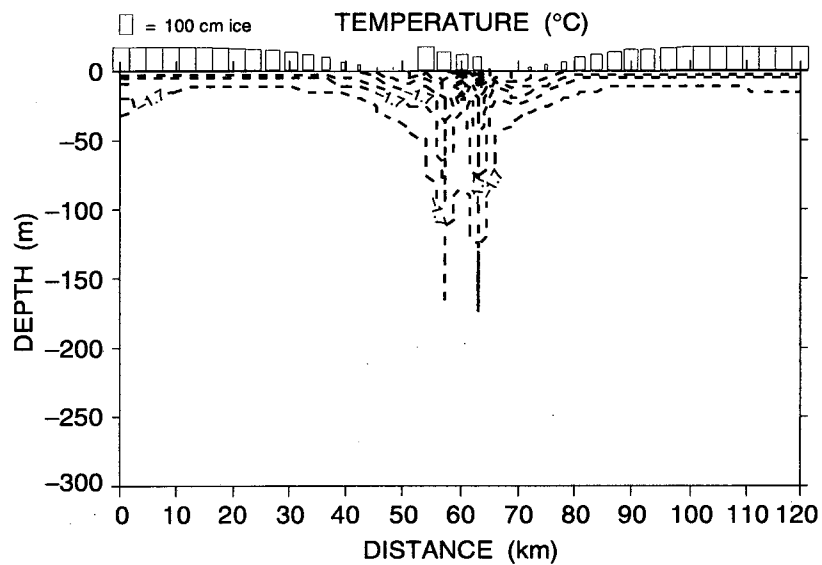
Figure 27a. Cross section contours for data at day 6.4 from experiment "74". Dashed lines are negative.
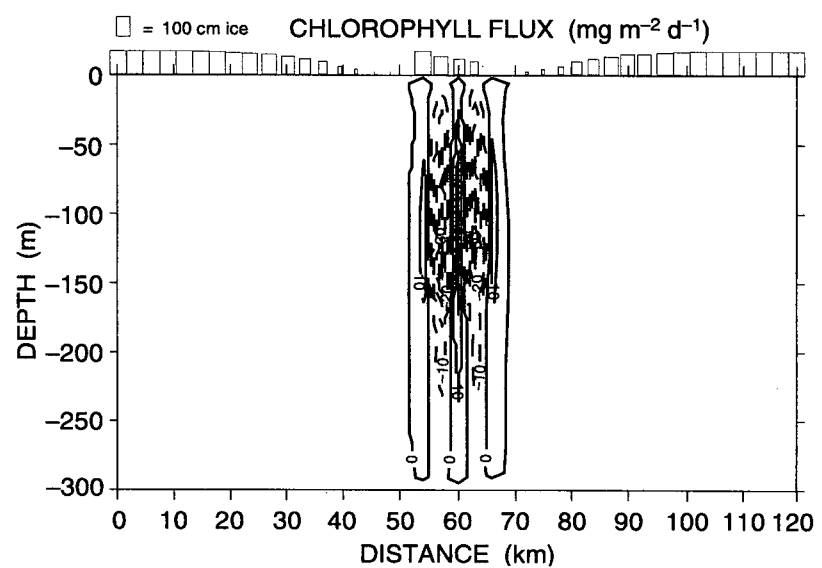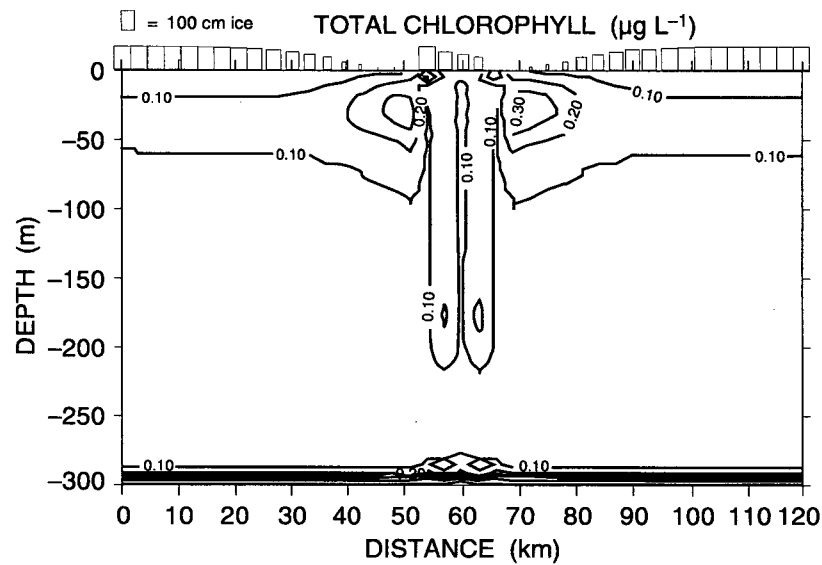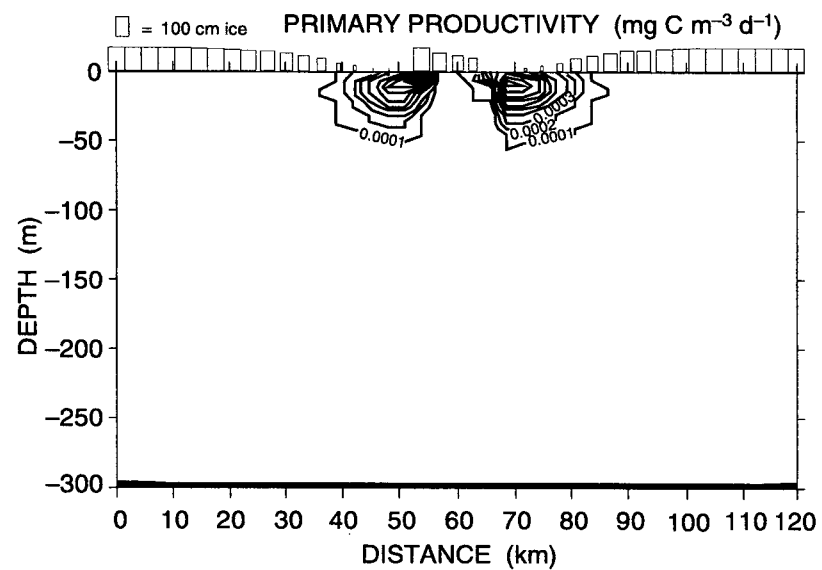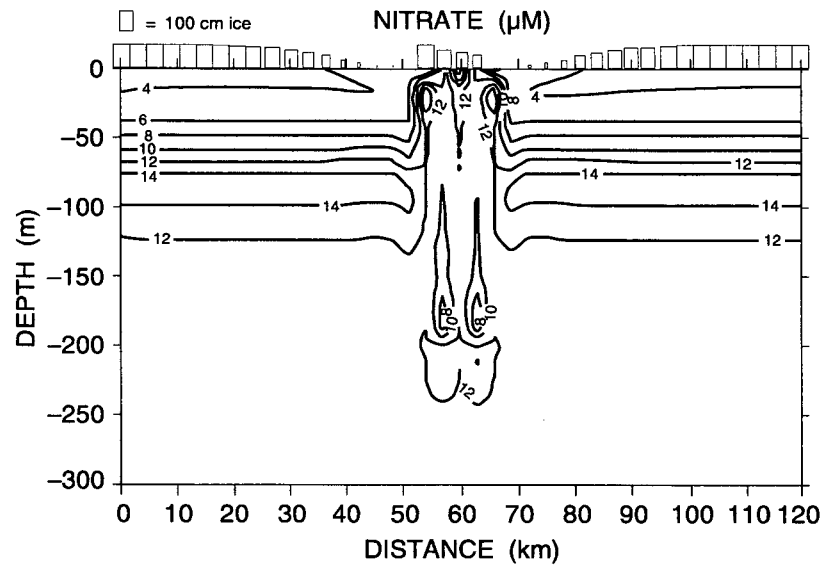
Figure 27b. Cross section contours for data at day 6.4 from experiment "74". Dashed lines are negative.
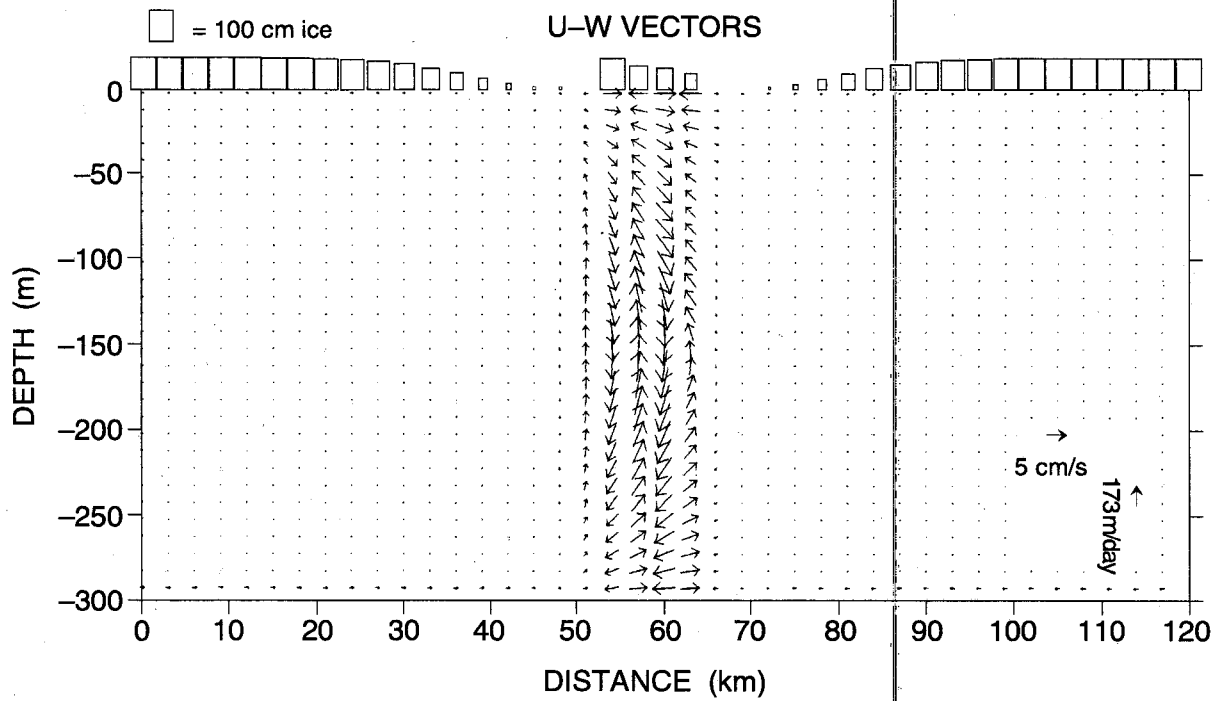
Figure 28. Vector cross sections of the u and w component of the flow at day 6.4 for experiment "74".

Figure 29a. Time series contours over 28 days of data from experiment "74". Dashed lines are negative.
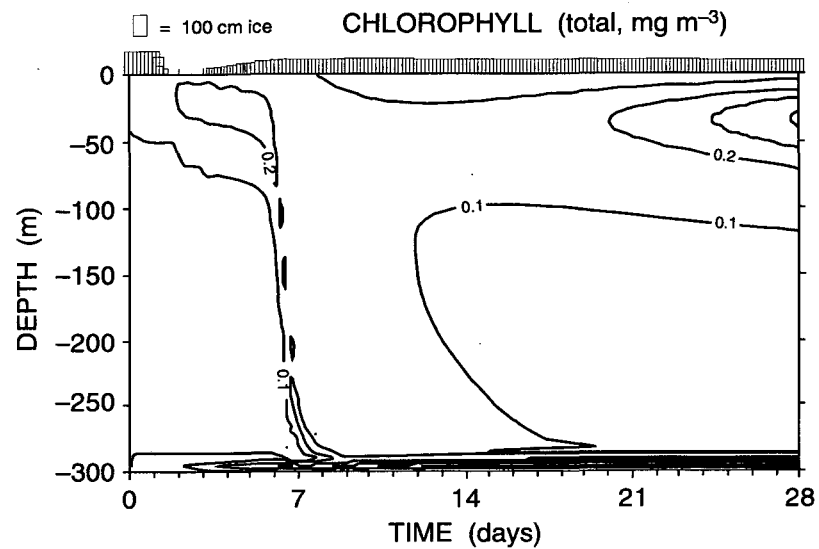
Figure 29b. Time series contours over 28 days of data from experiment "74". Dashed lines are negative.
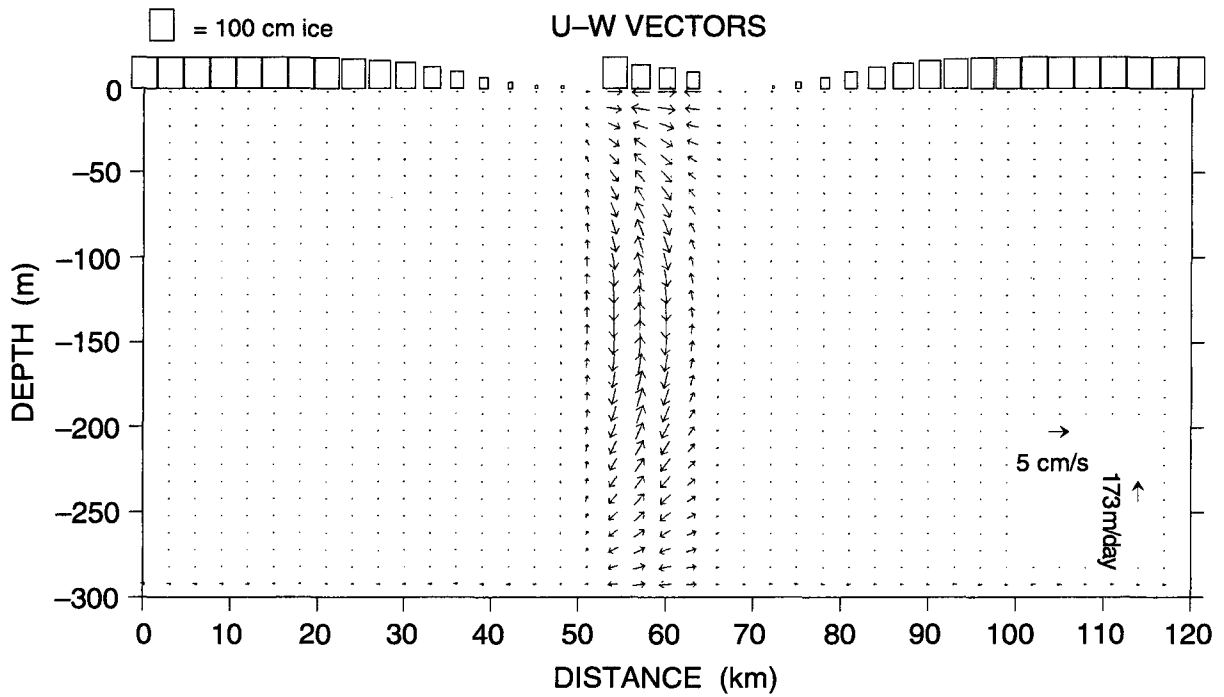
Figure 30. Vector cross sections of the u and w component of the flow at day 6.4 for experiment "79".
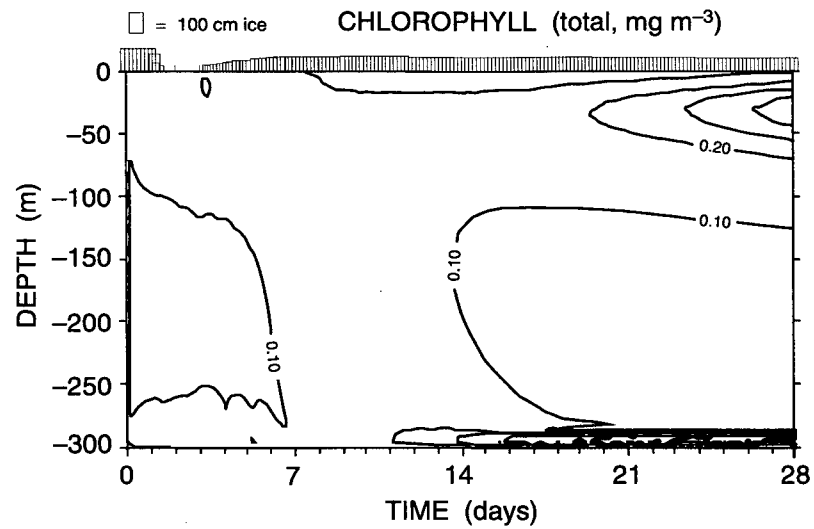
Figure 31a. Time series of the physical data for experiment "79". Dashed lines are negative.
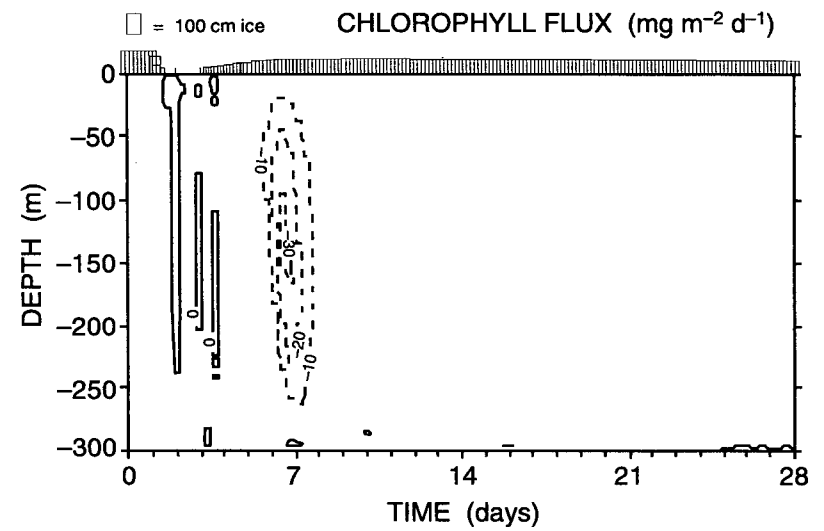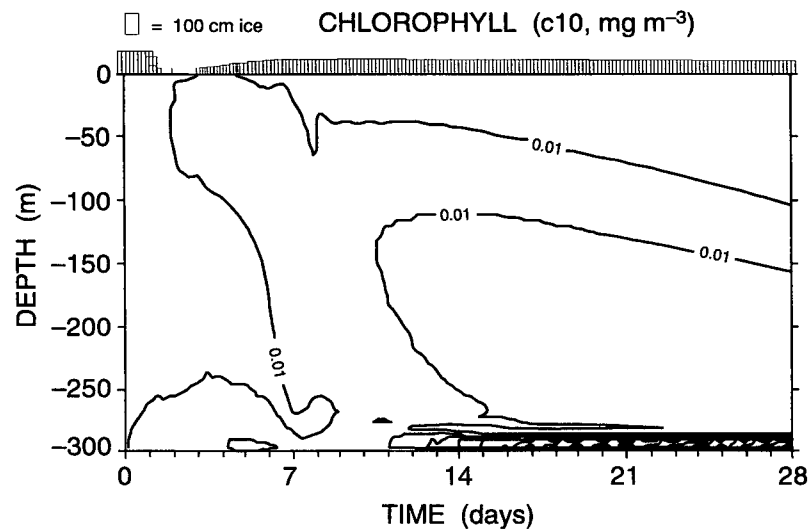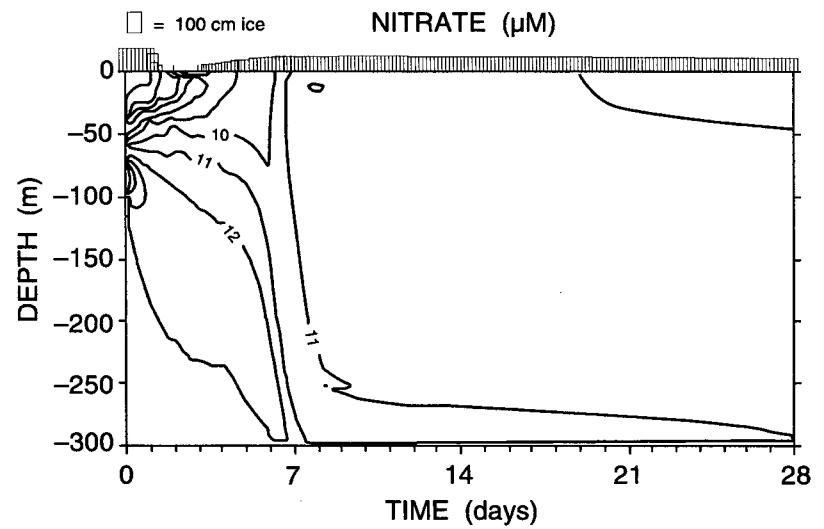
Figure 31b. Time series of the bio-nutrient data for experiment "79". Dashed lines are negative.
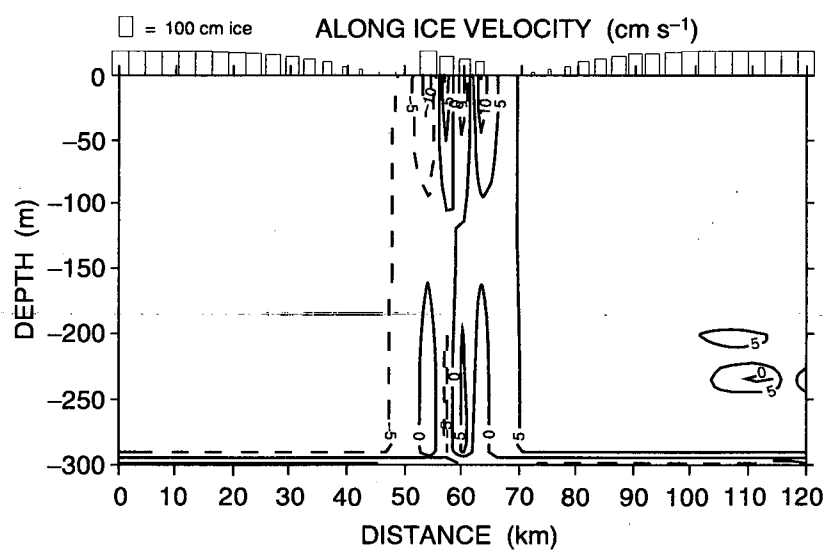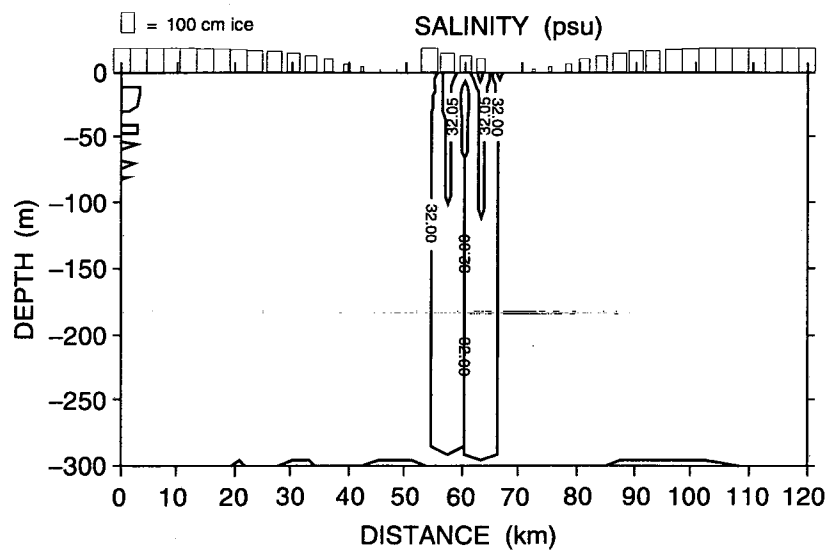
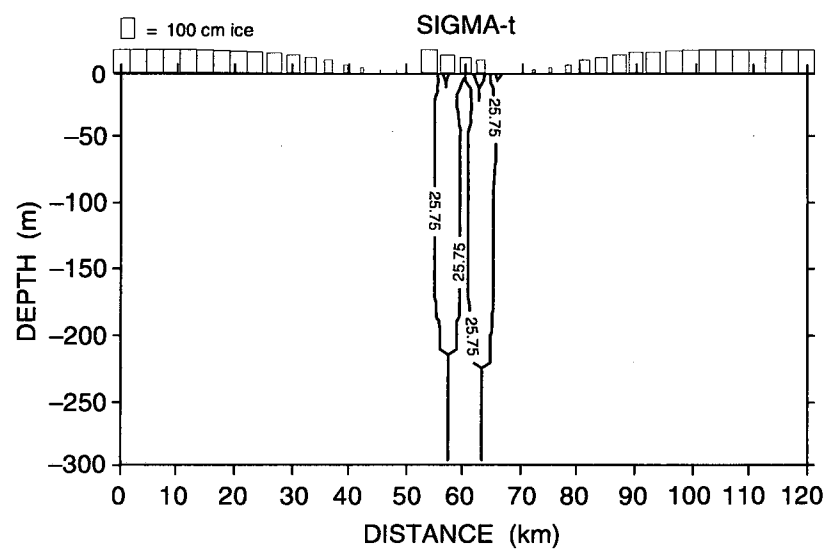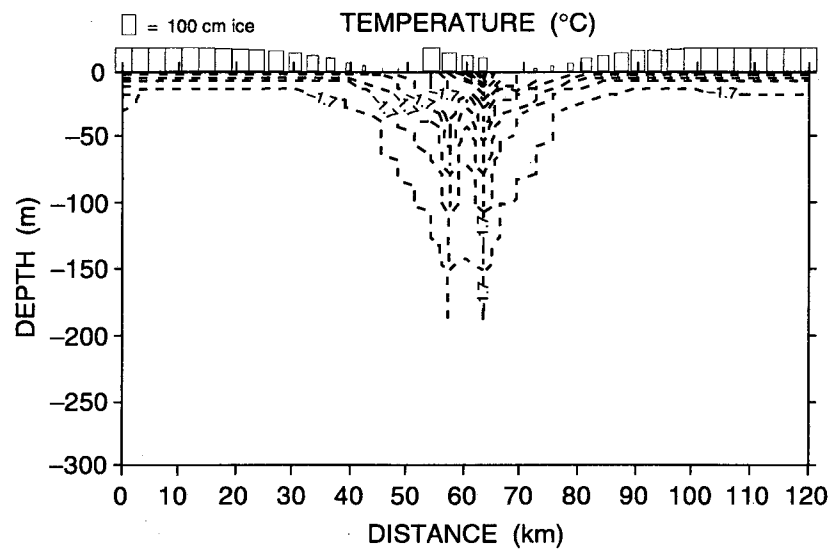Figure 32a. Cross section contours for data at day 6.4 from experiment "79". Dashed lines are negative.

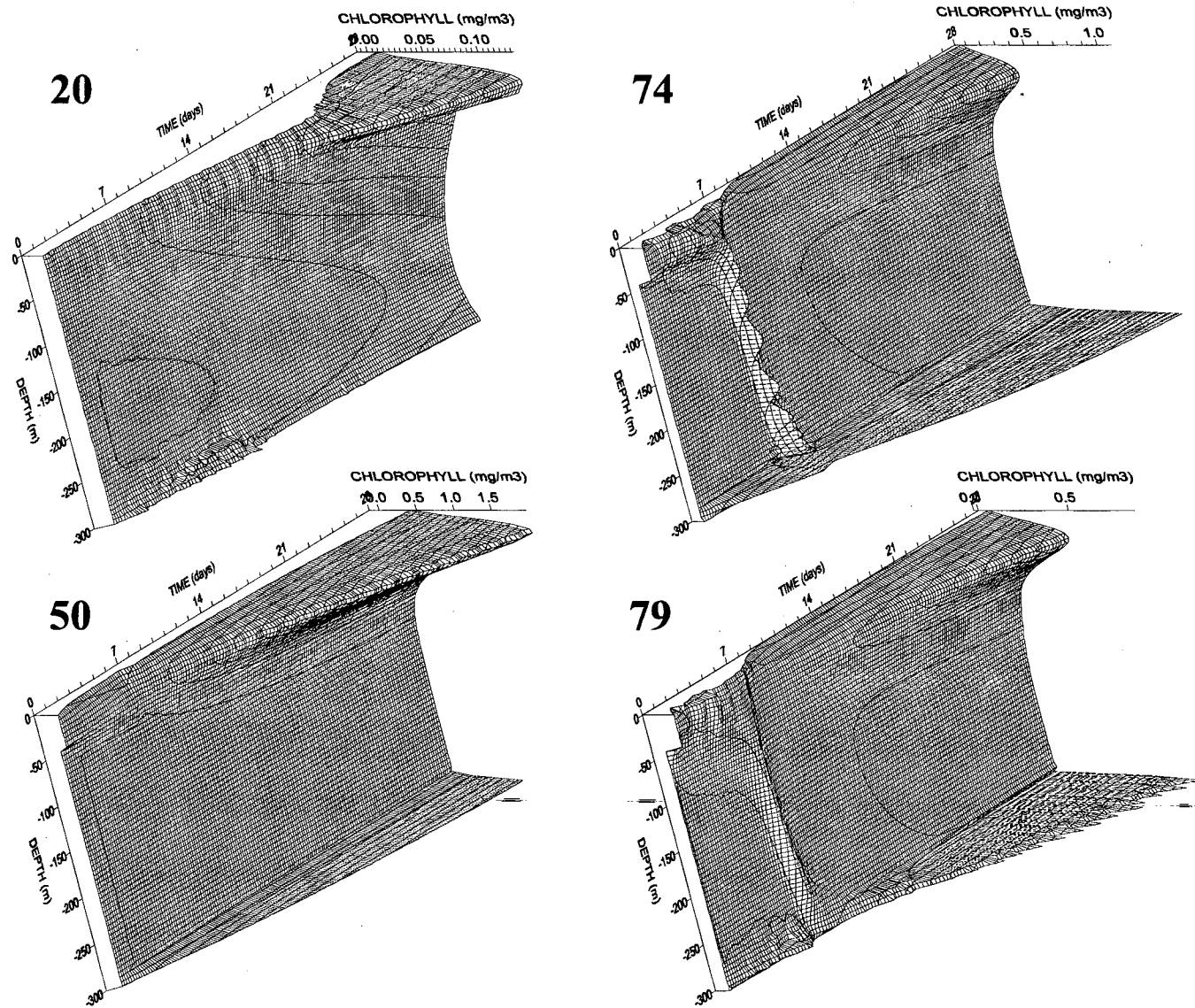Figure 32b. Cross section contours for data at day 6.4 from experiment "79". Dashed lines are negative.

Figure 33.   Time series through depth of total chlorophyll from experiments "20", "50", "74" and "79".

The Department of the Interior Mission

As the Nation's principal conservation agency, the Department of the Interior has responsibility for most of our nationally owned public lands and natural resources. This includes fostering sound use of our land and water resources; protecting our fish, wildlife, and biological diversity; preserving the environmental and cultural values of our national parks and historical places; and providing for the enjoyment of life through outdoor recreation. The Department assesses our energy and mineral resources and works to ensure that their development is in the best interests of all our people by encouraging stewardship and citizen participation in their care. The Department also has a major responsibility for American Indian reservation communities and for people who live in island territories under U.S. administration.

The Minerals Management Service Mission

As a bureau of the Department of the Interior, the Minerals Management Service's (MMS) primary responsibilities are to manage the mineral resources located on the Nation's Outer Continental Shelf (OCS), collect revenue from the Federal OCS and onshore Federal and Indian lands, and distribute those revenues.

Moreover, in working to meet its responsibilities, the **Offshore Minerals Management Program** administers the OCS competitive leasing program and oversees the safe and environmentally sound exploration and production of our Nation's offshore natural gas, oil and other mineral resources. The MMS **Royalty Management Program** meets its responsibilities by ensuring the efficient, timely and accurate collection and disbursement of revenue from mineral leasing and production due to Indian tribes and allottees, States and the U.S. Treasury.

The MMS strives to fulfill its responsibilities through the general guiding principals of: (1) being responsive to the public's concerns and interests by maintaining a dialogue with all potentially affected parties and (2) carrying out its programs with an emphasis on working to enhance the quality of life for all Americans by lending MMS assistance and expertise to economic development and environmental protection.